ADA035055

RADC-TR-76-351

STUDY OF THE EFFECTS OF RADIATION
ON THE ELECTRICAL AND OPTICAL
PROPERTIES OF HgCdTe

IRT Corporation
P.O. Box 80817
San Diego, California 92138

Approved for public release; distribution unlimited.

ROME AIR DEVELOPMENT CENTER
AIR FORCE SYSTEMS COMMAND
GRIFFISS AIR FORCE BASE, NEW YORK 13441

DDC

This report has been reviewed by the RADC Information Office (OI) and is releasable to the National Technical Information Service including foreign nations.

This technical report has been reviewed and is approved.

HENRY M. DEANGELIS
Contract Monitor

REPORT DOCUMENTATION PAGE	READ INSTRUCTIONS BEFORE COMPLETING FORM

1. REPORT NUMBER	2. GOVT ACCESSION NO.	3. RECIPIENT'S CATALOG NUMBER
RADC-TR-76-351		

Final rept. 26 Jun 75 - 26 Jun 76

4. TITLE (and Subtitle)	5. TYPE OF REPORT & PERIOD COVERED
STUDY OF THE EFFECTS OF RADIATION ON THE ELECTRICAL AND OPTICAL PROPERTIES OF HgCdTe.	Scientific: Final for Period 26 June 1975 to 26 June 1976
	6. PERFORMING ORG. REPORT NUMBER
	INTEL-RT-8137-006

7. AUTHOR(s)	8. CONTRACT OR GRANT NUMBER(s)
Charles E. Mallon, Roland E. Leadon and James A. Naber	F19628-75-C-0179

9. PERFORMING ORGANIZATION NAME AND ADDRESS	10. PROGRAM ELEMENT, PROJECT, TASK AREA & WORK UNIT NUMBERS
Intelcom Rad Tech P. O. Box 80817 San Diego, CA 92138	62704H Z99QAXTA026, W. U. 41 CDNA-0001

11. CONTROLLING OFFICE NAME AND ADDRESS	12. REPORT DATE
Deputy for Electronic Technology (RADC) Hanscom AFB, Massachusetts 01731 Monitor: Henry deAngelis/ETSR	November 1976
	13. NUMBER OF PAGES

14. MONITORING AGENCY NAME & ADDRESS(if different from Controlling Office)	15. SECURITY CLASS. (of this report)
127 p.	Unclassified
	15a. DECLASSIFICATION/DOWNGRADING SCHEDULE

16. DISTRIBUTION STATEMENT (of this Report)

Approved for public release; distribution unlimited.

17. DISTRIBUTION STATEMENT (of the abstract entered in Block 20, if different from Report)

19. KEY WORDS (Continue on reverse side if necessary and identify by block number)

Mercury-cadmium-telluride	Photoconductivity	Mobility
Conductivity	Infrared detectors	Spectral response
Hall coefficient	Radiation damage	
Carrier concentration	Carrier lifetime	

20. ABSTRACT (Continue on reverse side if necessary and identify by block number)

Bulk n-type $Hg_{0.8}Cd_{0.2}Te$ was electron, gamma, and neutron irradiated at 10°K. Prior to irradiation, the samples had carrier densities (N_D-N_A) of about 1×10^{14} cm^{-3} and a mobility greater than 1×10^5 cm^2/V·sec. Each type of irradiation produced an increase in carrier density with introduction rates of +12.5 cm^{-1} for 5 MeV electrons, +2.5 $\frac{e}{cm^3}/\frac{n}{cm^2}$ for fission neutrons and $+2.5 \times 10^7$ $\frac{e}{cm^3}$/rad(Si). The mobility

DD $_{1\ JAN\ 73}^{FORM}$ 1473   EDITION OF 1 NOV 65 IS OBSOLETE

408159

damage constant for electron irradiation varied between 3.1 and 7.4×10^{-20} V·sec/e. The mobility damage constant measured for neutron and gamma irradiation was 6.9×10^{-20} V·sec/n and $3.2 \times 10^{-13} \frac{V·sec}{cm^2}$/rad(Si). The electron and gamma irradiation produced a larger increase in conductivity compared to the neutron irradiation as a result of a small neutron produced carrier introduction rate and a larger mobility damage.

During electron irradiation, the carrier lifetime remained essentially constant until the carrier density exceeded $\sim 6 \times 10^{14}$ cm^{-3}, after which the lifetime decreased approximately as $1/n^2$ (Auger recombination). At lower carrier density the lifetime appears to be controlled by Shockley-Read recombination. The 10°K Shockley-Read recombination center introduction rate for 5 MeV electrons was not sufficiently large to appreciably alter the lifetime. The 10°K neutron irradiation however decreased the lifetime, presumably as the result of a larger Shockley-Read introduction rate. A gamma dose of 1×10^6 rad(Si) produced no measurable decrease in carrier lifetime.

Spectral response measurements indicate a 14.7 to 13.3 μm decrease in the 10°K cutoff wavelength during the electron irradiation which increased the carrier density from 9×10^{13} to $\sim 9 \times 10^{14}$ cm^{-3}. The change in cutoff wavelength is believed to be associated with the relatively large increase in carrier density (Burstein Shift). The gamma and neutron irradiations, which resulted in a smaller increase in carrier density, produced no measurable change in cutoff wavelength.

Isochronal anneal to 340°K resulted in a nearly complete recovery of carrier density, mobility, conductivity, spectral response, and carrier lifetime. The recovery of damage produced by the neutron irradiation was less complete.

Damage constants derived from the measured radiation damage were applied to predict response degradation in HgCdTe detectors.

CONTENTS

iii

1. INTRODUCTION

This report presents the results of an experimental and theoretical investigation of the effects of radiation on the optical and electrical properties of the alloy semiconductor HgCdTe. The objective is to obtain sufficient radiation effects data on detector grade material to enable prediction of the radiation response of detectors fabricated from HgCdTe.

This report describes work performed during the period June 26, 1975 to June 26, 1976, and is an extension of work reported in Refs. 1, 2,3, 4, and 8. The previous studies used n-type $Hg_{0.8}Cd_{0.2}Te$ with an extrinsic electron density of about 1.5×10^{15} cm^{-3}. The material used in this study had an extrinsic electron density of about 1×10^{14} cm^{-3} and is considered to be more representative of current state-of-the-art detector grade material.

The results obtained from measurements on HgCdTe (e.g., carrier life-time and photoresponse) are influenced by the experimental conditions. Therefore, Section 3 describes the experimental procedures and conditions in detail to allow comparison and correlation of this data with that of other investigations.

Sections 4 and 5 discuss the results of a $9.5°K$, 5-MeV electron irradiation ($\Phi = 7 \times 10^{13}$ e/cm^2) and isochronal anneal to $340°K$. The sample used for this irradiation had an initial carrier density and mobility of $\sim 1 \times 10^{14}$ e/cm^3 and 1.6×10^5 $cm^2/V \cdot sec$.

In Section 5, the results of $10°K$ gamma and neutron irradiation are presented. The gamma exposure was 1×10^6 rad(Si). After isochronal anneal to $340°K$ the same sample was then neutron irradiated to a fluence of 1.2×10^{13} $n/cm^2 > 10$ keV. The initial carrier density and mobility for this sample was $\sim 1 \times 10^{14}$ e/cm^3 and 3×10^5 $cm^2/V \cdot sec$.

1

In Section 6, the damage constants measured during the various irradiations are compiled and a method is developed for applying the damage constants to estimate degradation of photoconductive response.

During the course of the program, 9 samples were fabricated and screened for radiation effects studies. In general, observation of a small low temperature mobility ($\mu \ll 10^5$ cm^2/V·sec) was the reason for rejection of samples not chosen for irradiation. A fairly complete set of data for two of the samples in this category is given in Section 7.

Section 8 compares the electrical conductivity temperature dependence of two commercial HgCdTe detectors with sample I-1 which was neutron and gamma irradiation. The comparison indicated that the carrier density and mobility of the detectors was probably within a factor of two of the carrier density and mobility of bulk sample I-1.

2

2. SUMMARY

Radiation effect studies were performed at 10°K on samples of bulk n-type $Hg_{0.8}Cd_{0.2}Te$. The samples had preirradiation carrier densities of $\sim$1 x 10^{14} cm^{-3} and mobility greater than 1 x 10^5 cm^2/V·sec. Sample II-4 was irradiated with 5-MeV electrons to a fluence of 7.2 x 10^{13} e/cm^2. A second sample, I-1, was gamma irradiated to a total dose of 1 x 10^6 rad(Si), isochronal annealed to 340°K, and then irradiated with a fission neutron fluence of 1.3 x 10^{13} n/cm^2 > 10 keV. The radiation effects studies concentrated on material parameters that are important to detector operation such as carrier density, mobility, conductivity, carrier lifetime and cutoff wavelength.

The significant radiation effects observed during the irradiations are given below.

<u>10°K Electron Irradiation, Φ = 7.2 x 10^{13} e/cm^2 (5 MeV)</u>

1. The increase in carrier density with fluence was slightly nonlinear. The carrier introduction rate increased from 10 cm^{-1} during the initial part of the irradiation to 14 cm^{-1} at the end of the irradiation.

2. The Hall mobility decreased initially with a mobility damage constant of 7.4 x 10^{-20}. This damage constant decreased to 3.1 x 10^{-20} V-sec/e towards the end of the irradiation.

3. The increase in carrier density was greater than the decrease in mobility, resulting in a net factor of 5.9 increase in electrical conductivity.

4. The steady-state photoconductivity at 6.3°K exhibited a carrier density dependence of 1/n at lower carrier density (n < 6 x 10^{14} cm^{-3}) and >1/n^2 for carrier densities >6 x 10^{14} cm^{-3}. The 9.5°K signal exhibited approximately

3

the same dependence for carrier densities $>3 \times 10^{14}$ cm^{-3}.
The carrier lifetime determined from the steady-state
photoconductivity and photoconductive decay indicates
that the carrier lifetime at 6.3°K was relatively
independent of carrier density for $n < 6 \times 10^{14}$ cm^{-3} and
decreased approximately as $1/n^2$ for $n > 7 \times 10^{14}$ cm^{-3}. At
the lower carrier densities, it appears that the lifetime
was controlled by Shockley-Read recombination which
dominates until the carrier density becomes large enough
for recombination by the Auger process ($\tau \propto 1/n^2$) to
become important.

5. Spectral response measurements indicated that the 10°K
   cutoff wavelength decreased from 14.7 to 13.3 µm during
   irradiation. Recovery to near the preirradiation value
   occurred during anneal to 330°K.

6. After irradiation, the photoconductive response to pulsed
   injection was prompt and appeared to have only a single
   decay time constant. After the 100°K anneal, the longest
   decay time constant observed was ∿4 µsec, compared to about
   700 µsec before irradiation.

Isochronal anneal to 300°K after irradiation resulted in substantial
recovery of the above parameters.

10°K Gamma Irradiation

Sample I-1 was gamma irradiated at 10°K using bremsstrahlung produced
by a 5-MeV electron beam and a tantalum converter. The total dose during
the irradiation was 1×10^6 rad(Si).

The gamma irradiation produced an increase in carrier density with
an introduction rate of 2.5×10^7 e/cm^3/rad(Si). The carrier introduction,
coupled with a small decrease in mobility resulted in an increase in
conductivity. The carrier lifetime determined from the decay of excess
conductivity produced by a GaAs LED was unchanged by the gamma dose of
1×10^6 rad(Si). Isochronal anneal to 340°K resulted in a nearly complete
recovery of the above parameters, with the majority of the recovery
occurring below 100°K.

4

10°K Neutron Irradiation, $\Phi = 1.2 \times 10^{13}$ n/cm^2 > 10 keV

The 10°K neutron irradiation increased the carrier density with an introduction rate of 2.5 e/cm^3 per n/cm^2, which is about a factor of five less than for 5 MeV electrons. The mobility damage per carrier introduced was about a factor of 3 larger for the neutron irradiation, than for the 5 MeV electron irradiation.

The neutron irradiation caused a decrease in carrier lifetime presumably as the result of an increase in the number of Shockley-Read recombination centers. A calculated lifetime damage constant $K = \Delta \frac{1}{\tau}/\Phi$ of 9×10^{-9}cm^2/n·sec was obtained from the decreased lifetime. The neutron damage, unlike electron and gamma damage, exhibited only a partial recovery during anneal to 340°K.

Damage constants derived from radiation effects data gave a reasonable fit when used to estimate photoresponse degradation in the bulk samples. Radiation effects data for actual HgCdTe detectors is not presently available for comparison. The temperature dependence of the electrical conductivity of two high performance HgCdTe detectors agreed reasonably well with similar data obtained from the bulk material used in these studies. This agreement supports a conclusion that the bulk material studied is probably representative of material used in detector fabrication.

A logical next step in radiation effects in HgCdTe would be the irradiation of actual detectors to verify the applicability of damage parameters obtained from bulk material studies. Also, there is some indication that irradiation may partially eliminate the undesirable low frequency response observed in photoconductive HgCdTe detectors at low background. This comment is prompted by the disappearance of the longer time constant during the 9.5°K electron irradiation of Sample II-4. The longer time constant recovered during subsequent isochronal anneal to 340°K; however, the recovery was not complete.
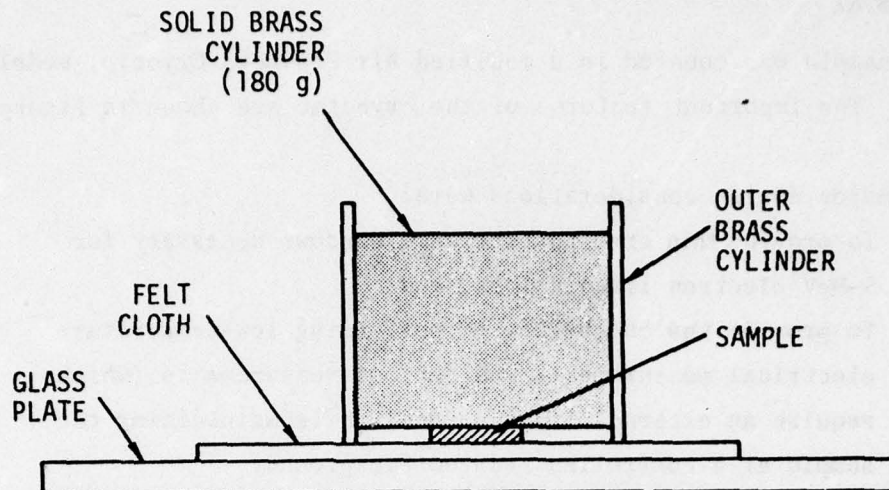
3. EXPERIMENTAL PROCEDURE

3.1 SAMPLE PREPARATION

Sample II-4 as received was 12 mm long, 3 mm wide, and 0.56 mm thick. The length and width of the sample were not altered. The thickness of the sample was decreased to 0.228 mm, as described below. The sample was mounted to the solid brass cylinder of the lapping fixture shown in Figure 3-1 with phenyl salicylate, which liquefies slightly above room temperature. During the lap, the only pressure exerted on the sample resulted from the weight of the solid brass cylinder, which is a slip-fit in the outer cylinder. The sample was first lapped with 3-µm, followed by 0.3-µm, Al_2O_3, which decreased the thickness to 0.258 mm. The sample was then etched in methanol-20 percent bromine to a final thickness of 0.228 mm.

Etching is performed in a plastic beaker with small holes which fits into a larger beaker containing the etch solution. During the etch, the beaker containing the sample is raised and lowered continuously to prevent the sample from resting on the beaker surface. Preferential etching has been observed when the sample is allowed to rest on the bottom of the beaker. After the etch, the sample is rinsed and stored in methanol until contact application.

3.2 SAMPLE CONTACTS

After etching, five indium-soldered contacts were applied to sample II-4 for measurement of electrical conductivity, Hall mobility, carrier density, and optical properties. A small piece of indium is placed on the sample at the desired contact location. The indium is then fused to the sample by bringing the tip of a hot wire attached to a soldering iron tip into contact with the indium. It is not generally necessary for the hot wire to touch the sample during contact application. Contacts made by this technique are quite small (~0.2-mm-dia.) and require minimal sample heating. Positions of the contacts on sample II-4 are shown in Figure 3-2.

6

SOLID BRASS
CYLINDER
(180 g)

OUTER
BRASS
CYLINDER

FELT
CLOTH

SAMPLE

GLASS
PLATE

RT-13102

Figure 3-1. Fixture used to lap samples

VOLTAGE PROBES

"A"

0.447

I

0.301

4.94

HALL PROBE

1.07

DIMENSIONS
IN cm

SAMPLE THICKNESS = 0.0228 cm

"A" = SLOT IN SAMPLE MOUNT WHICH
DEFINES ILLUMINATED AREA
OF SAMPLE
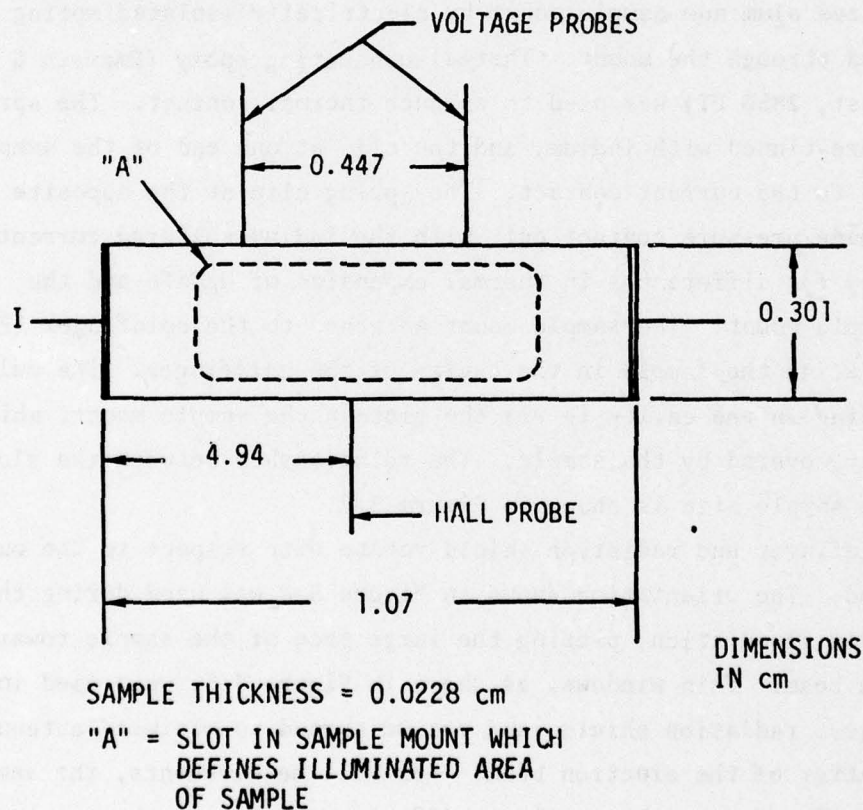
RT-13103

Figure 3-2. Sample II-4 contact and masking arrangement

7

3.3 CRYOSTAT

The sample was mounted in a modified Air Products Cryotip, model
LT-3-110. The important features of the cryostat are shown in Figure
3-3.

The major design considerations were:

1. To provide thin cryostat entrance windows necessary for
    5-MeV electron irradiations, and

2. To provide the capability of performing low-temperature
    electrical measurements and optical measurements (which
    require an external light source) while maintaining the
    sample at a controlled reduced background.

This was accomplished by placing the sample 3 inches from the optical
aperture in the cold radiation shield. The background level was then
controlled by choice of the aperture diameter. The sample was attached
to the anodized aluminum sample mount by electrically isolated spring
clips epoxied through the mount. Thermal-conducting epoxy (Emerson &
Cuming Stycast, 2850 FT) was used to enhance thermal contact. The spring
clips were pre-tinned with indium, and the clip at one end of the sample
was soldered to the current contact. The spring clip at the opposite
sample end made pressure contact only with the indium-soldered current
lead to allow for differences in thermal expansion of HgCdTe and the
aluminum sample mount. The sample mount attaches to the coldfinger (Fig-
ure 3-3), placing the sample in the cavity of the coldfinger. The only
optical opening in the cavity is via the slot in the sample mount, which
is completely covered by the sample. The relationship between the slot
size and the sample size is shown in Figure 3-2.

The coldfinger and radiation shield rotate with respect to the outer
vacuum shroud. The orientation shown in Figure 3-3 was used during the
5-MeV electron irradiation, placing the large face of the sample toward
the electron beam. Thin windows, as shown in Figure 3-3, were used in
the coldfinger, radiation shield, and vacuum shroud to minimize attenua-
tion and scatter of the electron beam. For Hall measurements, the sample
was rotated 90°, placing the sample at 45° with respect to the magnetic
field.

8

SPRING CLIPS

ANODIZED Al
SAMPLE MOUNT

KRS-5
WINDOW

0.100-in.
APERTURE

OPTICAL PATH

GaAs LED

T.C.

3 in.

MAGNETIC FIELD
NORMAL TO PAPER

⊙ B

SAMPLE

0.002-in. Al

0.002-in. Ti

e-BEAM

VACUUM SHROUD

RADIATION SHIELD
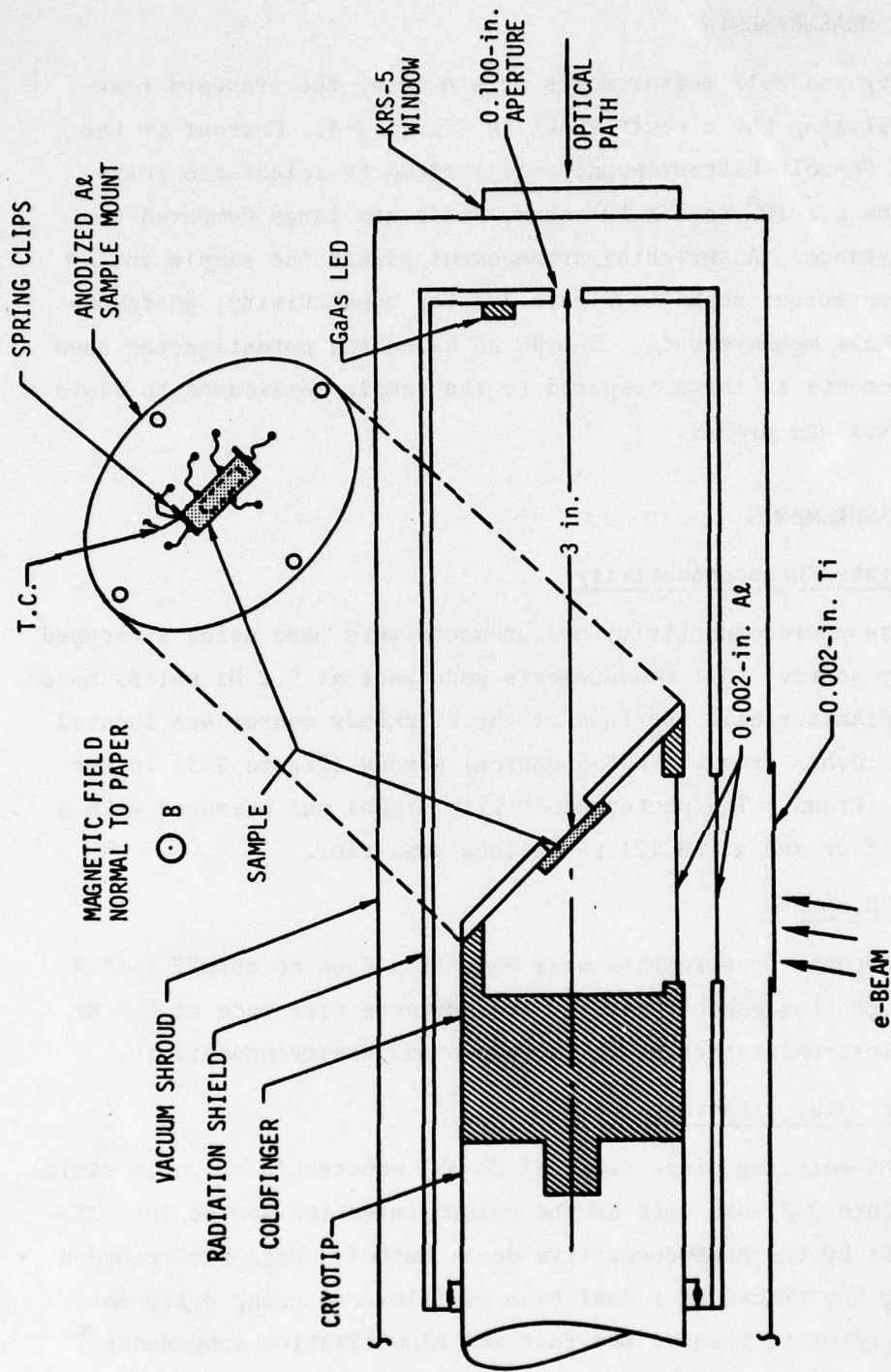
COLDFINGER

CRYOTIP

RT-13104

Figure 3-3. Sample cryostat

9

3.4 ELECTRICAL MEASUREMENTS

Conductivity and Hall measurements were made by the standard four-probe method utilizing the circuit shown in Figure 3-4. Current to the sample from the 90-volt battery supply was limited by selectable resistors ranging from 5×10^3 to 1×10^6 ohms, which are large compared to the sample resistance. A switching arrangement placed the sample in the alternate configurations shown in Figure 3-4 for conductivity, photoconductivity, and Hall measurements. The 50-kΩ balancing potentiometer used for Hall measurements is large compared to the sample resistance to avoid loading of the voltage probes.

3.5 OPTICAL MEASUREMENTS

3.5.1 Steady-State Photoconductivity

Steady-state photoconductivity measurements were made using a chopped 1000°K blackbody source. All measurements were made at 5.2 Hz unless noted. The 0.375-inch-diameter exit aperture of the blackbody source was located approximately 6 inches from the KRS-5 optical window (Figure 3-3) in the cryostat vacuum shroud. The photoconductivity signal was measured with a PAR 113 preamplifier and a PAR 121 phase-lock amplifier.

3.5.2 Spectral Response

Spectral response measurements were made from 5 μm to cutoff (∼15.5 μm) with a Spex grating monochromator. Measurements were made at 5.2 Hz using the same instrumentation as for steady-state photoconductivity.

3.5.3 Transient Decay Lifetime

A GaAs light-emitting diode (LED; TI XL-35) mounted in the cold radiation shield (Figure 3-3) was used as the pulsed-injection source for lifetime measurements by the photoconductive decay method. Data was recorded by photographing the traces of a dual-beam oscilloscope using different gains and sweep rates to resolve the fast and slow lifetime components.
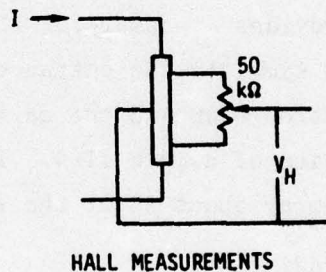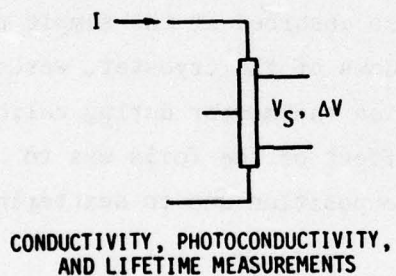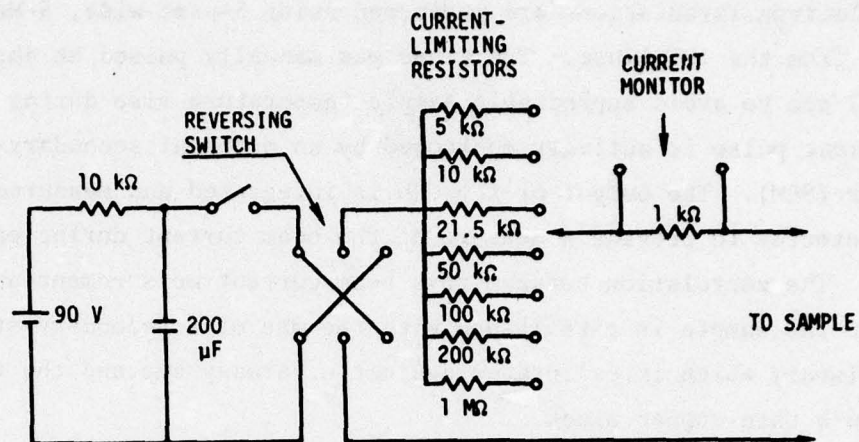
Figure 3-4. Circuit for electrical measurements

RT-13105

11

3.6 IRRADIATION PROCEDURE

3.6.1 Electron Irradiation

Electron irradiations are performed using 5-μsec-wide, 5-MeV electron pulses from the IRT Linac. The Linac was manually pulsed at about 1 pulse every 2 sec to avoid appreciable sample temperature rise during irradiation. Each Linac pulse is actively monitored by an external secondary-emission monitor (SEM). The output of the SEM is integrated and measured by a peak detector to provide a measure of the beam current during each Linac pulse. The correlation between this beam-current measurement and the fluence at the sample is established with the use of a secondary standard (thermistor) which is calibrated against a Faraday cup and the temperature rise in a thin copper block.

The thermistor is mounted in a styrofoam block for thermal isolation and forms one leg of a balanced Wheatstone bridge circuit. When the Linac is pulsed, the dose absorbed in the thermistor material results in a decrease in thermistor resistance, and the corresponding unbalance voltage of the bridge provides a measure of the dose absorbed at the sample position. Foils, to simulate the entrance windows of the cryostat, were placed between the electron beam and the calibration thermistor during calibration for the irradiation of sample II-4. The effect of the foils was to reduce the electron beam by about 5% at the sample position due to scattering.

3.6.2 Gamma Irradiations

Gamma irradiations were performed with bremsstrahlung produced by a 5-MeV electron beam and a 40-mil tantalum converter. The tantalum converter was backed with 0.250-inch aluminum to insure that none of the primary electron beam reached the sample. Electron pulses with an average current of ∿300 mA and 6 μsec in width resulted in a gamma dose of about 0.44 rad(Si)/pulse at the sample location. A pulse rate of 180 pps was used during the irradiation with no appreciable sample heating. Cobalt glass dosimeters were used to measure the gamma dose.

12

3.6.3 Neutron Irradiations

Neutrons with approximately a fission spectrum were produced by
γ-n reactions resulting from a 55-MeV electron beam and a thick Fansteel
(tungsten) target. The sample was positioned at the side of the target,
90° with respect to the electron beam to reduce the gamma dose. The
gamma dose was further reduced by a 4-inch thick depleted uranium
shield between the target and sample. This arrangement resulted in
approximately 1.25×10^7 n/cm^2 > 10 keV for each pulse. A gamma dose
of 5.2×10^{-2} rad(Si)/pulse was measured using cobalt glass dosimeters.
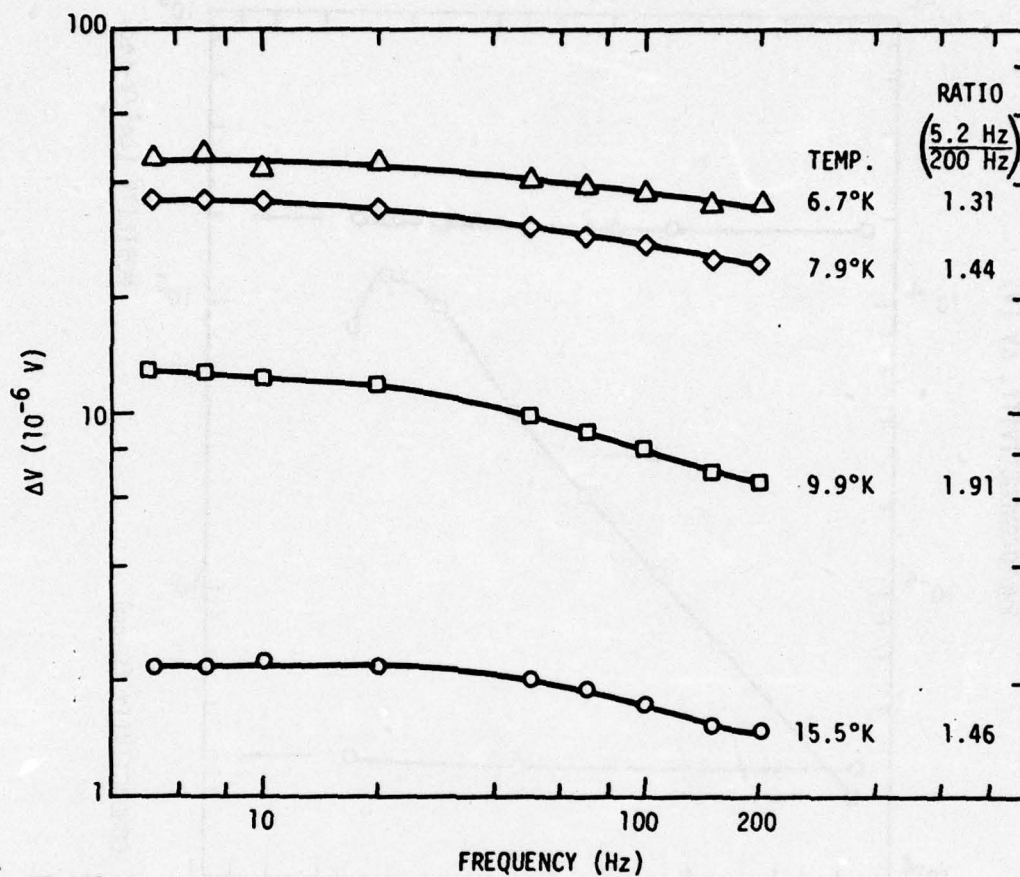
4. RESULTS OF ELECTRON IRRADIATION

Sample II-4 was irradiated at 10°K to a 5-MeV electron fluence of 7.1×10^{13} e/cm^2. The sample was obtained from Texas Instruments, Inc. Sample II-4 was n-type with an "x" value of 0.2 ±0.3 mole percent, and was grown by the solid-state recrystallization method.

Preirradiation measurements included temperature dependence of the carrier density, Hall mobility, electrical conductivity, steady-state photoconductivity, and photoconductive decay lifetime. These parameters, with the exception of photoconductive decay lifetime, were monitored periodically during the electron irradiation. Spectral dependence of the photoconductivity was measured at 10°K before irradiation, after irradiation, and after various isochronal anneals to 330°K.

Before irradiation, several diagnostic measurements were made to determine appropriate sample bias levels and the chopping frequency for steady-state photoconductivity measurements. Figure 4-1 shows the frequency dependence of the steady-state photoconductivity signal (PC) at several temperatures. Due to the observed decrease in the PC signal with frequency, the PC temperature dependence measurements and the spectral response measurements were made at 5.2 Hz unless noted. Figure 4-2 shows the bias dependence of the steady-state photoconductivity, Hall mobility, and electrical conductivity. At biases less than 0.1 V/cm, the conductivity and mobility were independent of bias and the PC signal (ΔV) was approximately linear with bias; therefore, all measurements were made with the electric field equal to or less than 0.1 V/cm.

An optical input aperture (Figure 3-3) of 0.020 inch diameter was used for initial preirradiation measurements; however, with this configuration only marginal spectral response measurements were obtained. The input aperture was, therefore, enlarged to 0.1-inch-diameter. Enlargement of the aperture, which increased the background from 1.5×10^{13} to 3.6×10^{14} photons/cm^2-sec, had no effect on the sample resistance at low temperature, as shown in Figure 4-3.

14

100

RATIO

$\left(\dfrac{5.2\ Hz}{200\ Hz}\right)$

TEMP.

ΔV (10^{-6} V)

6.7°K   1.31

7.9°K   1.44

10

9.9°K   1.91

15.5°K   1.46

1

10   100   200

FREQUENCY (Hz)

RT-13106

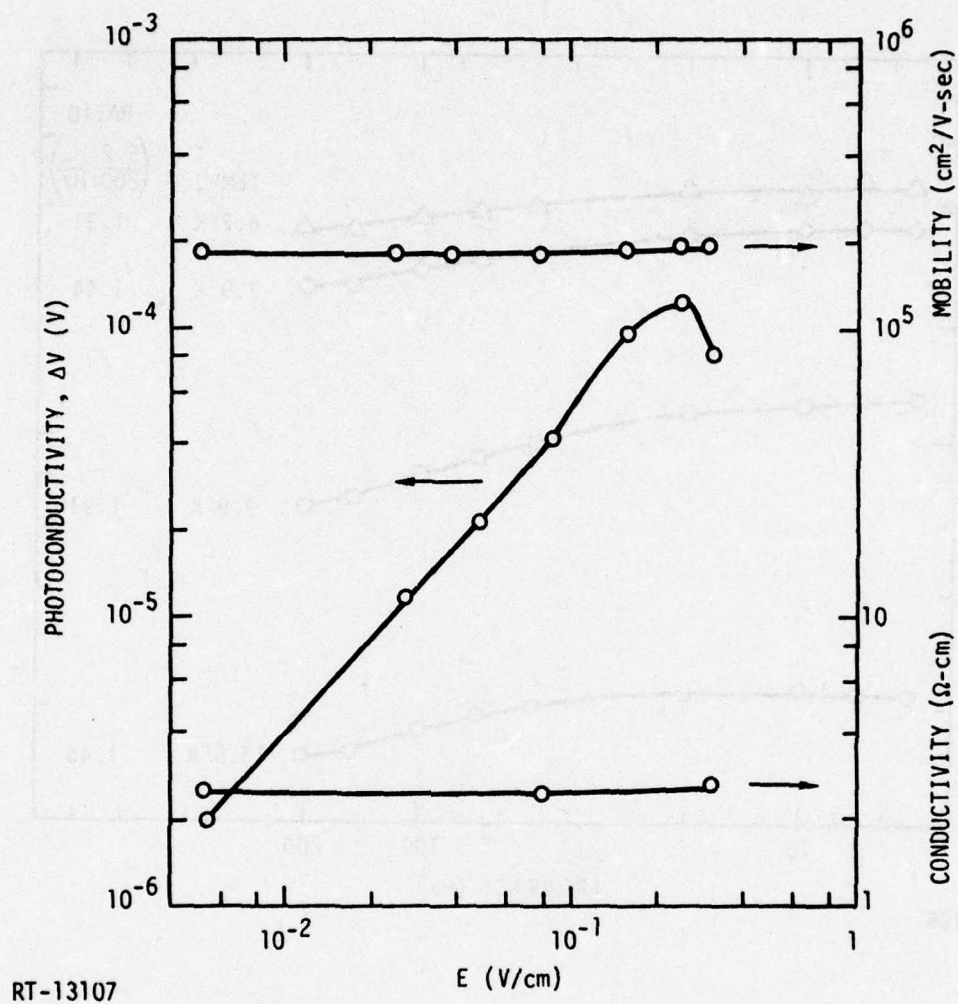Figure 4-1. Photoconductivity frequency dependence

15

RT-13107

Figure 4-2.   Photoconductivity, mobility, and
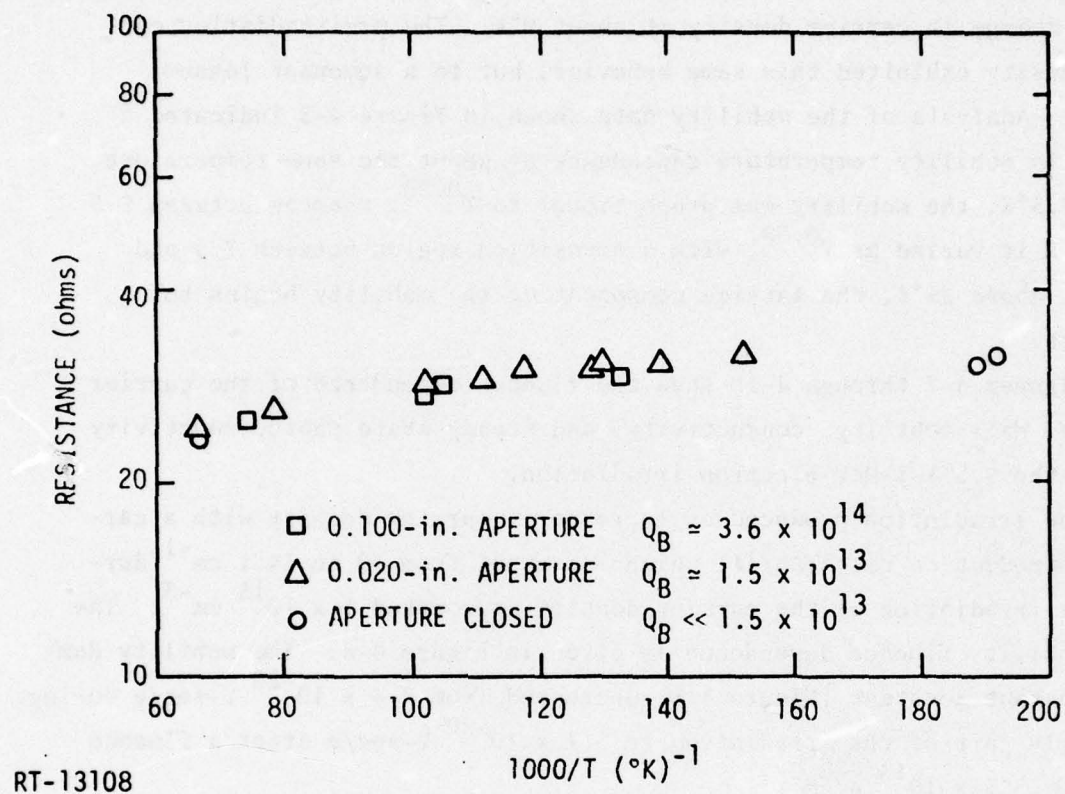conductivity bias dependence

16

RT-13108

Figure 4-3. Temperature dependence of sample resistance
for different background levels

17

The temperature dependence of the carrier density, Hall mobility, and electrical conductivity before irradiation and during cooldown after various postirradiation isochronal anneals is shown in Figure 4-4, 4-5, and 4-6. The inset in Figure 4-4 is the carrier density temperature dependence after the 330°K anneal on an enlarged scale to show the small abrupt change in carrier density at about 9°K. The preirradiation carrier density exhibited this same behavior, but to a somewhat lesser degree. Analysis of the mobility data shown in Figure 4-5 indicated a change in mobility temperature dependence at about the same temperature. Below 7.5°K, the mobility was proportional to $T^{0.20}$, whereas between 9.5 and 19°K it varied as $T^{0.39}$, with a transition region between 7.5 and 9.5°K. Above 25°K, the lattice component of the mobility begins to dominate.

Figures 4-7 through 4-10 show the fluence dependence of the carrier density, Hall mobility, conductivity, and steady-state photoconductivity during the 9.5°K 5-MeV electron irradiation.

The irradiation produced an increase in carrier density with a carrier introduction rate ($\Delta n/\Delta \Phi$) which increased from 10 to 14.1 cm^{-1} during the irradiation as the carrier density approached 1×10^{15} cm^{-3}. The Hall mobility fluence dependence is given in Figure 4-8. The mobility damage constant constant (Figure 4-8) decreased from 7.4×10^{-20} V-sec/e during the early part of the irradiation to 3.1×10^{-20} V-sec/e after a fluence of about 3.5×10^{13} e/cm^2.

The electrical conductivity (Figure 4-9) shows an almost linear increase with fluence as a result of the increasing carrier density and decreasing mobility.

The steady-state photoconductivity shown in Figure 4-10 initially decreased, then increased until after a fluence of about 2×10^{13} e/cm^2, then decreased for larger fluences. As will be seen later in the isochronal anneal data, this behavior in photoconductivity with damage was observed only at 9.5°K; the photoconductivity signal at 6.3°K does not exhibit multiple values with damage.

Isochronal anneal of the carrier density, Hall mobility, electrical conductivity, and steady-state photoconductivity is presented in Figures 4-11 through 4-14. The anneals were of 10-min duration, with measurements
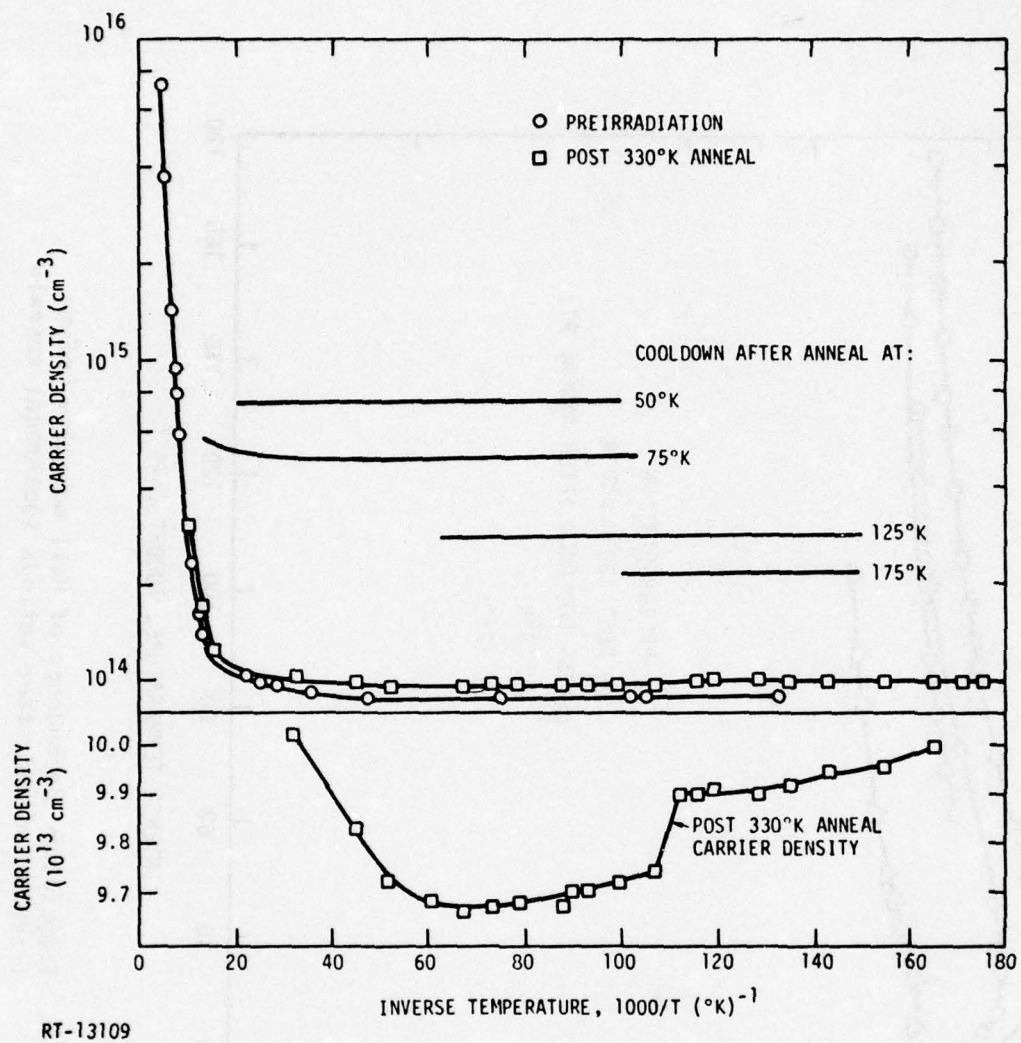
18

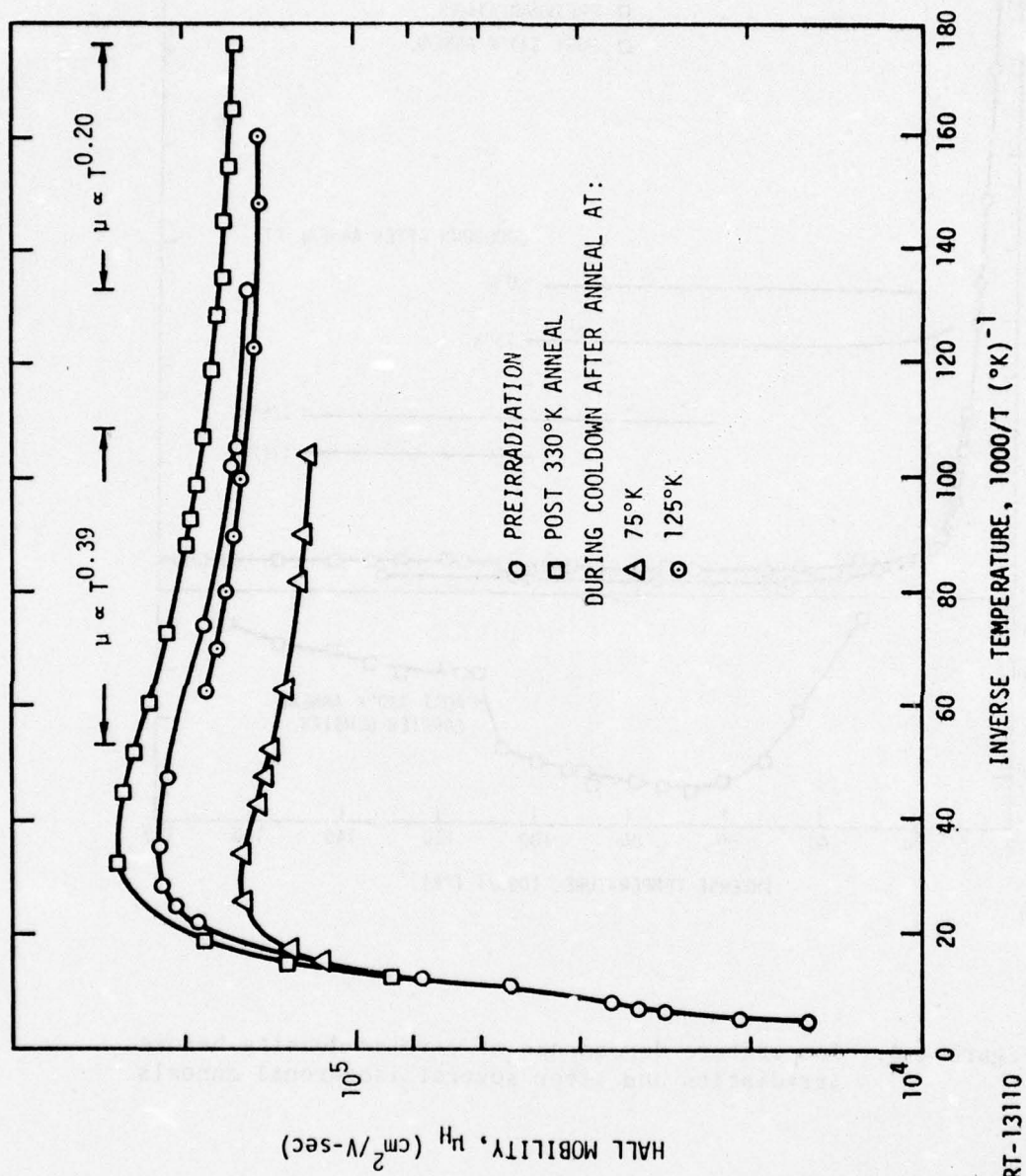Figure 4-4. Temperature dependence of carrier density before irradiation and after several isochronal anneals

RT-13109

Figure 4-5. Temperature dependence of Hall mobility before irradiation and after various isochronal anneals
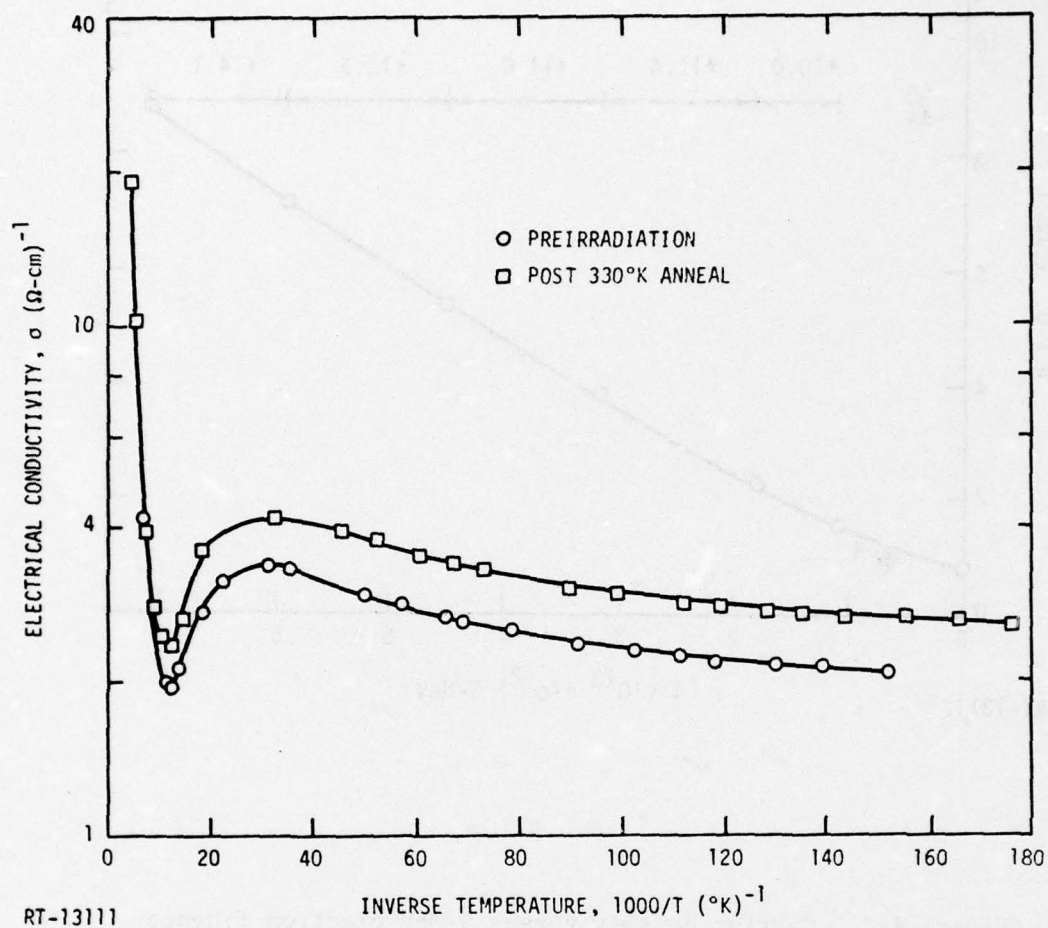
RT-13110

20

ELECTRICAL CONDUCTIVITY, σ (Ω-cm)⁻¹

40

10

4

1

O PREIRRADIATION
□ POST 330°K ANNEAL

0   20   40   60   80   100   120   140   160   180

INVERSE TEMPERATURE, 1000/T (°K)⁻¹

RT-13111

Figure 4-6.   Temperature dependence of electrical
conductivity before irradiation and
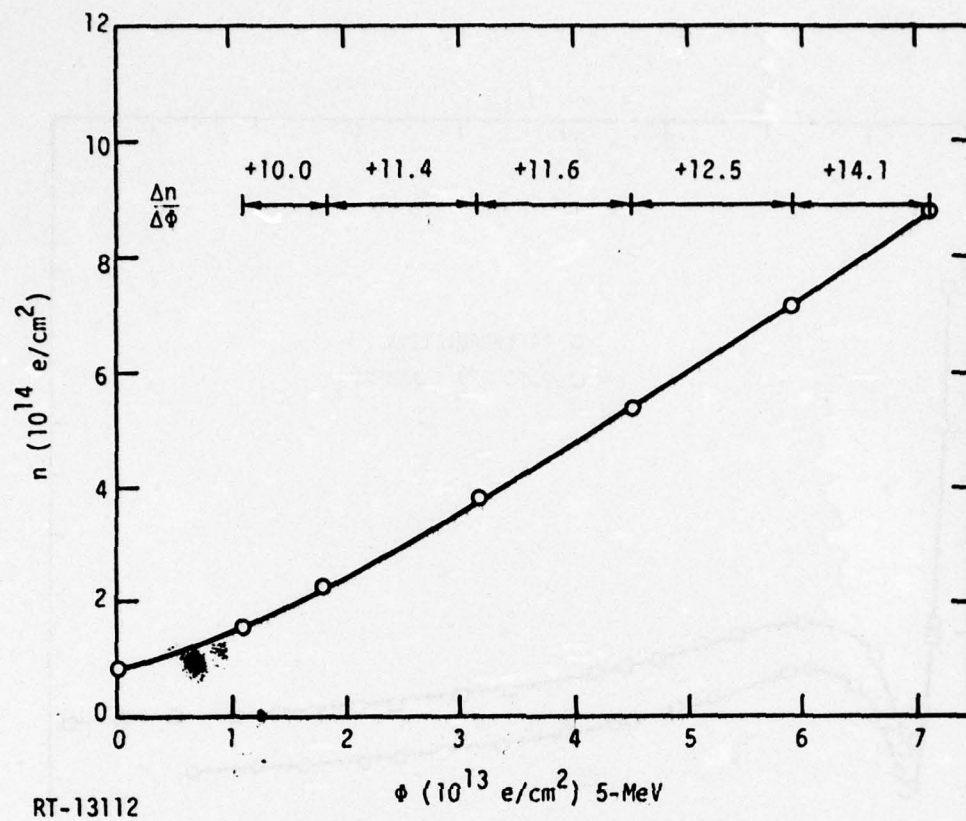after the 330°K isochronal anneal

Figure 4-7. Carrier density versus 5-MeV electron fluence at 9.5°K, sample II-4
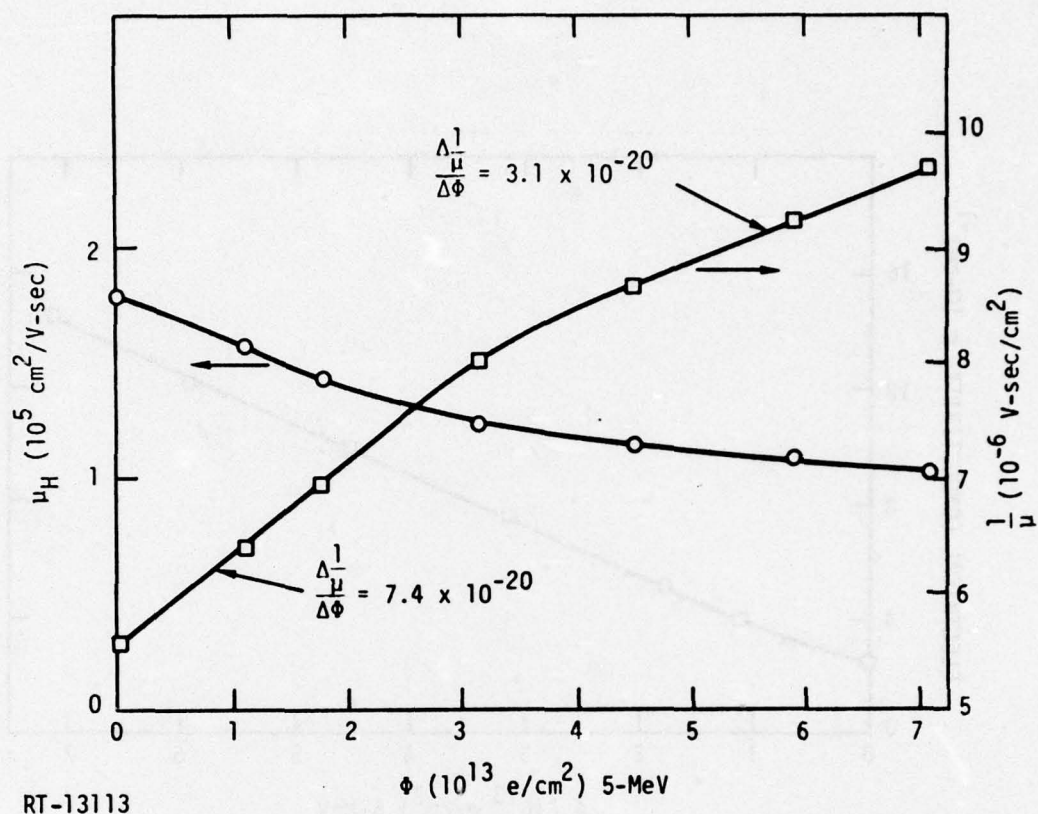
RT-13112

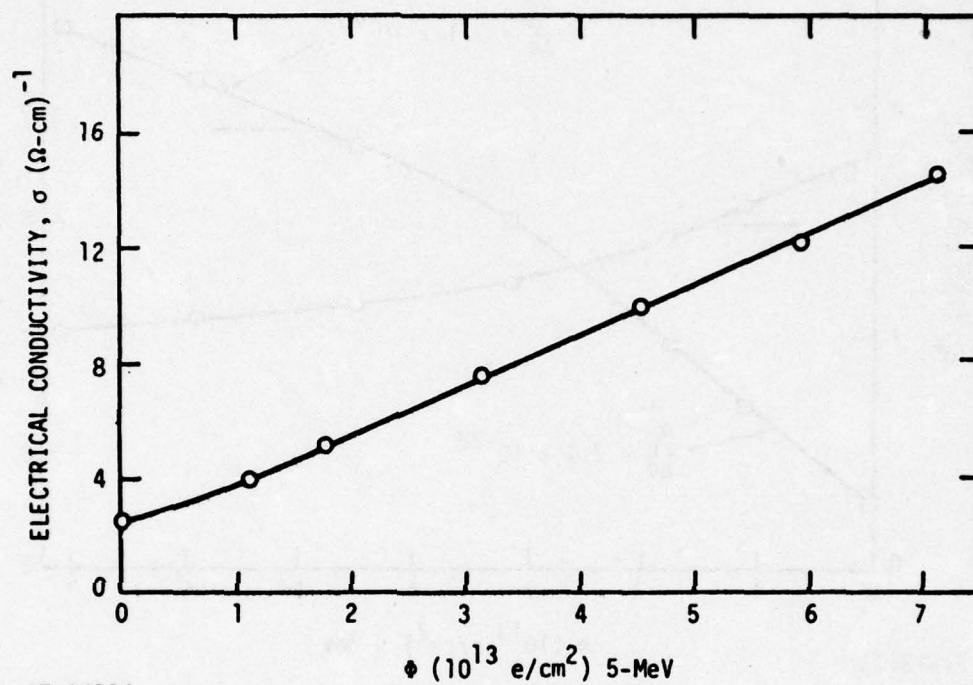RT-13113

Figure 4-8. Hall mobility versus 5-MeV electron fluence at 9.5°K, sample II-4

RT-13114

Figure 4-9. Electrical conductivity versus 5-MeV
electron fluence at 9.5°K, sample II-4

24

STEADY-STATE PHOTOCONDUCTIVITY ($\Delta V/V \times 10^{-3}$)

Φ (10^{13} e/cm^2) 5-MeV

RT-13115

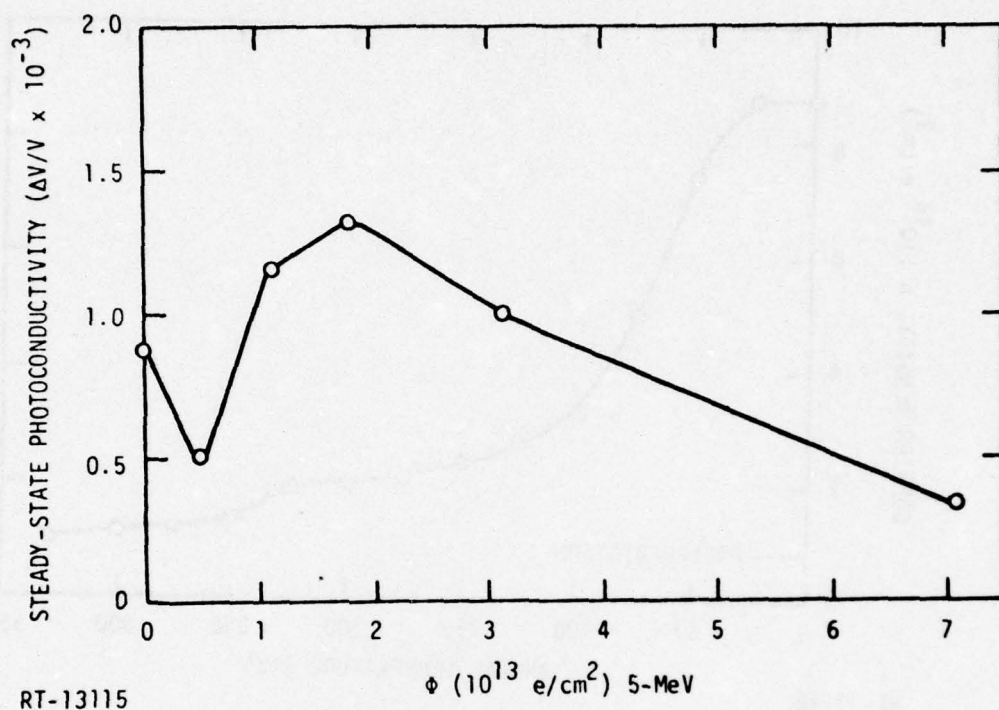Figure 4-10.   Steady-state photoconductivity versus 5-MeV
electron fluence at 9.5°K, sample II-4

25
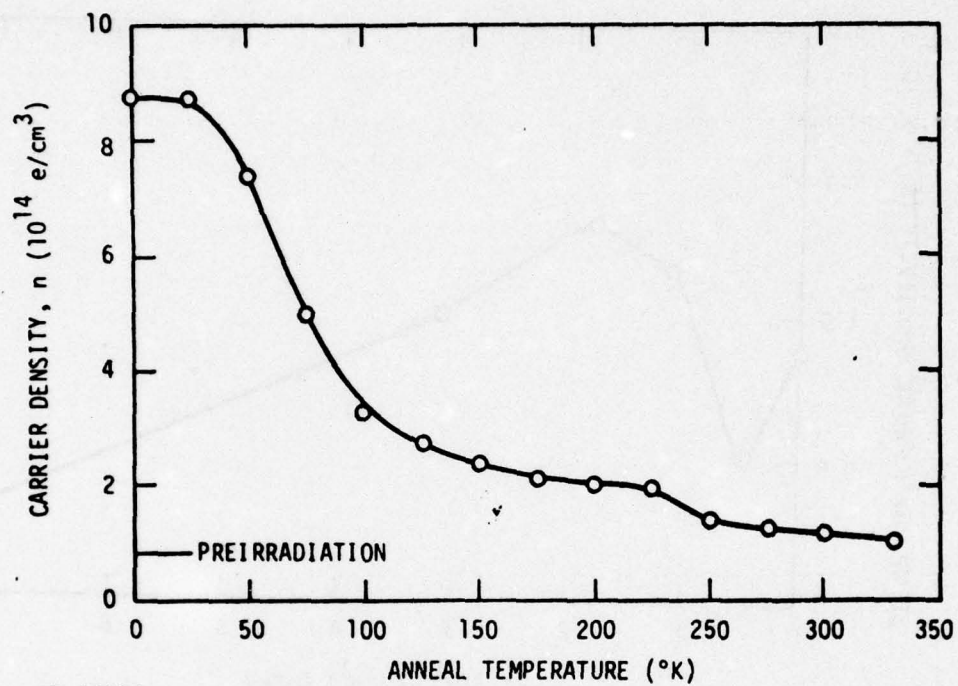
RT-13116

Figure 4-11.   Isochronal anneal (10 min) of carrier density after
9.5°K, 5-MeV electron irradiation; measurement at
9.5°K after each anneal

26
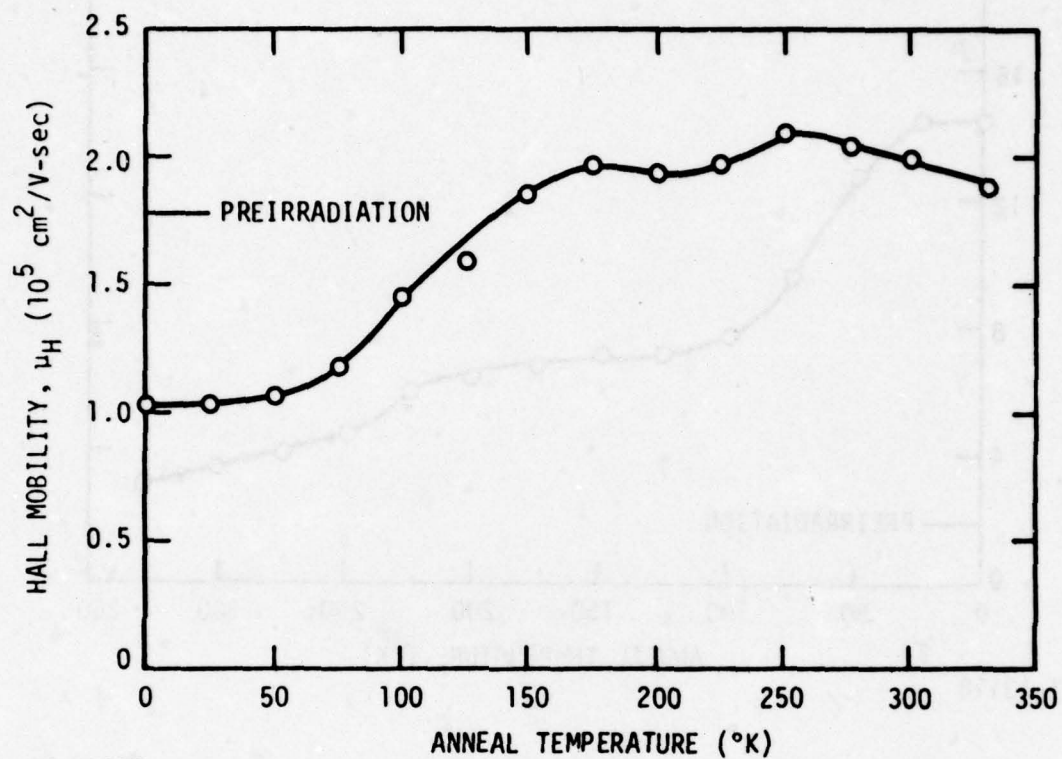
RT-13117

Figure 4-12. Isochronal anneal (10 min) of Hall mobility after
9.5°K, 5-MeV electron irradiation; measurements at
9.5°K after each anneal

RT-13118

Figure 4-13. Isochronal anneal (10 min) of electrical conductivity after 9.5°K, 5-MeV electron irradiation; measurements at 9.5°K after each anneal

28

made at 9.5°K after anneals at the temperatures indicated by the data points. The carrier density (Figure 4-11) recovered to approximately the preirradiation value, with the major annealin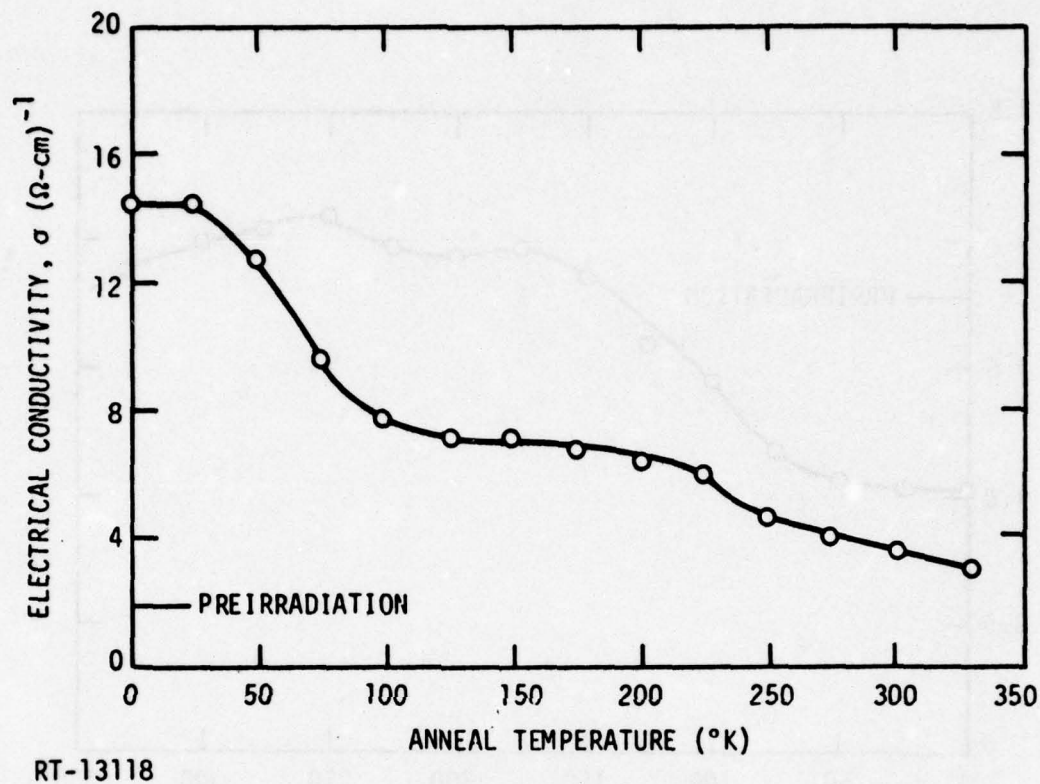g stage centered at about 65°K. The mobility recovered during anneal (Figure 4-12) and overshot the preirradiation mobility after the 150°K anneal. The mobility then decreased after the 250°K anneal and approached the preirradiation mobility after the 330°K anneal. Similar anneal of carrier density and mobility was previously observed for higher-carrier-density n-type samples whose preirradiation carrier density was about $1.5 \times 10^{15} cm^{-3}$ (Ref. 3). Recovery of the electrical conductivity, shown in Figure 4-13, reflects the recovery of the mobility and carrier density during anneal.

During irradiation, the steady-state photoconductivity was monitored only at the irradiation temperature of 9.5°K. During anneal, however, the temperature was decreased to 6.3°K to monitor the recovery of the steady-state photoconductivity at the lower temperature also. The recovery of the steady-state photoconductivity at these temperatures is shown in Figure 4-14. For anneal temperatures below 100°K ($n > 3 \times 10^{14} cm^{-3}$), the two signals are nearly equal. For anneal temperatures above 100°K ($n < 3 \times 10^{14} cm^{-3}$), the 6.3°K signal continues to increase and approach the preirradiation value and the 9.5°K signal retraces the carrier density dependence observed during the irradiation (see Figure 4-23).

4.1 STEADY-STATE PHOTOCONDUCTIVITY

4.1.1 Temperature Dependence

The temperature dependence of the steady-state photoconductivity before irradiation and during cooldown after several isochronal anneals after irradiation is shown in Figure 4-15. As can be seen in the figure, the steady-state photoconductivity signal before irradiation falls in a valley at the irradiation temperature. The effect of the irradiation was to move the peak that precedes this valley and also the valley to higher temperature, as shown by the curves taken after the 200, 250, and 300°K isochronal anneals. As the valley moves to higher temperatures (to the left in Figure 4-15) with irradiation and increased carrier density, the effect is
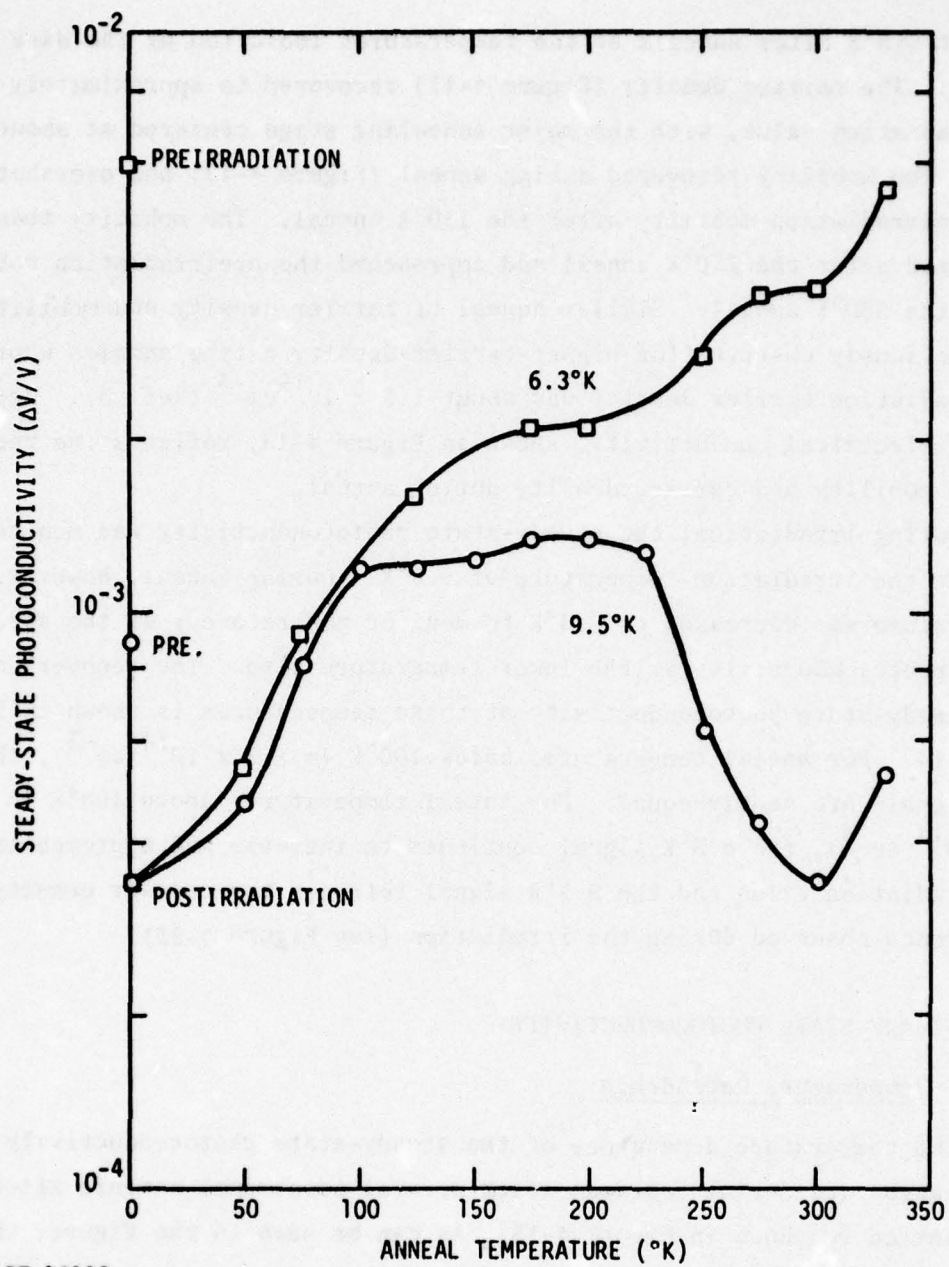
29

RT-13119

Figure 4-14. Isochronal anneal of steady-state photoconductivity after 9.5°K, 5-MeV electron irradiation; measurements at 6.3 and 9.5°K after each anneal
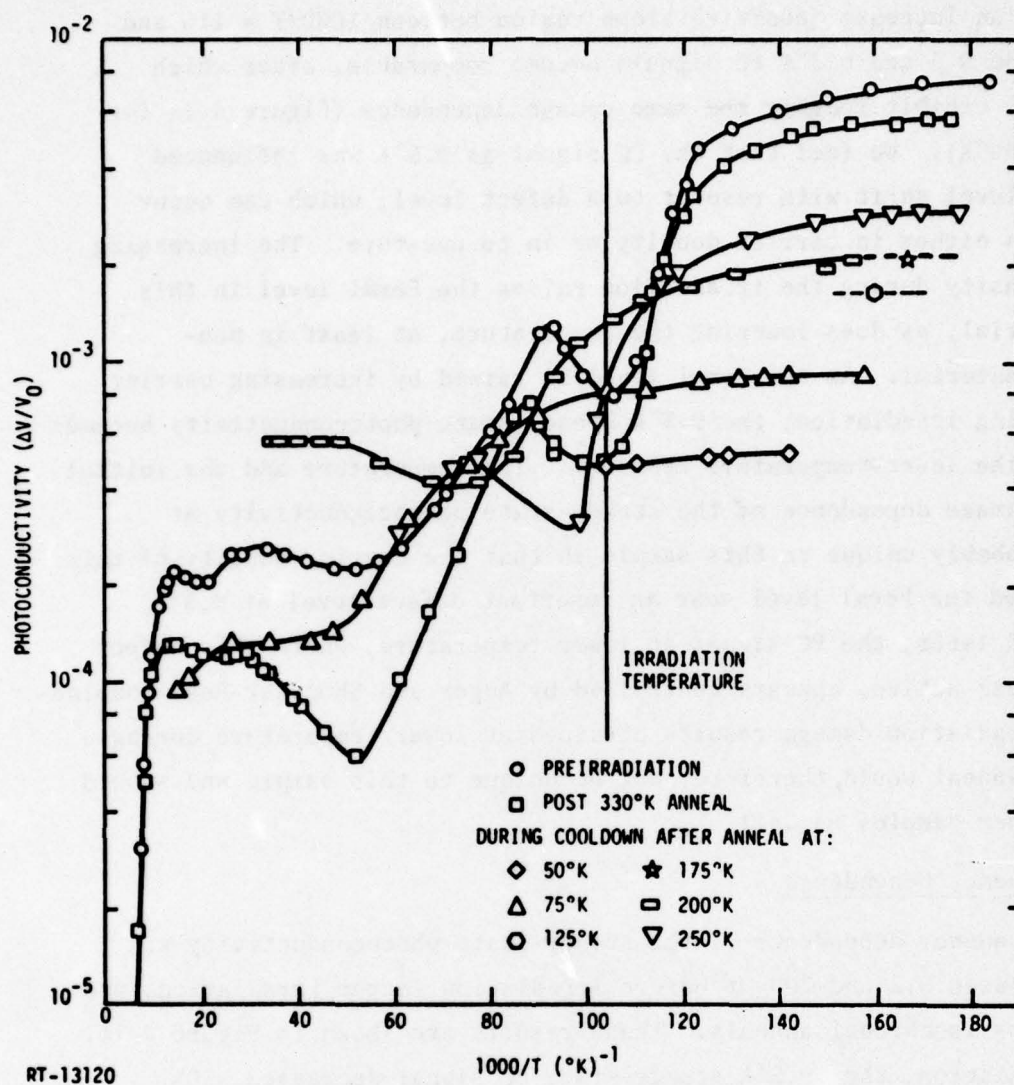
30

Figure 4-15. Temperature dependence of steady-state photoconductivity before irradiation and after various isochronal anneals

31

to first decrease the 9.5°K steady-state PC signal; this decrease is then followed by an increase (positive slope region between 1000/T = 110 and 12) until the 9.5 and 6.3°K PC signals become comparable, after which both signals exhibit roughly the same damage dependence (Figure 4-14 for anneals < 100°K). We feel that the PC signal at 9.5°K was influenced by a Fermi level shift with respect to a defect level, which can occur with changes either in carrier density or in temperature. The increasing electron density during the irradiation raises the Fermi level in this n-type material, as does lowering the temperature, at least in non-degenerate material. As the Fermi level is raised by increasing carrier density during irradiation, the 9.5°K steady-state photoconductivity becomes similar to the lower-temperature behavior. The temperature and the initial radiation damage dependence of the steady-state photoconductivity at 9.5°K is probably unique to this sample in that the carrier density of this sample placed the Fermi level near an important defect level at 9.5°K. As discussed later, the PC signal at lower temperature, where this defect level was less active, appears controlled by Auger and Shockley-Read combination. The radiation damage results obtained at lower temperature during isochronal anneal would, therefore, not be unique to this sample and should apply to other samples as well.

4.1.2 Frequency Dependence

The frequency dependence of the steady-state photoconductivity was measured between 5.2 and 200 Hz before irradiation, after irradiation, and after various isochronal anneals. These results are shown in Figure 4-16. Before irradiation, the 9.5°K steady-state PC signal decreased $\sim$50% between 5.2 and 200 Hz. Photoconductive decay measurements indicated at least two decay time constants of about 1.4×10^{-6} and 0.7×10^{-3} sec. A time constant of 0.57×10^{-3} sec is obtained from Figure 4-16 (pre-irradiation) assuming $\tau = (2\pi f)^{-1}$, where f is the frequency at which the signal has decreased to 50% of its low-frequency value. Similar analysis of the post-330°K anneal data of Figure 4-16 yields a value of 0.4×10^{-3} sec for the longer time constant.
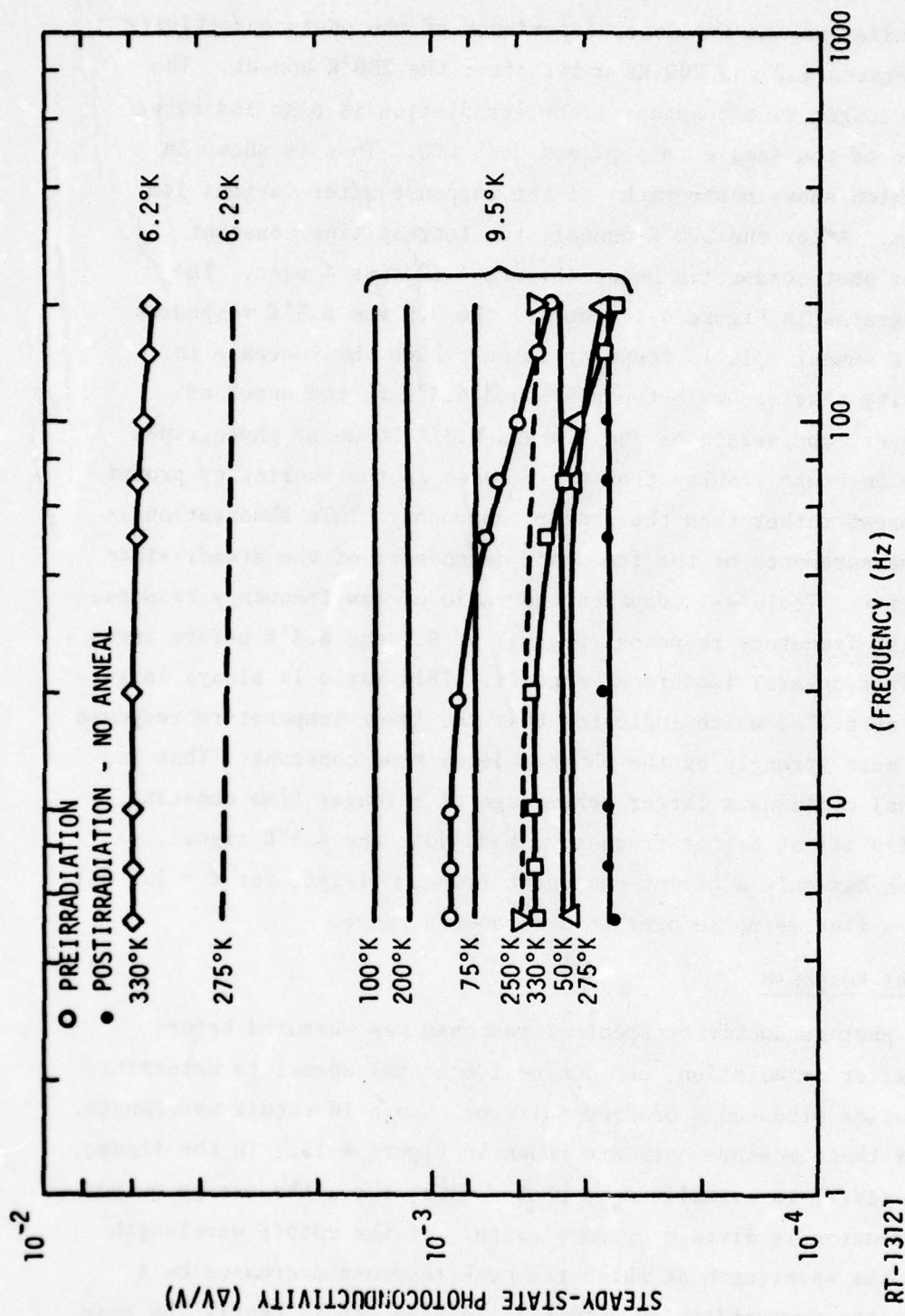
32

Figure 4-16. Frequency dependence of steady-state photoconductivity before irradiation and after various isochronal anneals at temperatures indicated to the left of the curves.
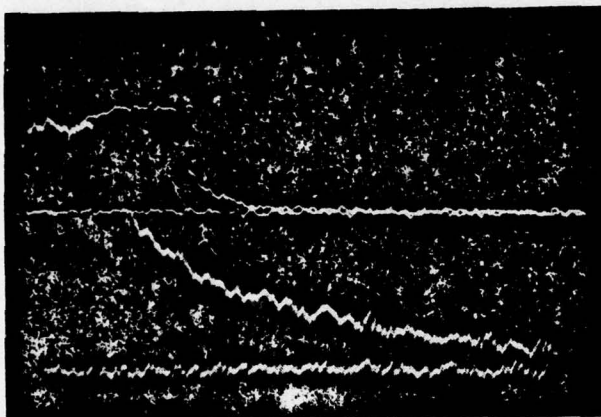
RT-13121

33

After irradiation, no frequency dependence of the photoconductivity was observed between 5.2 and 200 Hz until after the 250°K anneal. The absence of the longer time constant after irradiation is also indicated in the response of the sample to a pulsed GaAs LED. This is shown in Figure 4-17, which shows photographs of the response after various isochronal anneals. After the 100°K anneal, the longest time constant observable from photoconductive decay (Figure 4-17) was 4 μsec. The last two photographs in Figure 4-17 compare the 9.5 and 6.3°K responses after the 330°K anneal. It is tempting to attribute the increase in photoconductivity that occurs between 9.5 and 6.3°K to the onset of trapping; however, comparison of the 9.5 and 6.3°K PC decay photographs shows that the increase results from an increase in the shorter or prompt lifetime component rather than the longer component. This observation is supported by measurements of the frequency dependence of the steady-state photoconductivity. Table 4-1 compares the ratio of low-frequency response (5.2 Hz) to high-frequency response (200 Hz) at 9.5 and 6.3°K before irradiation and after several isochronal anneals. This ratio is always larger at 9.5°K than at 6.3°K, which indicates that the lower-temperature response is controlled more strongly by the shorter decay time constant. That is, the 9.5°K signal contains a larger percentage of a longer time constant, which then rolls off at higher frequency, than does the 6.3°K signal. A PC signal which has only a prompt component (i.e., $\tau < 1/2\pi f$, for $f = 5.2$ Hz) would exhibit a flat response over this frequency range.

4.1.3 Spectral Response

The 10°K photoconductivity spectral response was measured before irradiation, after irradiation, and during isochronal anneal to determine if the irradiation produced a bandgap shift or change in cutoff wavelength. The results of these measurements are shown in Figure 4-18. In the figure, the PC signal ($\Delta V/V$) is normalized to photon flux; i.e., the energy output of the monochromator is divided by wavelength. If the cutoff wavelength is defined as the wavelength at which the peak response decreases by a factor of two, the preirradiation cutoff is 14.7 μm and is nearly the same after irradiation and isochronal anneal to 330°K. After irradiation and during anneal, the spectral response measurements did not extend to short

34
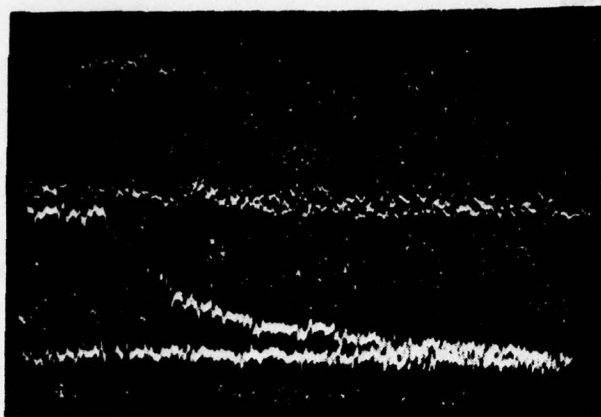
POST 75°K ANNEAL
T = 9.5°K
UPPER TRACE
  H = 20 µsec/div
LOWER TRACE
  H = 2 µsec/div

POST 100°K ANNEAL
T = 9.5°K
UPPER TRACE
  H = 20 µsec/div
LOWER TRACE
  H = 2 µsec/div
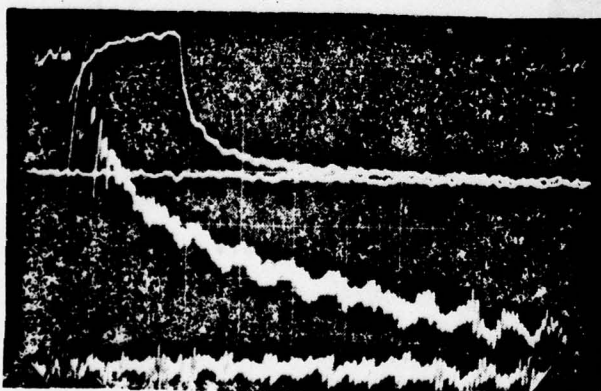
POST 175°K ANNEAL
T = 9.5°K
UPPER TRACE
  H = 20 µsec/div
LOWER TRACE
  H = 2 µsec/div

RT-13122

Figure 4-17.   Photoconductive decay during isochronal anneal after
9.5°K, 5-MeV electron irradiation

35
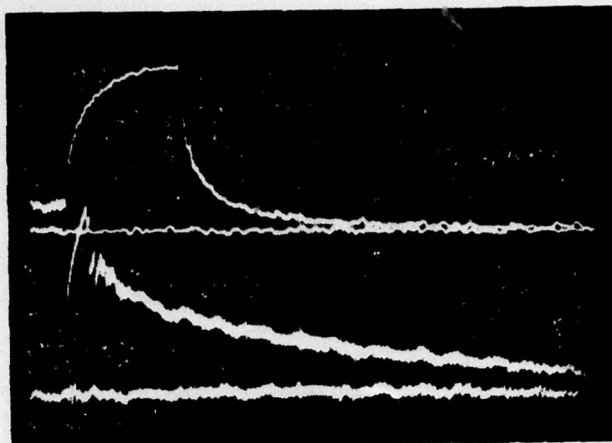
POST 225°K ANNEAL
T = 9.5°K
UPPER TRACE
 H = 20 μsec/div
LOWER TRACE
 H = 2 μsec/div
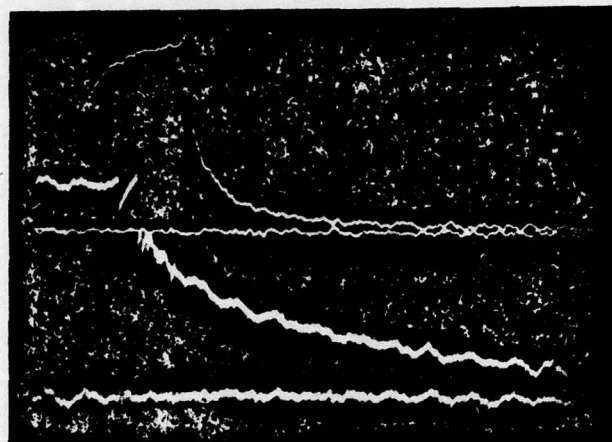
POST 250°K ANNEAL
T = 9.5°K
UPPER TRACE
 H = 20 μsec/div
LOWER TRACE
 H = 2 μsec/div
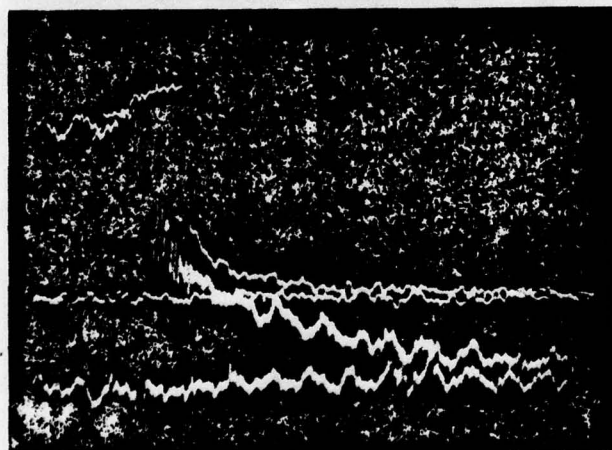
POST 300°K ANNEAL
T = 9.5°K
UPPER TRACE
 H = 20 μsec/div
LOWER TRACE
 H = 2 μsec/div

RT-13123

Figure 4-17 (cont.)

36

POST 330°K ANNEAL
T = 9.5°K
H = 100 μsec/div
V = 0.5 x 10⁻⁴ V/div

POST 330°K ANNEAL
T = 6.3°K
H = 100 μsec/div
V = 2.5 x 10⁻⁴ V/div

RT-13124

Figure 4-17 (cont.)

37
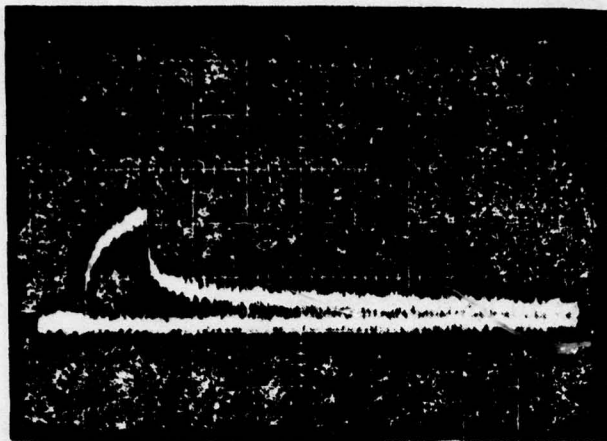
POST 330°K ANNEAL
T = 9.5°K
H = 100 μsec/div
V = 0.5×10^{-4} V/div
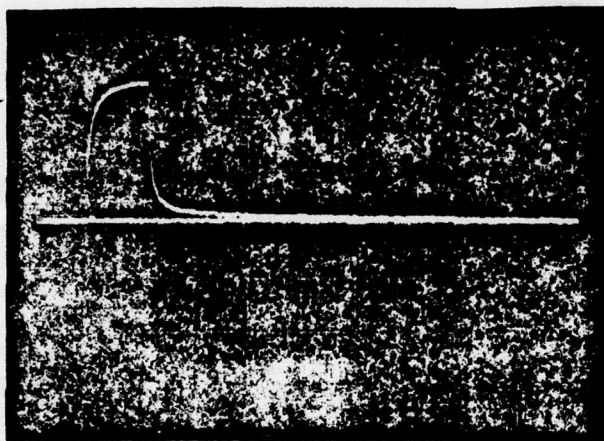
POST 330°K ANNEAL
T = 6.3°K
H = 100 μsec/div
V = 2.5×10^{-4} V/div

RT-13124

Figure 4-17 (cont.)

37

Table 4-1

RATIO OF LOW-FREQUENCY (5.2 Hz) TO HIGH-FREQUENCY (200 Hz)
STEADY-STATE PHOTOCONDUCTIVITY AT 9.5 AND 6.3°K
BEFORE IRRADIATION AND DURING ISOCHRONAL ANNEAL

Condition	Ratio $\frac{5.2 \text{ Hz}}{200 \text{ Hz}}$	
	9.5°K	6.3°K
Preirradiation	1.9	1.31
Postirradiation	1	1
200°K anneal	1	1
225°K anneal	1	1
250°K a-neal	1.11	1.06
275°K anneal	1.20	1.07
300°K anneal	1.38	1.03
330°K anneal	1.64	1.10

Chart legend:
- POSTIRRADIATION - NO ANNEAL
- POST 75°K ANNEAL
- POST 100°K ANNEAL
- POST 175°K ANNEAL
- POST 330°K ANNEAL

Y-axis: RELATIVE RESPONSE (1000, 100, 10)
X-axis: λ (μm) with values 5, 6, 8, 10, 12, 14, 16, 18

PREIRRADIATION label with arrow

RT-13125

Caption: Figure 4-18. Photoconductivity spectral response...

RELATIVE RESPONSE

□ POSTIRRADIATION - NO ANNEAL
○ POST 75°K ANNEAL
△ POST 100°K ANNEAL
◇ POST 175°K ANNEAL
⊟ POST 330°K ANNEAL

1000

100

10

PREIRRADIATION →

5   6   8   10   12   14   16   18

λ (μm)

RT-13125

Figure 4-18. Photoconductivity spectral response before
irradiation and after various isochronal anneals;
PC signal (ΔV/V) normalized to photon flux

39

enough wavelengths to observe a peak in the response. An estimate of
about 50 for the peak value of response after irradiation prior to any
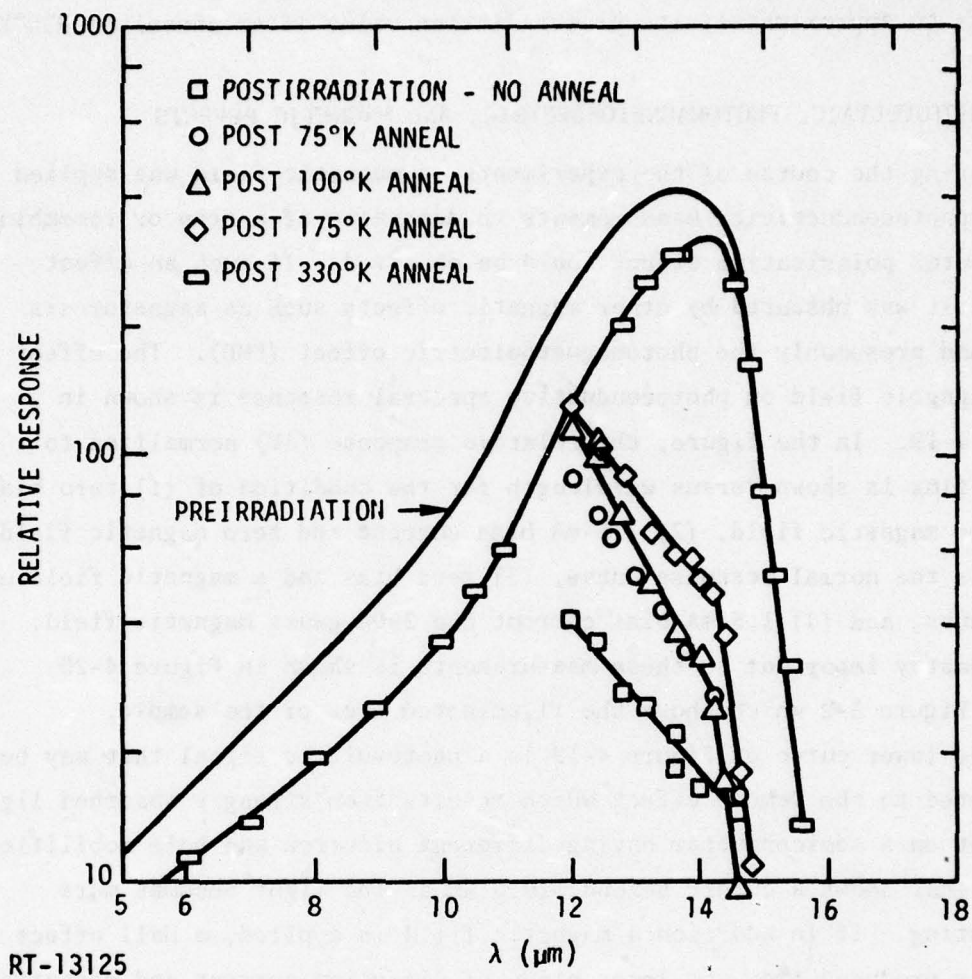anneal results in a cutoff wavelength of 13.3 μm. The cutoff wavelength
recovers to approximately its preirradiation value after anneal to 330°K.

4.2 PHOTOVOLTAIC, PHOTOMAGNETOELECTRIC, AND MAGNETIC EFFECTS

During the course of the experiments, a magnetic field was applied
during photoconductivity measurements to determine if a trap or recombina-
tion center polarization effect could be observed. If such an effect
exists, it was obscured by other magnetic effects such as magnetoresis-
tance and presumably the photomagnetoelectric effect (PME). The effect
of a magnetic field on photoconductive spectral response is shown in
Figure 4-19. In the figure, the relative response (ΔV) normalized to
photon flux is shown versus wavelength for the condition of (1) zero bias
and zero magnetic field, (2) 1.5-mA bias current and zero magnetic field,
which is the normal response curve, (3) zero bias and a magnetic field of
2900 gauss, and (4) 1.5-mA bias current and 2900-gauss magnetic field.
The geometry important to these measurements is shown in Figure 4-20,
and in Figure 3-2 which shows the illuminated area of the sample.

The lower curve of Figure 4-19 is a photovoltaic signal that may be
attributed to the Dember effect which results from strongly absorbed light
incident on a semiconductor having different electron and hole mobilities.
This signal shows a cutoff beyond ∿10.5 μm as the light becomes more
penetrating. If in addition a magnetic field is applied, a Hall effect
(PME) is produced from the interaction of diffusion current and magnetic
field. This effect also disappears when the incident light becomes
penetrating, as shown in Figure 4-19 (□ data points).

The upper curve of Figure 4-19 was taken with bias and magnetic field,
and includes both the PME effect and the effect of magnetoresistance. For
a given bias current, the magnetic field increases the sample resistance
which increases the bias voltage V and also the PC signal (ΔV) propor-
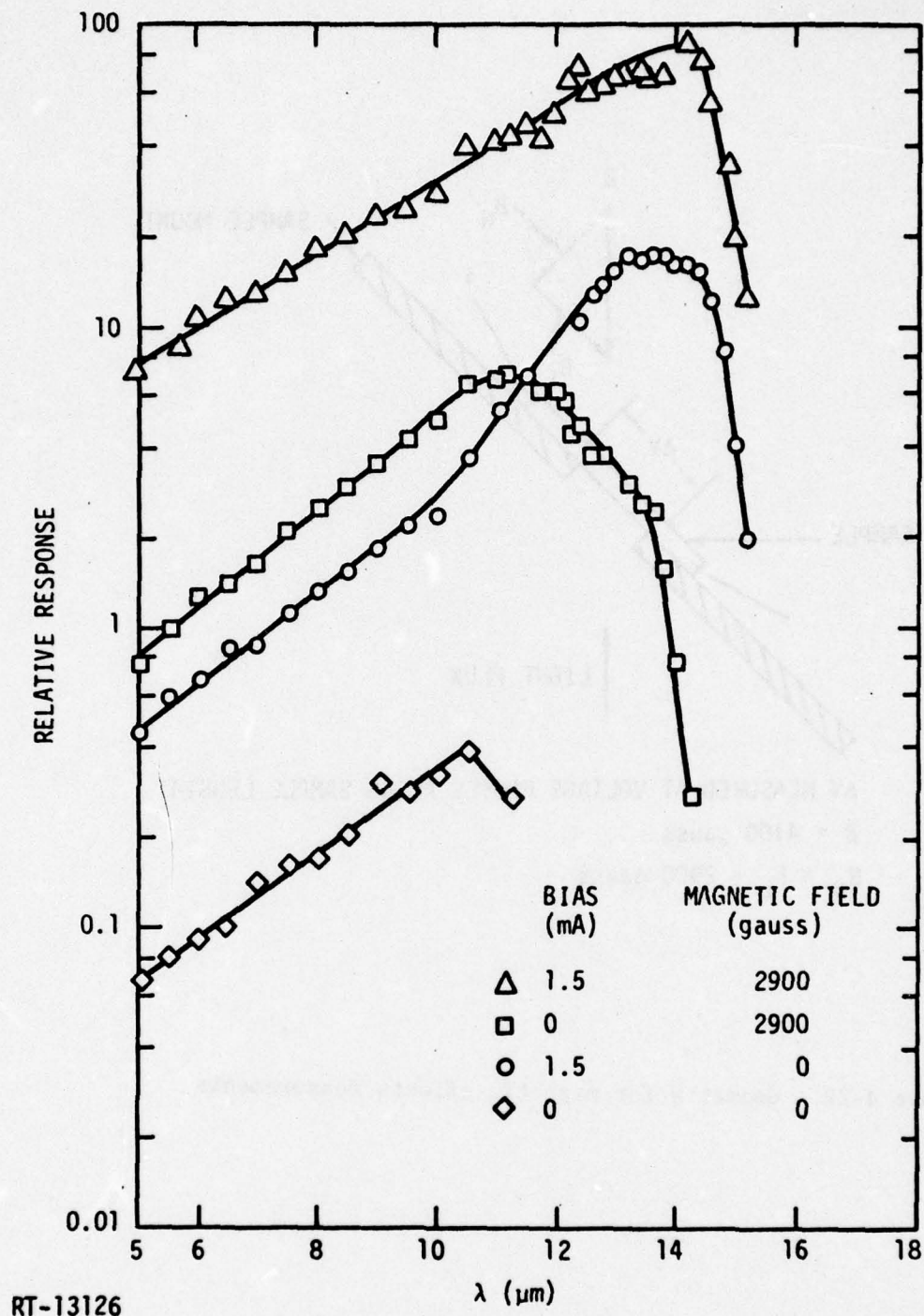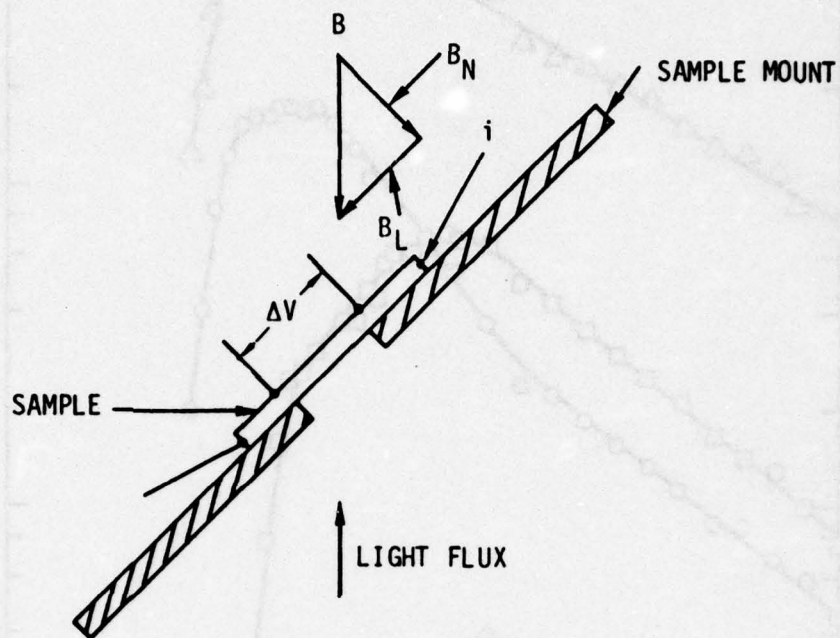tionally. At 5 μm, where the PME contribution is large, the signal with

40

Figure 4-19. Photoconductivity spectral response with magnetic
field; PC signal (ΔV) normalized to photon flux

RT-13126

41

ΔV MEASURED AT VOLTAGE PROBES ALONG SAMPLE LENGTH

B = 4100 gauss

$B_N = B_L$ = 2900 gauss

RT-13127

Figure 4-20. Geometry for magnetic effects measurements

42

bias and magnetic field is a factor of 10 greater than for the same bias only. At longer wavelength (14 μm), where the PME signal vanishes, the ratio of signals is ~4, which is about the value expected due to the magnetoresistance, $\Delta\rho/\rho$ (Figure 4-21) for a normal magnetic field of 2900 gauss.

The temperature dependence of the effect referred to as PME is shown in Figure 4-22. This figure also shows, for comparison, the temperature dependence of the normal photoconductivity signal for a 1000°K blackbody before the sample was irradiated and after the 330°K anneal. This figure is included primarily to show the rather sharp cutoff in the PME signal that occurs at 10°K before irradiation and about 12°K after irradiation and anneal. The reason for the cutoff is not known; however, the cutoff appears to be correlated with the peak and valley in the normal PC signal and the small abrupt change in carrier density. Bube (Ref. 5) states that the PME effect vanishes when one carrier mobility is effectively zero. Since this is normally the case for HgCdTe as the mobility ratio is large, it is difficult to attribute the cutoff to the onset of a carrier (hole) becoming immobilized by trapping at the lower temperature. In Figure 4-22, the PME signal is given as ΔV (volts), while the PC signal is the ratio $\Delta V/V_0$.

4.3 CARRIER ADDITION

The curve of carrier density versus fluence in Figure 4-7 shows an increasing rate of electron addition with increasing fluence (or density). At the highest fluence, the introduction rate approaches the constant rate measured at this temperature for high-density samples (Ref. 3). In Reference 3, an even more pronounced nonlinear electron introduction curve obtained at 80°K was explained using a defect model which included a donor level high in the conduction band and an acceptor level close to the valence band. The nonlinear electron introduction rate resulted from the interaction of the lower tail of the Fermi-Dirac distribution with the acceptor level. For low electron densities, the Fermi level was relatively close to the acceptor level, and their interaction caused the net rate of increase
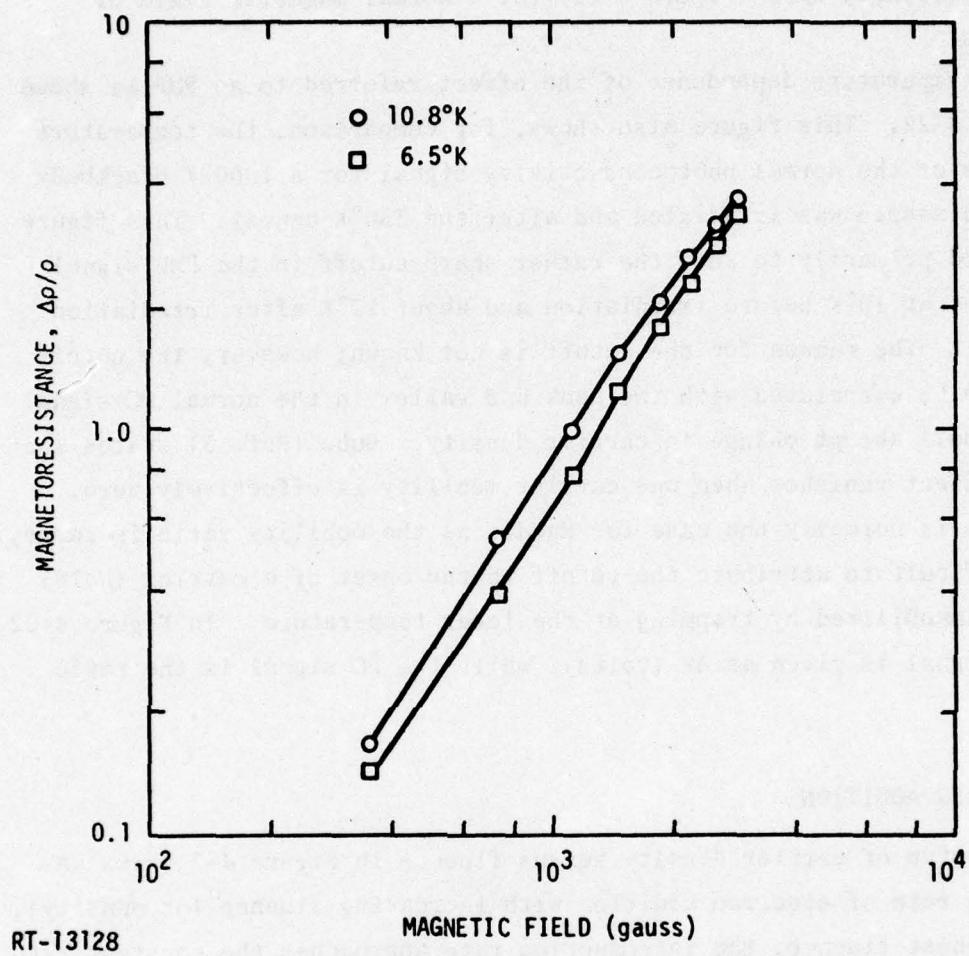
43

RT-13128

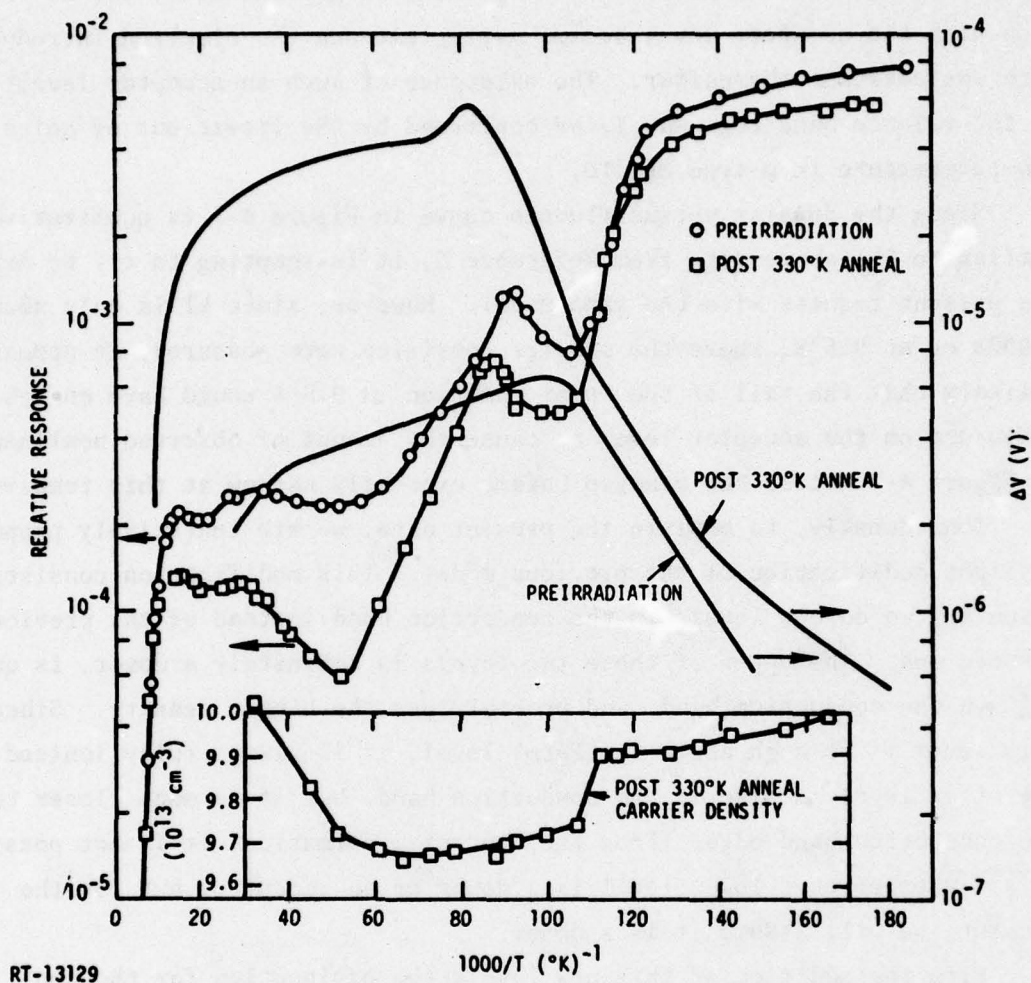Figure 4-21. Magnetoresistance versus magnetic field
normal to current flow.

44

Figure 4-22. Comparison of temperature dependence of (1) photoconductivity signal (ΔV/V) with bias and zero magnetic field and (2) signal (ΔV) with magnetic field and zero bias

of electrons in the conduction band to be less than the linear rate of creation of new donors by the radiation. However, as the electron density increased with the radiation, the Fermi level moved farther from the acceptor level. Eventually, at sufficiently large densities, the interaction with the acceptor level became negligible and the electron introduction rate was constant thereafter. The existence of such an acceptor level close to the valence band edge was later confirmed by the freeze-out of holes at low temperature in p-type HgCdTe.

Since the density versus fluence curve in Figure 4-7 is qualitatively similar to the above data from Reference 3, it is tempting to try to explain the present results with the same model. However, since kT in only about 0.0008 eV at 9.5°K, where the carrier densities were measured, it appears unlikely that the tail of the Fermi function at 9.5°K would have enough influence on the acceptor level to cause the amount of observed nonlinearity in Figure 4-7 unless the bandgap became extremely narrow at this temperature.

Consequently, to explain the present data, we are tentatively proposing a slight modification of the previous model. This modification consists of assuming two defect levels in the conduction band instead of the previously assumed one. The upper of these two levels is definitely a donor, is quite high in the conduction band, and probably has the higher density. Since this level is so high above the Fermi level, it is always fully ionized. The other level is also in the conduction band, but it is much closer to the conduction band edge. From the present information, it is not possible to say whether this lower level is a donor or an acceptor, but for the present, we will assume it is a donor.

With the addition of this new level, the explanation for the non-linear electron density versus fluence curve in Figure 4-7 is exactly equivalent to the previous explanation except that now the tail of the Fermi function interacts with this level instead of with the acceptor near the valence band edge to produce the nonlinearity. The sole basis for introducing this level is to provide a level sufficiently close to the Fermi level to produce enough interaction to cause the magnitude of the observed effect.

46

The addition of this new level is not in conflict with the previous analyses for the 80°K data (Ref. 3). First, for a sizable part of the density range in Reference 3, the Fermi level is well below this new level, so it would be fully ionized and its presence would not be seen. Also, the gradual curvature of the curve in Figure 4-7 probably means that this new level has a relatively low density. Thus, its effect could well have been overshadowed in the 80°K data by the nonlinear effect of the higher-density acceptor level.

Possible additional evidence for this level is provided by the pre-irradiation curve of electron density versus temperature in Figure 4-4. Starting from the lowest temperature, the electron density before irradiation first decreases slightly with increasing temperature and then increases. This final increase is due to the intrinsic carrier density at high temperatures. However, the initial decrease could be due to this new level. If the Fermi level at the lowest temperature on the preirradiation curve is slightly below this defect level, the level will be almost fully ionized at that temperature. However, as the temperature increases, the tail of the Fermi function will become broader and will reach up to the defect level and convert some of them from (+) to zero [or zero to (-)], thus causing the density of free electrons to decrease slightly. A similar but more pronounced effect was observed in p-type PbSnTe (Ref. 6) and was explained by a similar model. The fact that the slight decrease in electron density is not observed in the curves after irradiation and partial anneal (Figure 4-4) could be because the change in electron density is small and hard to see at the larger densities, or else the Fermi level is above the level at these densities so the decrease would not occur with increasing temperature.

The existence of this level may also help to explain the humps in the curve of steady-state lifetime (photoconductivity) versus temperature, as discussed in the next section.

4.4 LIFETIMES

The complicated trends of the curves of steady-state photoconductivity ($\Delta V/V$) with temperature, radiation, and annealing in Figure 4-15 undoubtedly mean that different recombination processes dominate in different temperature and density ranges. The processes usually considered are Auger and radiative recombination, Shockley-Read recombination through one or more defect levels, and possibly trapping. Unfortunately, not enough is known as yet about the defect and trap levels in HgCdTe and the various parameters in the formulas for Auger and radiative recombination to give a definite quantitative explanation for all these data. The most that can be done for the present is to suggest possible explanations for some of the trends.

It is generally accepted that the high-temperature (intrinsic) region is dominated by Auger recombination because the lifetime goes as $1/n^2$, where n is the electron density. The first peak at high temperatures is usually ascribed to Shockley-Read recombination becoming more important with decreasing temperature and starting to dominate the Auger recombination. The fact that this decreasing trend due to Shockley-Read recombination reverses itself and increases at lower temperatures has sometimes been attributed to minority-carrier trapping (Ref. 7). However, the additional structure in the present data must mean that still other effects come into prominence. Also, there is evidence that the lifetimes at the lowest temperatures ($\sim$6.3°K) are due to Auger recombination at high carrier densities.

In Figure 4-23, $\Delta V/V$ at 9.5 and 6.3°K after various annealing temperatures is plotted versus the corresponding electron densities. At low densities, the photoconductivity response ($\Delta V/V$) at 6.3°K goes as $1/n$, and for carrier densities $>6 \times 10^{14}$ e/cm^2, both the 6.3 and 9.5°K signals exhibit carrier density dependence greater than $1/n$. As will be shown later, the $1/n$ dependence at the lower density results from the dependence of $\Delta V/V$ on carrier density n rather than on a change in carrier lifetime.

During irradiation, the steady-state photoconductivity signal (SSPC) was measured at the irradiation temperature of 9.5°K. During the isochronal
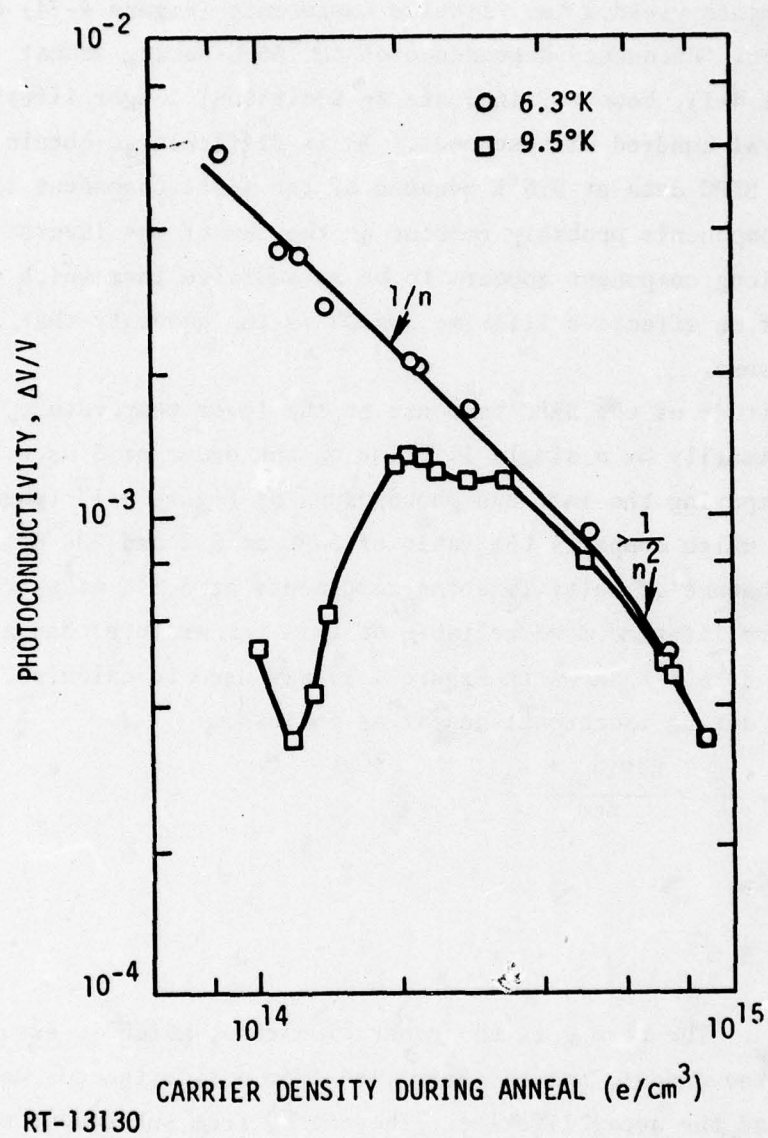
48

Figure 4-23. Steady-state photoconductivity at 9.5 and 6.3°K
versus carrier density during isochronal anneal

RT-13130

49

anneal, the SSPC was measured at both 9.5 and 6.3°K, and lifetime measurements by photoconductive decay were made only at 9.5°K. The photoconductive decay measurements yielded two lifetime components (Figure 4-24) of about 1.5 and 10 μsec. Frequency dependence of the SSPC during anneal (Figure 4-16 and Table 4-1), however, indicate an additional longer lifetime on the order of several hundred microseconds. It is difficult to obtain lifetime data from the SSPC data at 9.5°K because of the multi-component lifetimes. The shorter components probably combine as the sum of the inverse lifetimes; however, the long component appears to be an additive term which complicates calculation of an effective lifetime, which is the quantity that controls the SSPC response.

The amplitude of the SSPC response at the lower temperature, 6.3°K, was controlled primarily by a single lifetime on the order of 3 μsec. This can be seen by comparing the last two photographs of Figure 4-17 (page 37) and in Table 4-1, which compares the ratio of SSPC at 5.2 and 200 Hz at 6.3 and 9.5°K. The absence of multi-lifetime components at 6.3°K makes calculation of an effective lifetime more reliable at this temperature than at 9.5°K. The SSPC data at 6.3°K shown in Figure 4-14 was used to calculate the effective lifetime during isochronal anneal as follows.

$$\frac{\Delta V}{V} = \frac{\Delta \sigma}{\sigma} = \frac{g\tau e(\mu_n + \mu_p)}{ne\mu_n}$$

which reduces to

$$\frac{\Delta V}{V} = \frac{g\tau}{n}$$

since $\mu_n \gg \mu_p$. The term g is the generation rate, which is assumed constant during the anneal, and is determined from a simultaneous measurement of $\Delta V/V$, n, and the decay lifetime. Therefore, from subsequent measurements of $\Delta V/V$ and n, the lifetime τ can be determined from

$$\tau = \frac{\Delta V}{V} \times \frac{n}{g} \, .$$

[The assumption that g is constant during anneal is not completely true since a shift in cutoff wavelength was observed (Figure 4-18). However, estimates indicate that the change in cutoff wavelengths would change the generation rate by less than 20%.]
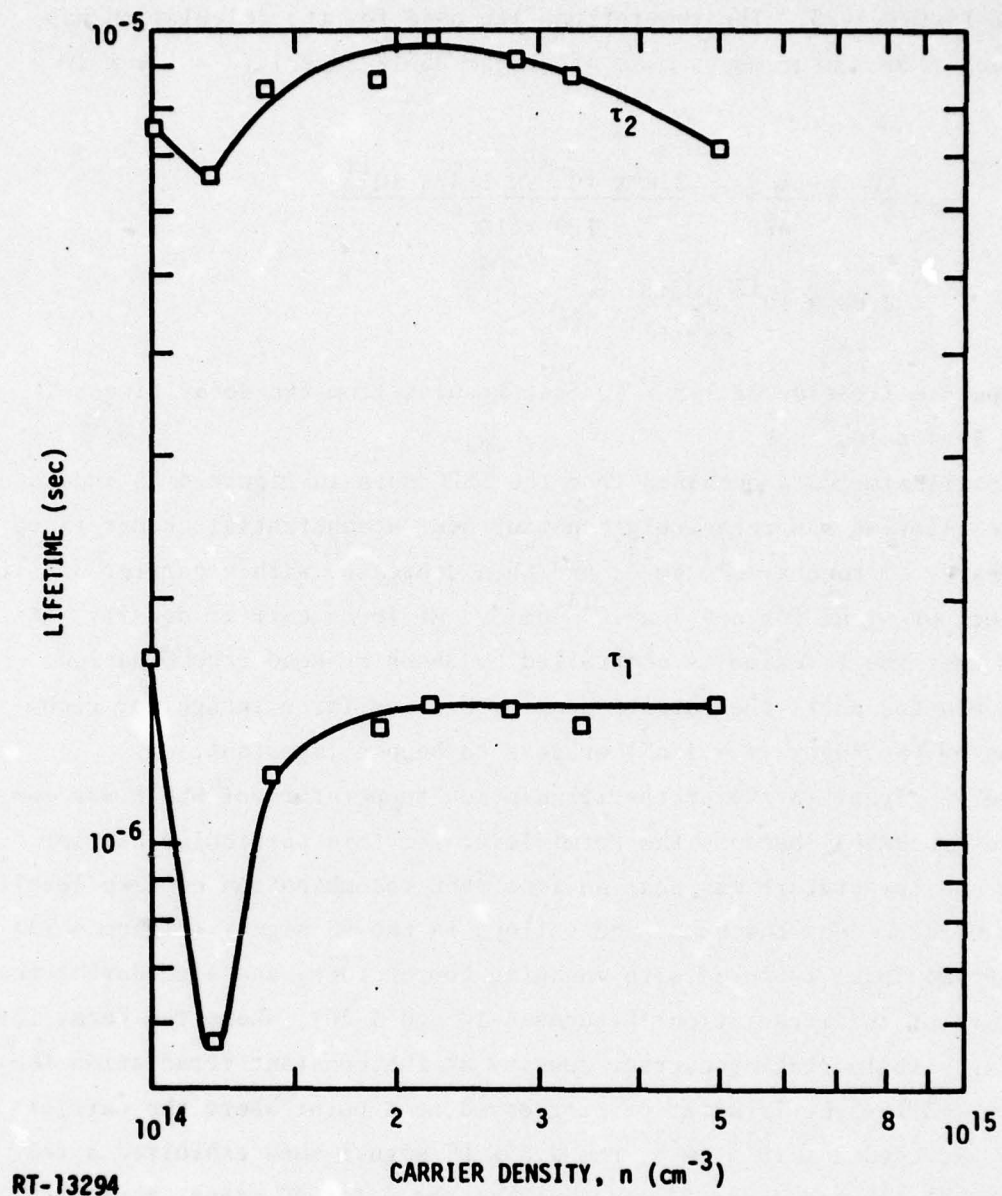
50

RT-13294

Figure 4-24. Photoconductive decay lifetime at 9.5°K versus
carrier density during isochronal anneal

51

Carrier lifetime at 6.3°K versus carrier density during anneal is shown in Figure 4-25. The generation rate used for the calculation was determined from measurements made after the 250°K anneal ($n = 1.4 \times 10^{14}$ cm^{-3}):

$$g = \frac{\Delta V}{V} \times \frac{n}{\tau_{eff}} = \frac{2.8 \times 10^{-3} \times 1.4 \times 10^{14}}{1.9 \times 10^{-6}}$$

$$= 2.08 \times 10^{17} \frac{pairs}{cm^3 - sec} \; .$$

The effective lifetime of 1.9×10^{-6} sec results from two decay times of 2.3 and 10.4×10^{-6} sec.

The lifetime data obtained from the SSPC data in Figure 4-25 indicates that the lifetime was relatively constant over a substantial change in carrier density (2 to 6×10^{14} cm^{-3}) and then decreases with a carrier density dependence of $\sim 1/n^2$ for $n > 7 \times 10^{14}$ cm^{-3}. At lower carrier density, it appears that the lifetime is controlled by Shockley-Read recombination, which dominates until the carrier density becomes large enough for recombination by the Auger ($\tau \propto 1/n^2$) process to become important.

The PC signal ($\Delta V/V$) at the irradiation temperature of 9.5°K was complicated presumably because the Fermi level for this particular carrier density and temperature was near an important recombination or trap level. This is evidenced by the humps and valleys in the PC signal (Figure 4-15) as the Fermi level is moved with changing temperature, and also during the early part of the irradiation (Figures 4-10 and 4-26), where the Fermi level is rising with increasing carrier density at the constant irradiation temperature. After the irradiation progressed to a point where the carrier density exceeded 2×10^{14} cm^{-3}, the 9.5°K PC signal then exhibited a relatively well behaved damage dependence, as the 6.3°K PC signal throughout the anneal. This is shown in Figure 4-10, which is the 9.5°K PC fluence dependence, and also in Figure 4-23, which is a plot of the 9.5 and 6.3°K PC signals as a function of carrier density during the anneal.

The above partially answers the question as to whether the results obtained are unique to this sample. The photoconductivity results at 9.5°K during the early stage of the irradiation are probably unique in that the preirradiation carrier density placed the Fermi level in the

52

RT-13295

LIFETIME, τ (sec)

10^{-6}

$1/n^2$

O τ CALCULATED FROM STEADY-STATE PHOTOCONDUCTIVITY (see p. 49)

□ $\tau_{eff} = [(1/\tau_1) + (1/\tau_2)]^{-1}$; τ_1 AND τ_2 MEASURED BY PHOTOCONDUCTIVE DECAY

CARRIER DENSITY DURING ISOCHRONAL ANNEAL, n (cm^{-3})
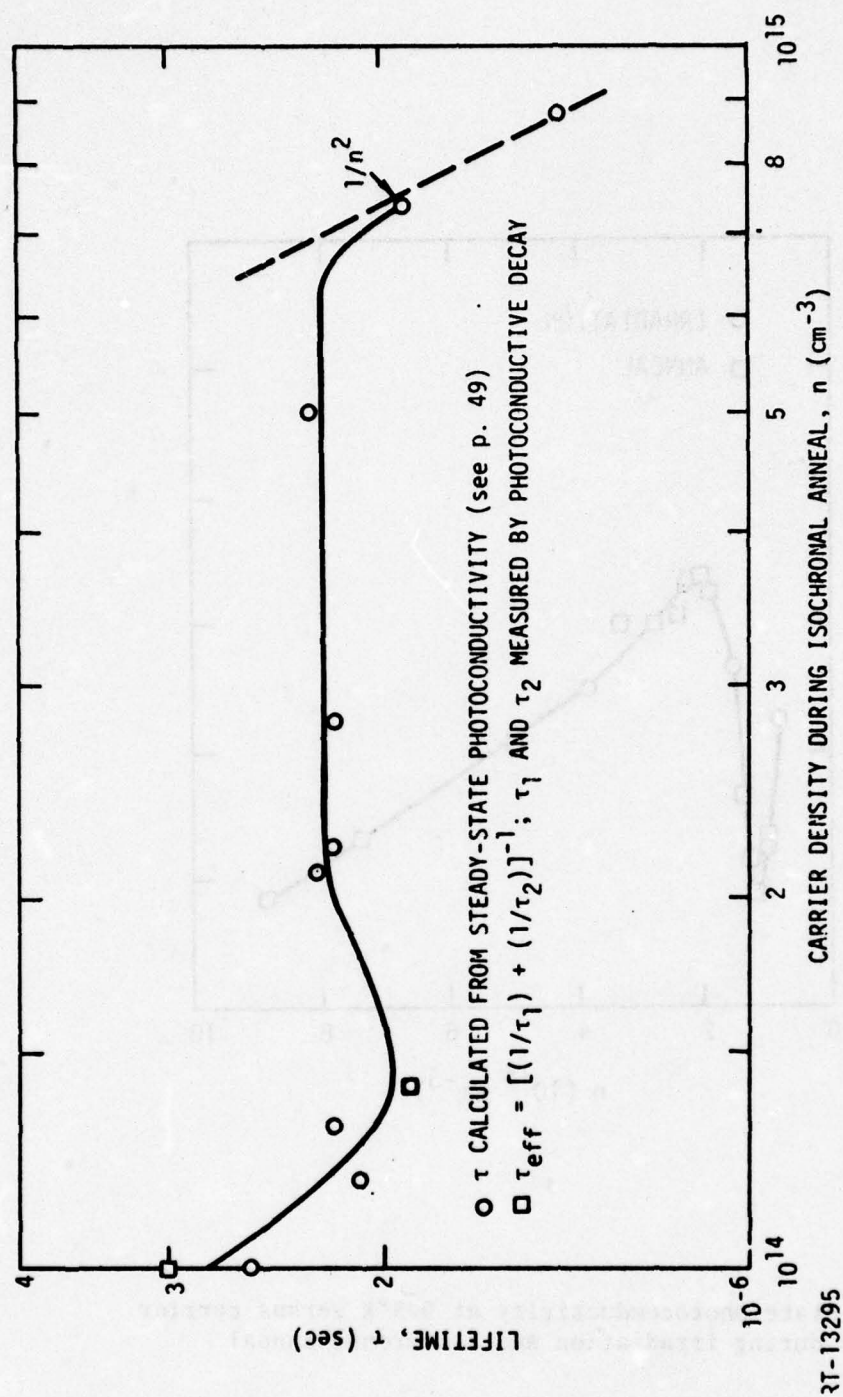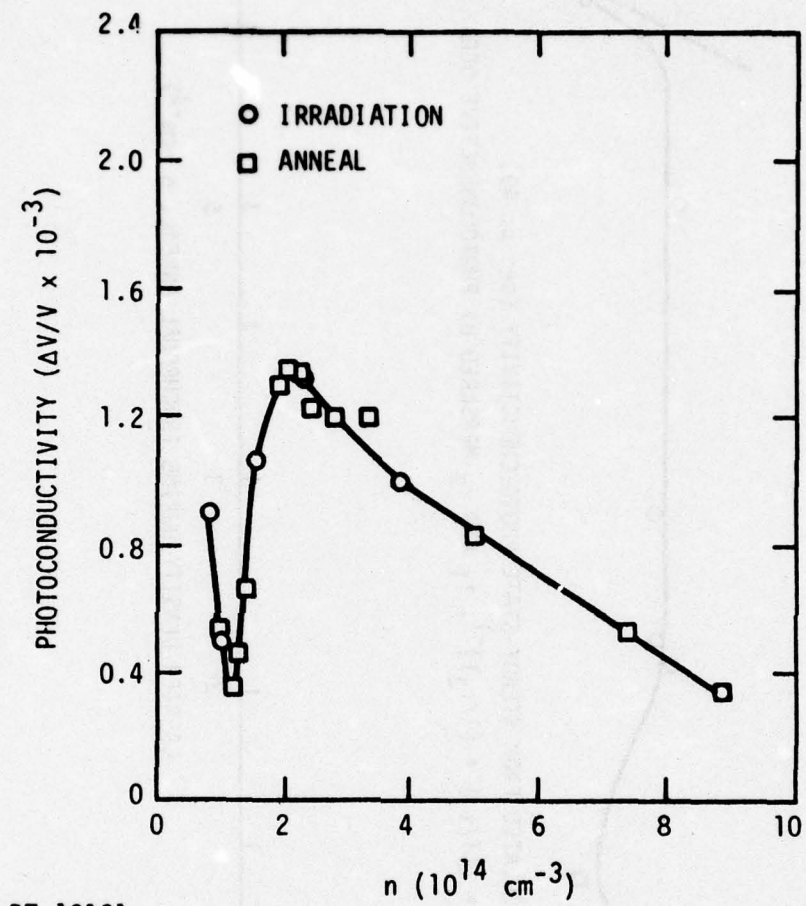
Figure 4-25. Carrier lifetime at 6.3°K (calculated from steady-state photoconductivity) versus carrier density during anneal

53

RT-13131

Figure 4-26. Steady-state photoconductivity at 9.5°K versus carrier
density during irradiation and isochronal anneal

54

proximity of a defect level at this temperature. The 6.3°K photoconductivity and also the 9.5°K photoconductivity for $n > 2 \times 10^{14}$ cm^{-3} are probably not unique to this sample since they exhibit a reasonable carrier density dependence. There were no important features in carrier density, Hall mobility, or conductivity that would indicate that the results obtained are unique to this sample.

We do not have a definite explanation for the other peaks and valleys which occur between the intrinsic and the low-temperature regions and which shift their positions under irradiation and annealing. A possibility is that different Shockley-Read centers become important in restricted temperature ranges as the Fermi level changes and makes the defects better or poorer recombination centers. This explanation is qualitatively compatible with the effects of radiation and annealing since the electron density and, therefore, the Fermi level are changed in the process. The acceptor level near the valence band in the original defect model (Ref. 3) and the level near the conduction band edge that was proposed in Section 4.3 are two possible candidates for these recombination levels.

5. GAMMA AND NEUTRON IRRADIATION OF SAMPLE I-1 at 10°K

Sample I-1 was gamma-irradiated at 10°K to a total dose of $\sim 1 \times 10^6$ rad(Si). The sample was then isochronal-annealed to 340°K and then neutron-irradiated at 10°K to a fluence of 1.2×10^{13} n/cm^2 (>10 keV). After the neutron irradiation, the sample was again isochronal-annealed to 340°K.

Sample Preparation

Sample I-1 was fabricated from a bar of $Hg_{0.8}Cd_{0.2}Te$ that was originally 2 cm long, 0.283 cm wide, and 0.6 mm thick. The sample was cut to a length of 0.9 cm using a 10-mil wire saw and silicon carbide slurry. The sample was then lapped with $A\ell_2O_3$ and etched 20-sec with methanol-5% bromine to obtain a sample thickness of 0.39 mm. Indium solder contacts were then applied as described in Section 3.2. Sample dimensions and probe locations are shown in Figure 5.1. Since the voltage probe spacing was an appreciable fraction of the total sample length, an additional Hall probe was added so that Hall measurements could be made at the center of the sample rather than using the voltage probes and a balancing potentiometer, as discussed in Section 3.4. Use of the voltage probes and balancing potentiometer resulted in approximately a 20% error in carrier density and mobility that was avoided by the use of opposite Hall probes.

Prior to irradiation, sample I-1 had an extrinsic electron density $(N_D - N_A)$ of $\sim 1 \times 10^{14}$ cm^{-3} and a relatively large low-temperature Hall mobility of about 3×10^5 cm^2/V·sec, indicative of a small to moderate compensation. The preirradiation temperature dependence of the carrier density, Hall mobility, and electrical conductivity is given in Figures 5.2, 5.3, and 5.4.

56

VOLTAGE PROBES

0.357

HALL PROBES

I

0.283

0.90

DIMENSIONS IN cm
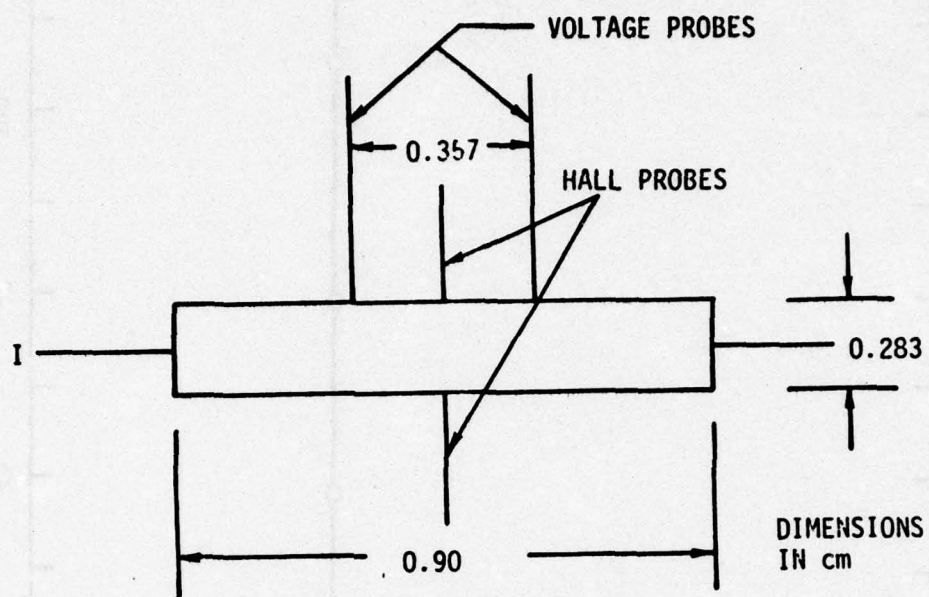
RT-14293

SAMPLE THICKNESS = 0.039 cm

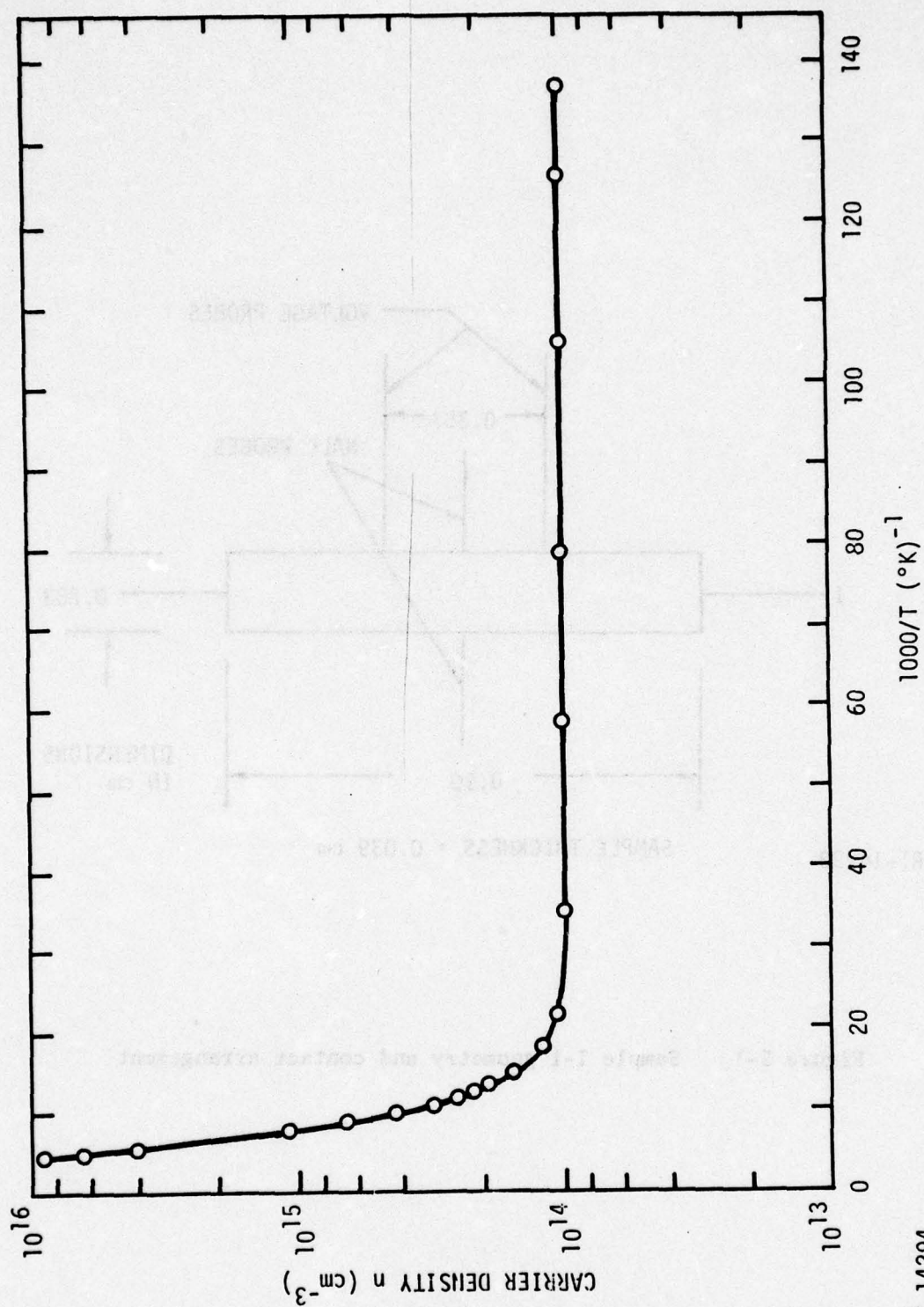Figure 5-1. Sample I-1 geometry and contact arrangement

Figure 5-2. Preirradiation temperature dependence of the carrier density, Sample I-1
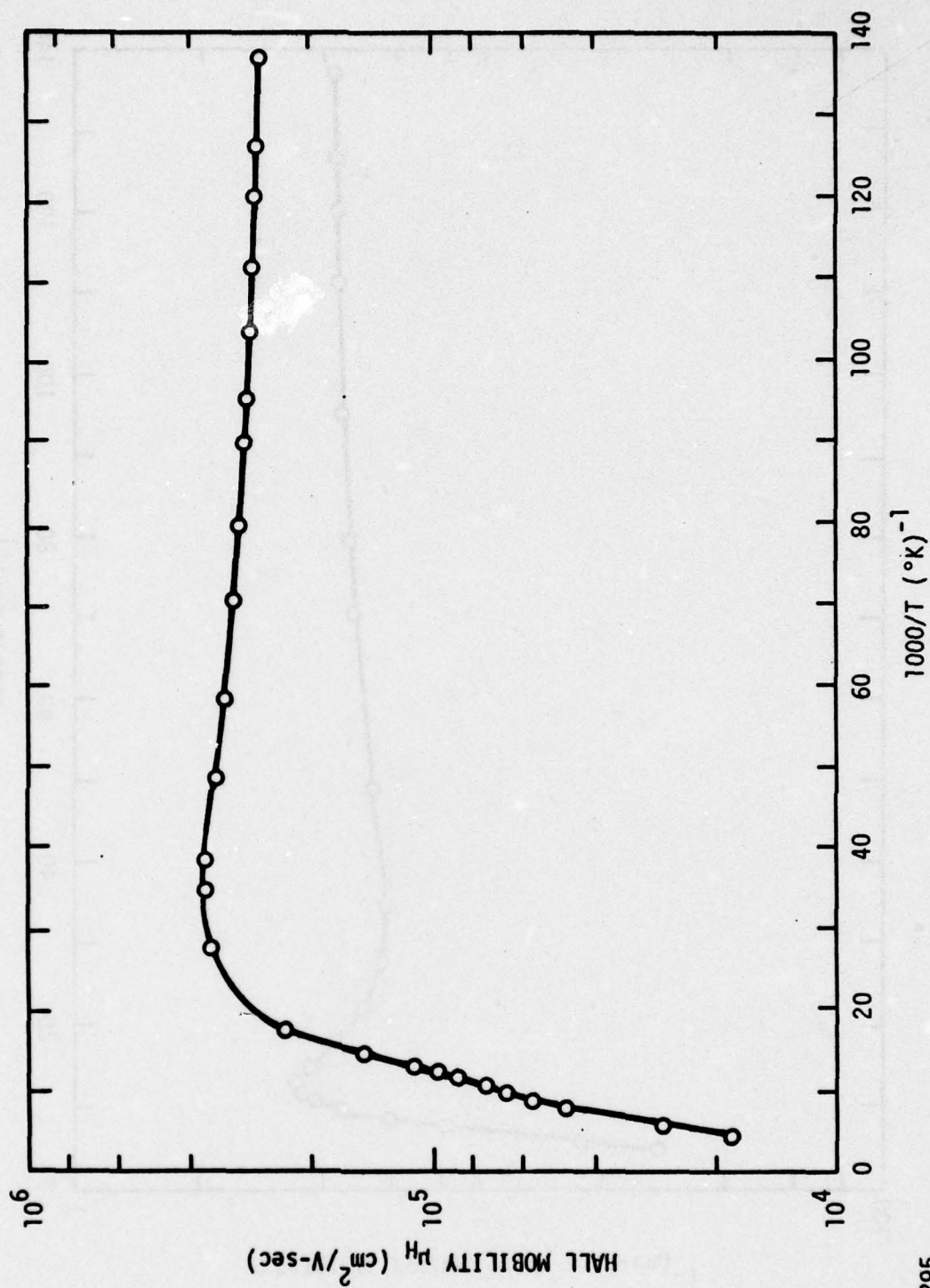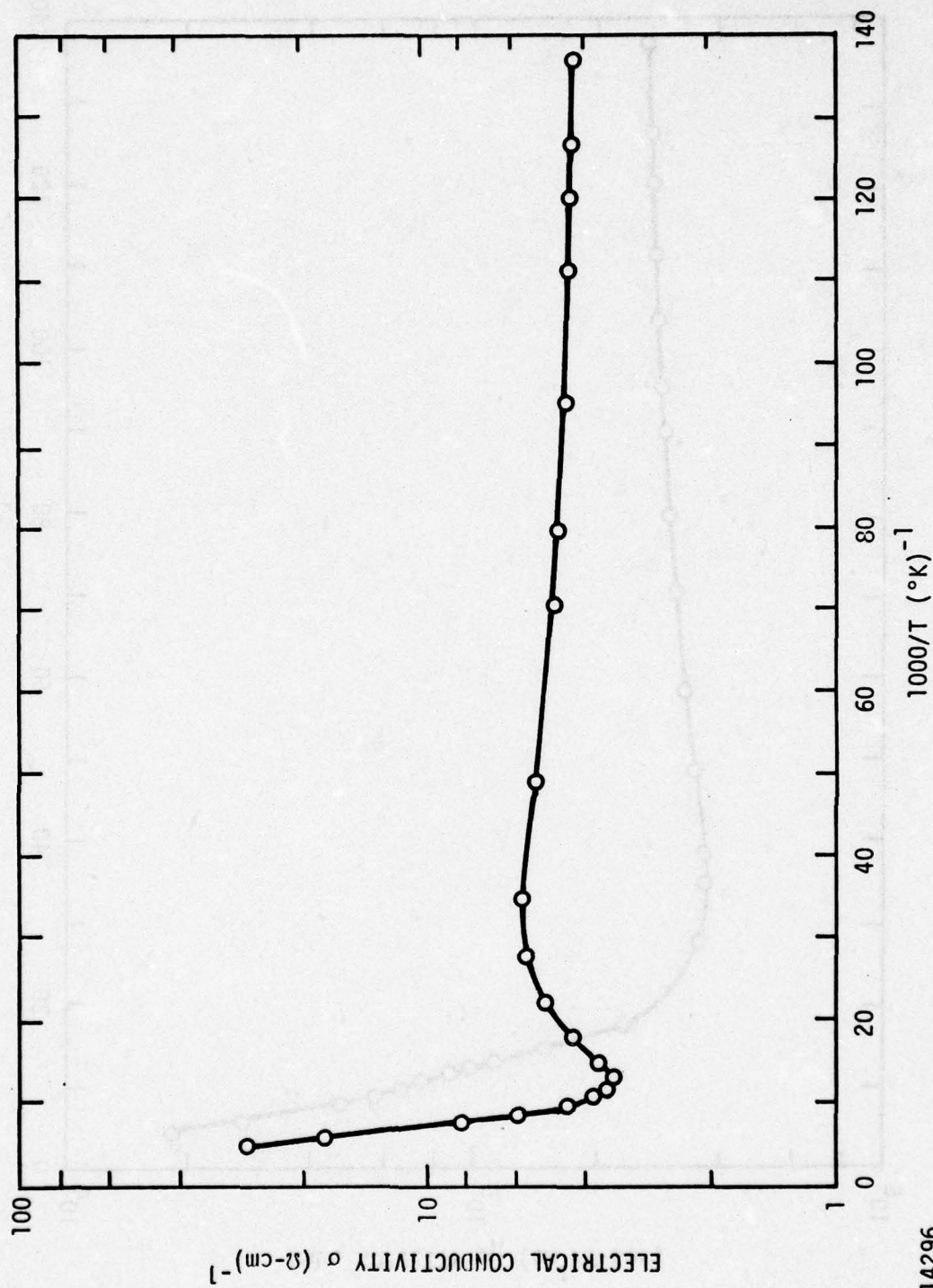
RT-14294

58

Figure 5-3. Preirradiation temperature dependence of the Hall mobility. Sample I-1

RT-14295

59

Figure 5-4. Preirradiation temperature dependence of the electrical conductivity, Sample I-1

RT-14296

60

Steady-State Photoconductivity and Carrier Lifetime

The background photon flux Q_B (and also the signal photon flux Q_S for spectral response and steady-state photoconductivity measurements) was controlled by the aperture diameter in the cold radiation shield (see Figure 3.3). An aperture diameter of 0.10 inch was chosen for measurements during irradiation and anneal, since smaller aperture diameters gave marginal spectral response signals. This aperture diameter resulted in a 300°K background Q_B of 3.6×10^{14} photons/cm^2·sec. It should be pointed out that the chopped 1000°K blackbody signal photon flux, Q_S, for this aperture size and the geometry used was ~2.5×10^{16} photons/cm^2·sec, which is considerably larger than the ambient 300°K background flux. Before irradiation, the carrier lifetime was measured from the decay of excess carriers produced by a pulsed GaAs LED at several background levels. The decay lifetimes were measured from about 8 to 25°K and exhibited at least two decay time constants, as shown in Table 5-1. At the highest background level ($Q_B = 2.5 \times 10^{16}$), the two components at 10°K were ~0.24 and 1.23 µsec. As the temperature is increased, the two decay times remain nearly constant; however, the relative effect of the two components on photoconductive response changes as shown in the last column of Table 5-1. At 8.2°K, 30% of the total response results from the shorter lifetime component and 70% results from the longer component. At 21.4°K, the shorter component controls ~70% of the response and results in a smaller photoconductive response even though the magnitudes of the decay times are relatively unchanged. A semi-log plot of the photoconductive decay versus time for these temperatures is given in Figure 5.5 and illustrates the relative weight of the two decay constants. The change in the relative weight of the two time constants with temperature makes it impractical to assign an effective temperature-dependent lifetime since the effective lifetime is neither the sum of the two components nor the sum of the reciprocal decay times. At lower background ($Q_B = 3.6 \times 10^{14}$, 4.5×10^{13}, $<1.5 \times 10^{13}$), both the short and longer lifetime components are increased and the longer component exhibits stronger temperature dependence (Table 5-1). Also, the increasing dependence of

61

Table 5-1

PREIRRADIATION CARRIER LIFETIME AT DIFFERENT BACKGROUND LEVELS

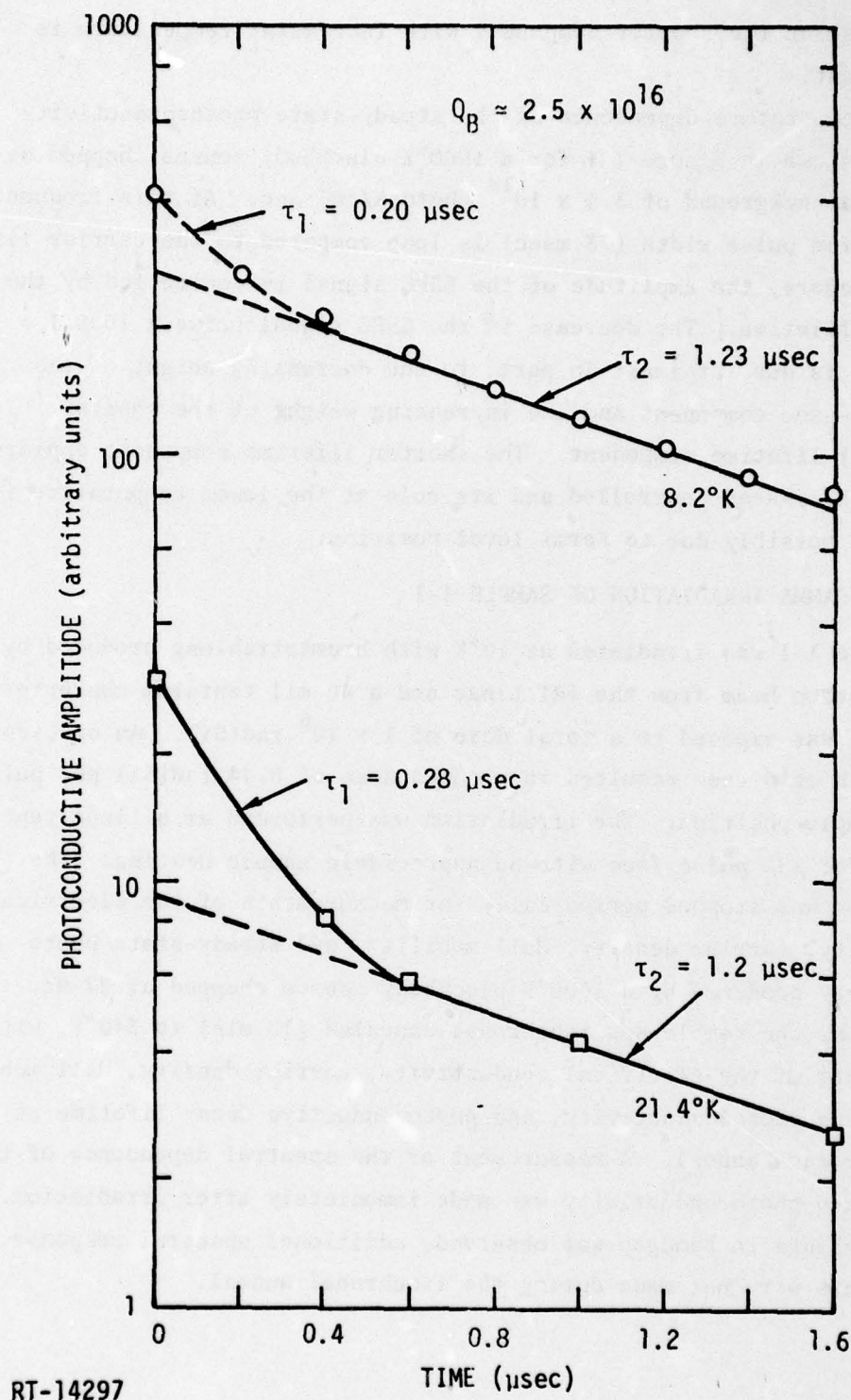| Temp (°K)	τ_1 (μsec)	τ_2 (μsec)	Percent of total response due to τ_1
$Q_B = 2.5 \times 10^{16}$			
8	0.20	1.23	30
8.7	0.20	1.23	35
9.5	0.24	1.23	40
11.1	0.24	1.20	49
13.2	0.16	1.20	50
14.5	0.20	1.20	71
21.4	0.28	1.20	71
$Q_B = 3.6 \times 10^{14}$			
10	0.3	2.8	28
$Q_B = 4.5 \times 10^{13}$			
5.9	0.61	7.5	52
7.6	0.61	7.5	56
9.3	0.56	6.4	60
10.5	0.52	5.9	64
14.5	0.40	4.6	80
$Q_B \ll 1.5 \times 10^{13}$			
5.1	0.78	14.0	38
5.7	0.65	13.0	40
10	~1.0	7.6	48

RT-14297

Figure 5-5. Comparison of photoconductive decay at 8.2 and 21.4°K after a GaAs LED pulsed injection. Sample I-1, preirradiation

63

the response on the shorter component with increasing temperature is still present.

The temperature dependence of the steady-state photoconductivity (SSPC) is shown in Figure 5-6 for a 1000°K blackbody source chopped at 22 Hz and a background of 3.6×10^{14} photons/cm^2·sec. At this frequency, the injection pulse width (23 msec) is long compared to the carrier life-time; therefore, the amplitude of the SSPC signal is controlled by the effective lifetime. The decrease in the SSPC signal between 1000/T = 100 and 50 is due, at least in part, to the decreasing weight of the longer 2.8-μsec component and the increasing weight of the shorter (∿0.3-μsec) lifetime component. The shorter lifetime component appears to be Shockley-Read controlled and its role at the lower temperature is diminished possibly due to Fermi level position.

5.1 10°K GAMMA IRRADIATION OF SAMPLE I-1

Sample I-1 was irradiated at 10°K with bremsstrahlung produced by a 5-MeV electron beam from the IRT Linac and a 40-mil tantalum converter. The sample was exposed to a total dose of 1×10^6 rad(Si). An electron pulse width of 6 μsec resulted in a gamma dose of 0.44 rad(Si) per pulse at the sample position. The irradiation was performed at a Linac repetition rate of 180 pulses/sec with no appreciable sample heating. The irradiation was stopped periodically for measurements of the electrical conductivity, carrier density, Hall mobility, and steady-state photo-conductivity produced by a 1000°K blackbody source chopped at 22 Hz. After irradiation, the sample was isochronal-annealed (10 min) to 340°K, with measurements of the electrical conductivity, carrier density, Hall mobility, steady-state photoconductivity, and photoconductive decay lifetime at 10°K after each anneal. A measurement of the spectral dependence of the steady-state photoconductivity was made immediately after irradiation. Since no change in bandgap was observed, additional spectral response measurements were not made during the isochronal anneal.
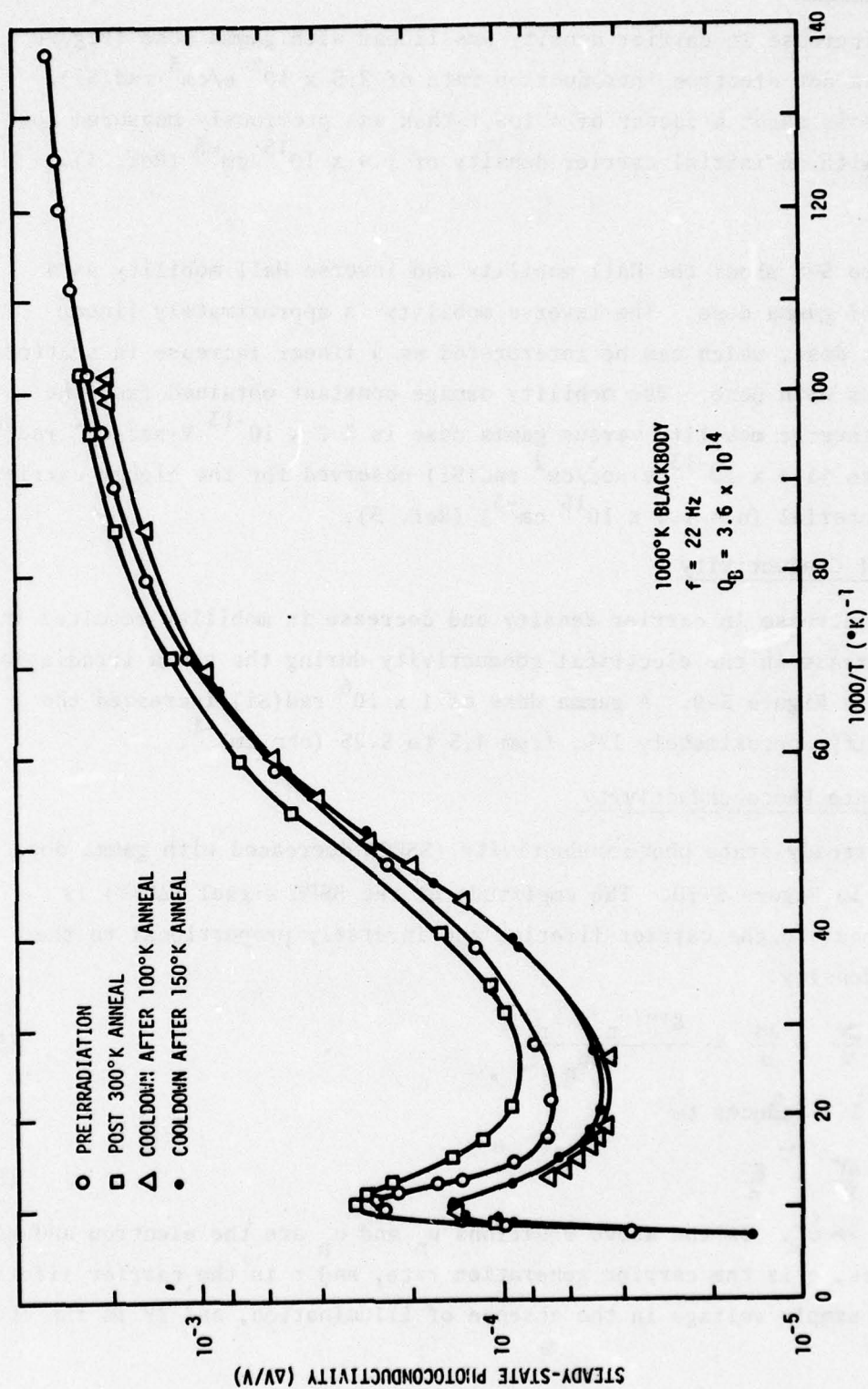
64

Figure 5-6. Steady-state photoconductivity temperature dependence before 10°K gamma irradiation and during cooldown after isochronal anneals. Sample I-1.

RT-14298

65

Carrier Density

The increase in carrier density was linear with gamma dose (Figure 5-7) with a net electron introduction rate of 2.5×10^7 e/cm^3·rad(Si). This value is about a factor of 4 lower than was previously measured for a sample with an initial carrier density of 1.4×10^{15} cm^{-3} (Ref. 3).

Mobility

Figure 5-8 shows the Hall mobility and inverse Hall mobility as a function of gamma dose. The inverse mobility is approximately linear with gamma dose, which can be interpreted as a linear increase in scattering centers with dose. The mobility damage constant obtained from the slope of inverse mobility versus gamma dose is 3.2×10^{-13} V·sec/cm^2 rad(Si) compared to $\sim 1.4 \times 10^{-13}$ V·sec/cm^2 rad(Si) observed for the higher-carrier-density material ($n \simeq 1.4 \times 10^{15}$ cm^{-3}) (Ref. 3).

Electrical Conductivity

The increase in carrier density and decrease in mobility resulted in a net increase in the electrical conductivity during the gamma irradiation as shown in Figure 5-9. A gamma dose of 1×10^6 rad(Si) increased the conductivity approximately 17%, from 4.5 to 5.25 (ohm-cm)$^{-1}$.

Steady-State Photoconductivity

The steady-state photoconductivity (SSPC) decreased with gamma dose as shown in Figure 5-10. The amplitude of the SSPC signal ($\Delta V/V$) is proportional to the carrier lifetime and inversely proportional to the carrier density.

$$\frac{\Delta V}{V} = \frac{\Delta \sigma}{\sigma} = \frac{g\tau e(\mu_n + \mu_p)}{ne\mu_n} \tag{5.1}$$

Equation 5.1 reduces to

$$\frac{\Delta V}{V} = \frac{g\tau}{n} \tag{5.2}$$

since $\mu_n \gg \mu_p$. In the above equations μ_n and μ_p are the electron and hole mobilities, g is the carrier generation rate, and τ is the carrier lifetime. V is the sample voltage in the absence of illumination, and ΔV is the change
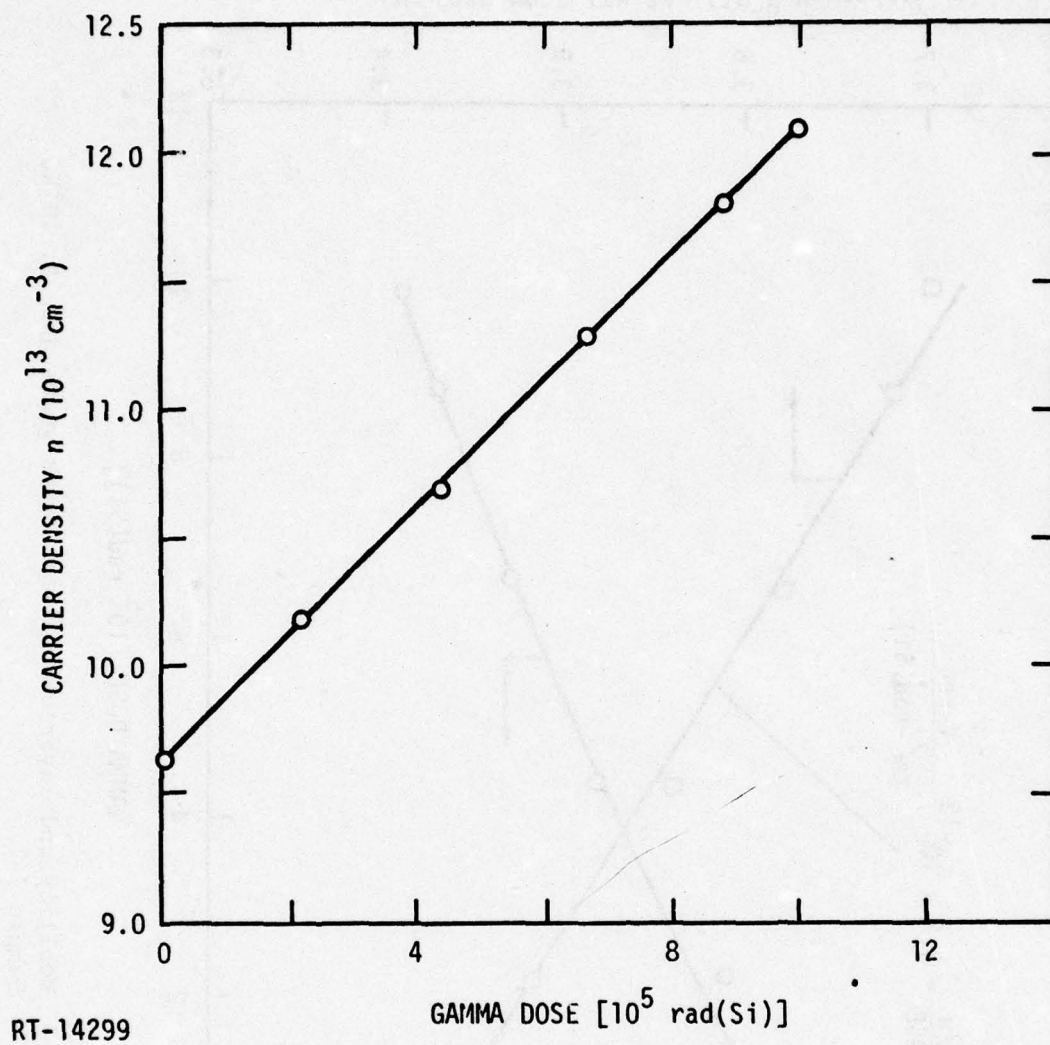
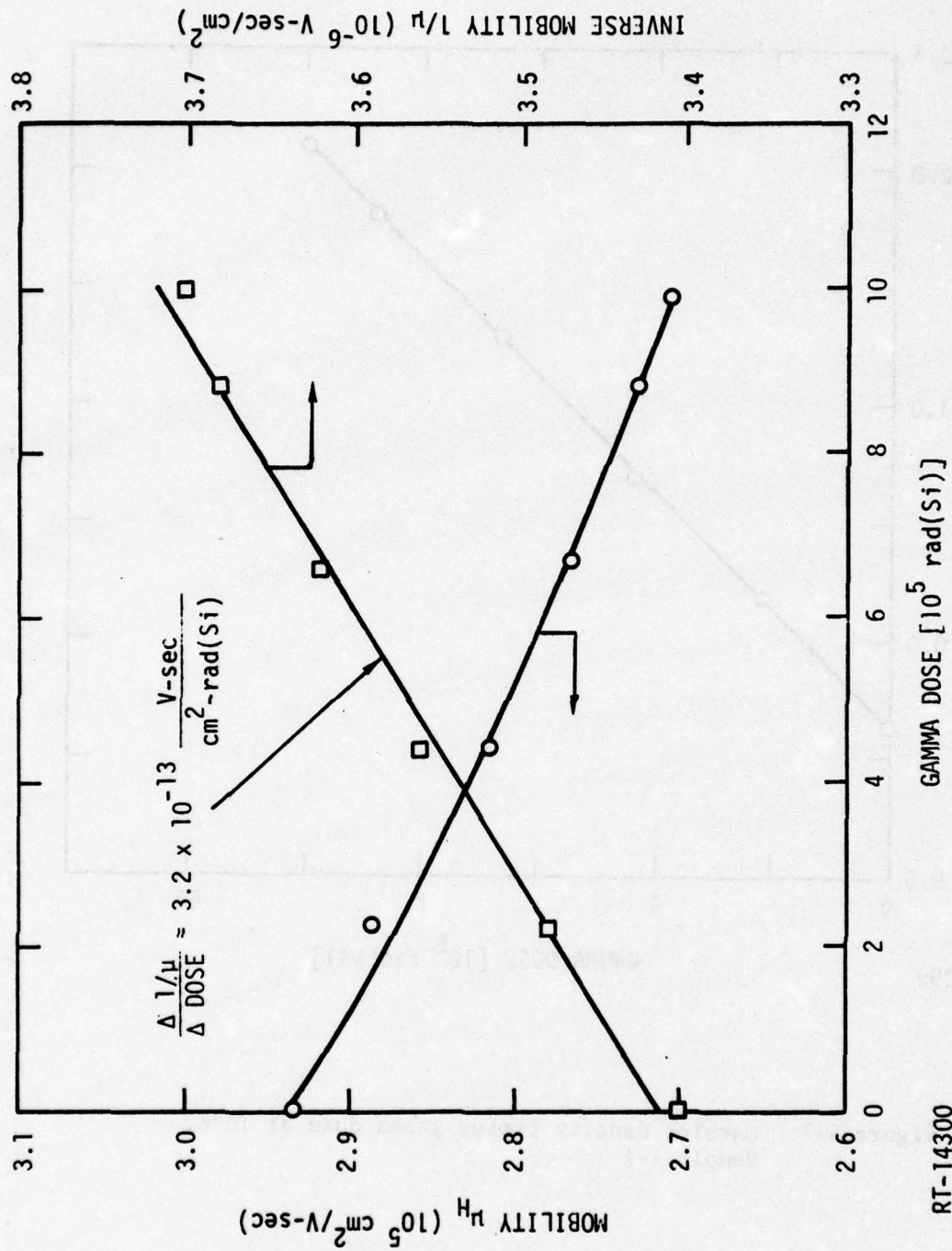Figure 5-7   Carrier density versus gamma dose at 10°K, Sample I-1

RT-14299

INVERSE MOBILITY $1/\mu$ (10^{-6} V-sec/cm^2)

3.8   3.7   3.6   3.5   3.4   3.3

GAMMA DOSE [10^5 rad(Si)]

$$\frac{\Delta\,1/\mu}{\Delta\,\text{DOSE}} = 3.2 \times 10^{-13} \; \frac{\text{V-sec}}{\text{cm}^2\text{-rad(Si)}}$$

MOBILITY μ_H (10^5 cm^2/V-sec)

3.1   3.0   2.9   2.8   2.7   2.6

RT-14300

Figure 5-8 Mobility and inverse mobility versus gamma dose at 10°K, Sample I-1
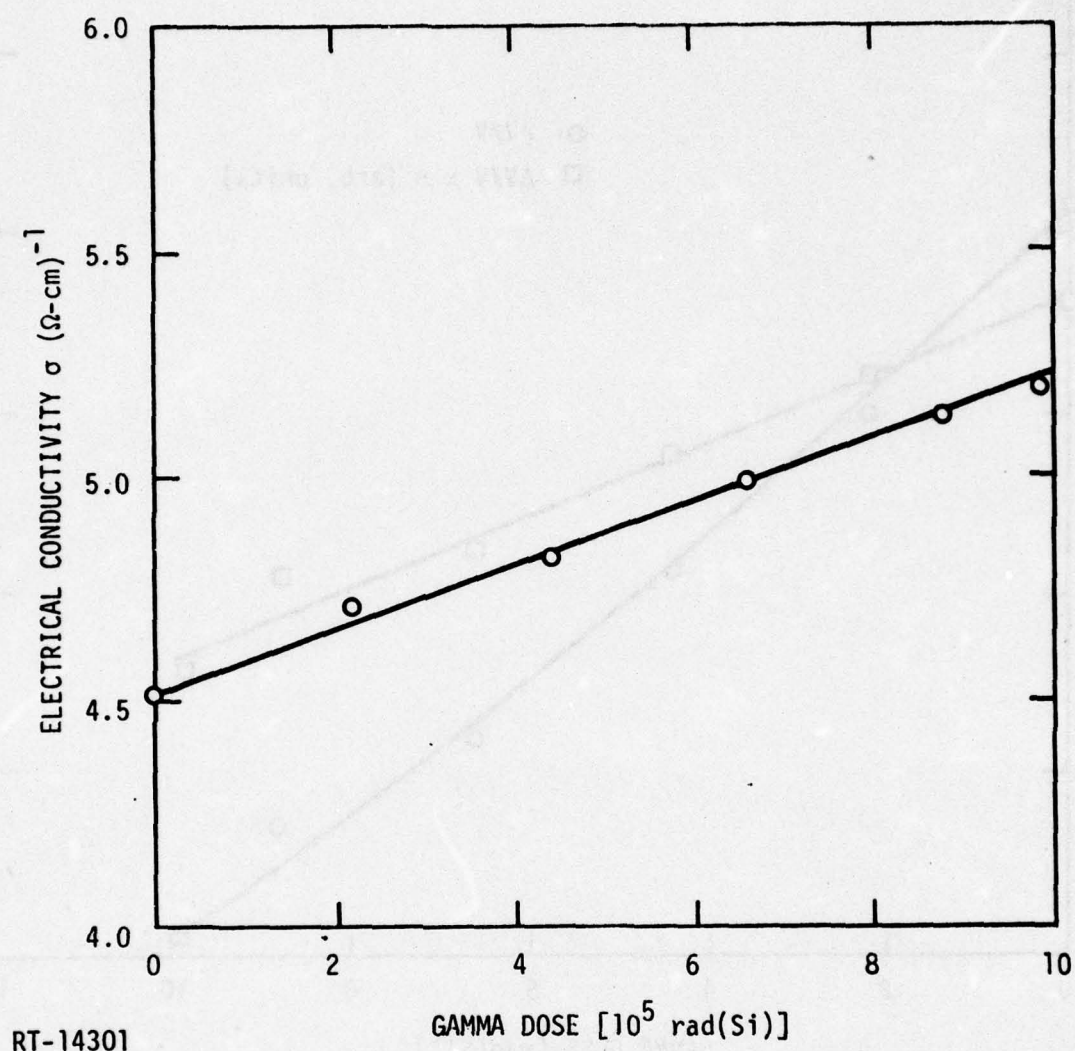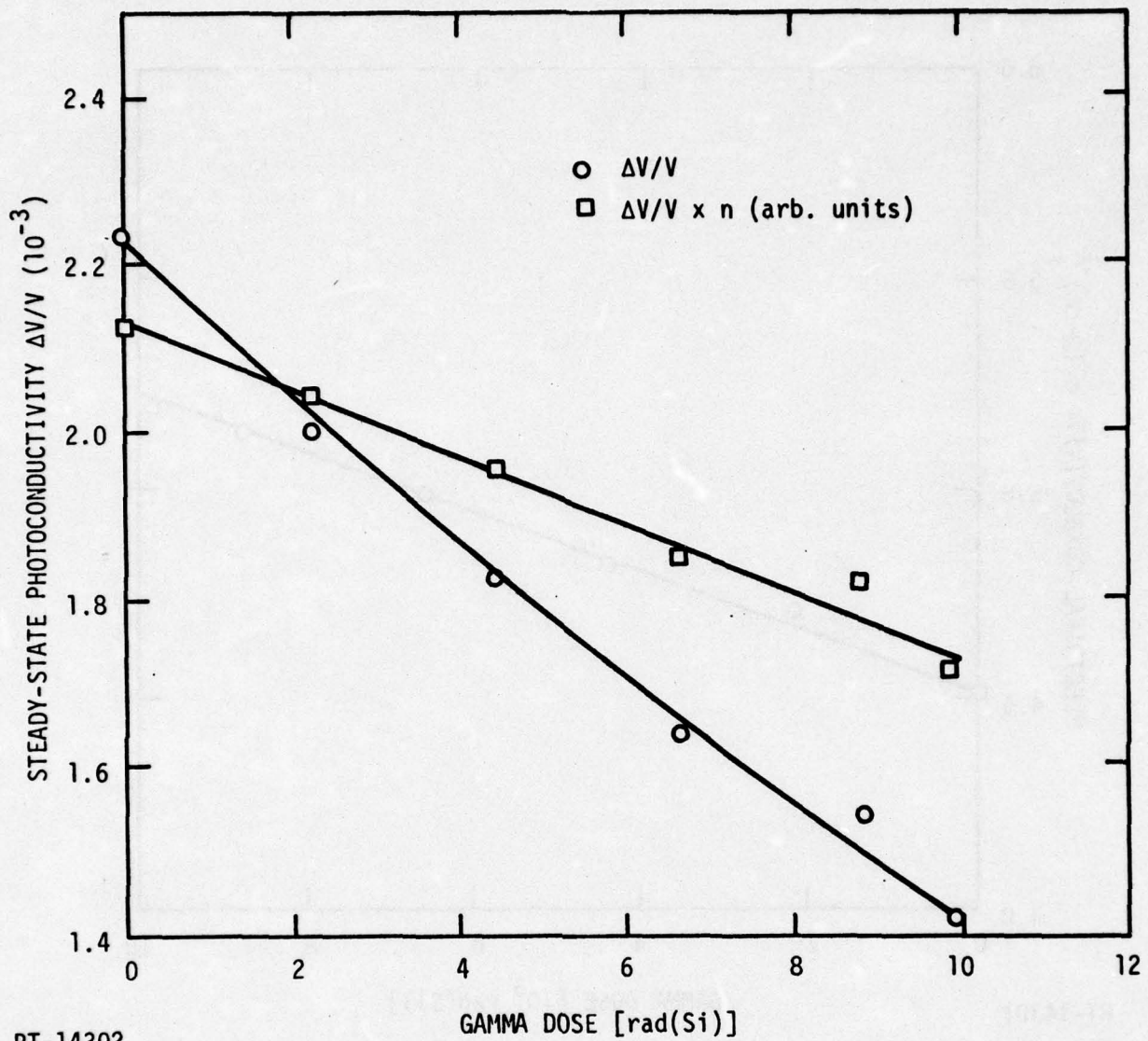
68

RT-14301

Figure 5-9   Electrical conductivity versus gamma dose
              at 10°K, Sample I-1

69

RT-14302

Figure 5-10   Steady state photoconductivity versus gamma
dose at 10°K, Sample I-1

70

in V produced by illumination ($\Delta V \ll V$). Equation 5.2 indicates that if $\Delta V/V$ is multiplied by the increasing carrier density during the irradiation, the product should be proportional to the carrier lifetime τ. This product is also shown in Figure 5-10 and indicates approximately a 20% decrease in lifetime for a gamma dose of 1×10^6 rad(Si). After irradiation and prior to any anneal, however, the lifetime measured by photoconductive decay was the same as the preirradiation lifetime, at least within the accuracy of decay lifetime measurements. A possible explanation for the apparent decrease in lifetime indicated from SSPC is the relative weight of the two lifetime components on the response before and after irradiation. Before irradiation, the short component (~ 0.3 μsec) was responsible for about 28% of the total response compared to about 38% after irradiation and prior to anneal. A value of ~ 2.8 μsec was measured for the longer component before irradiation, compared to ~ 2.7 μsec after irradiation. From the above, it appears that the gamma irradiation of 1×10^6 rad(Si) produced no significant lifetime damage and that the decrease in SSPC was produced by the increased carrier density and possibly a change in the relative weight of the two lifetime components.

Isochronal Anneal

Isochronal anneal of the carrier density, Hall mobility, electrical conductivity, and SSPC is shown in Figures 5-11 through 5-14. The anneals were of 10-min duration, with measurements made at 10°K after anneals at the temperatures indicated by the data points. All of these parameters recovered to near their preirradiation values, with the major annealing stage occurring between 50 and 75°K. The SSPC, however, exhibits an additional gradual recovery between 150 and 275°K. After the 275°K anneal, the SSPC signal exceeds the preirradiation value and then decreases and approaches the preirradiation value after the 330°K anneal.

Figure 5-15 compares the carrier lifetime measured by photoconductive decay and calculated from SSPC data during the anneal. The peak observed in the calculated lifetime after the 275°K anneal (and also $\Delta V/V$, Figure 5-14) appears to result from the relative weight of the two lifetime components on the photoconductive response. After the 275°K anneal, the shorter component controls about 32% of the response, compared with 52% after the
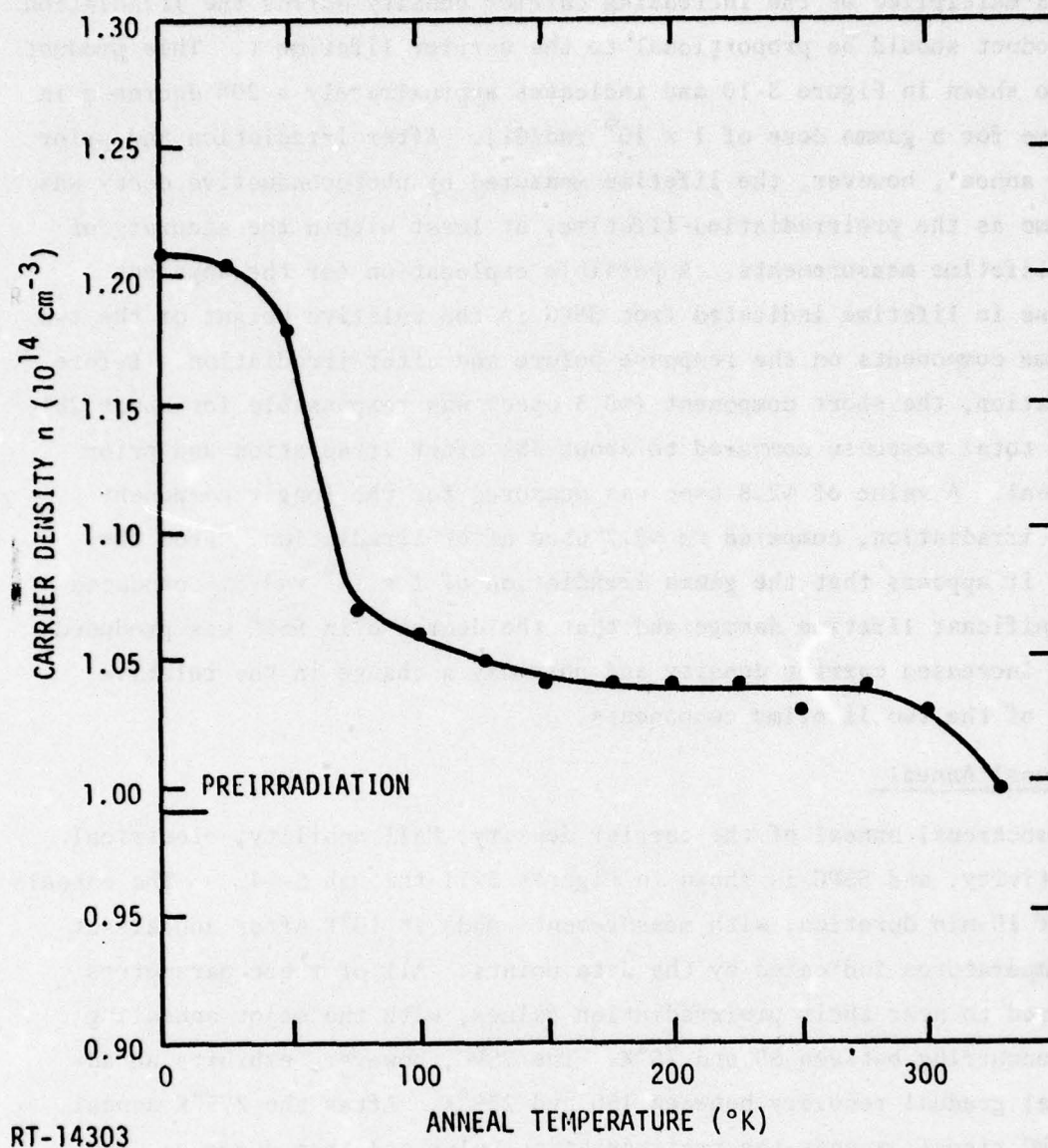
71

RT-14303

Figure 5-11   Isochronal anneal (10 min) of carrier density
after 10°K gamma irradiation: measurement at
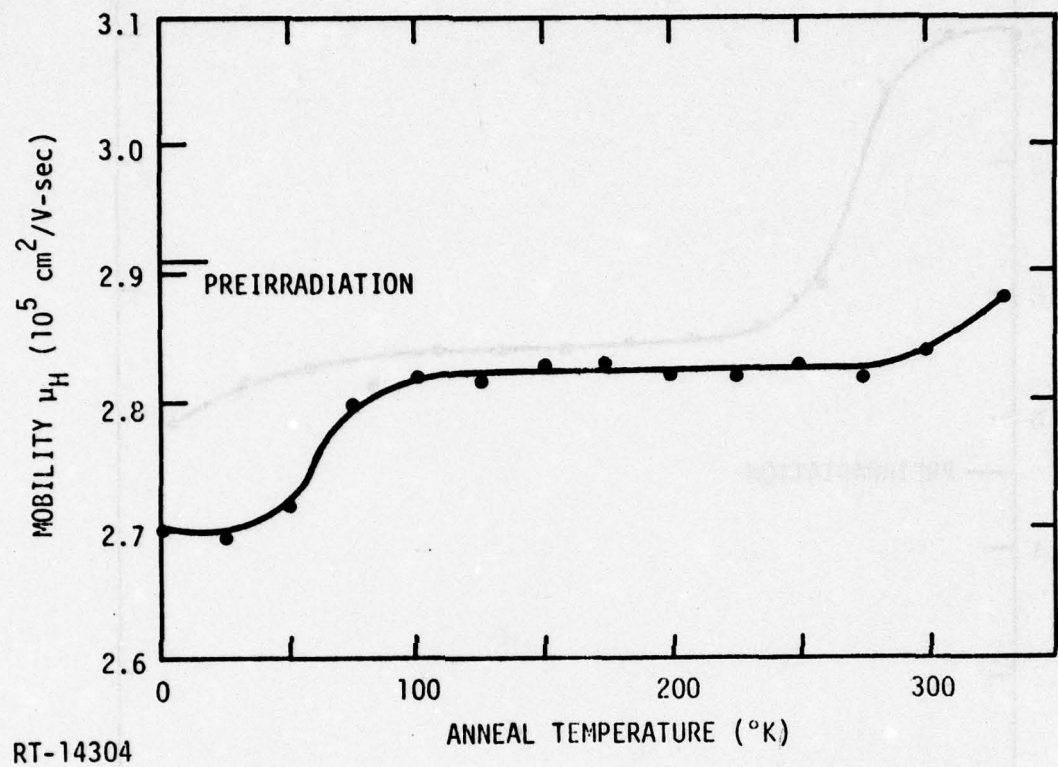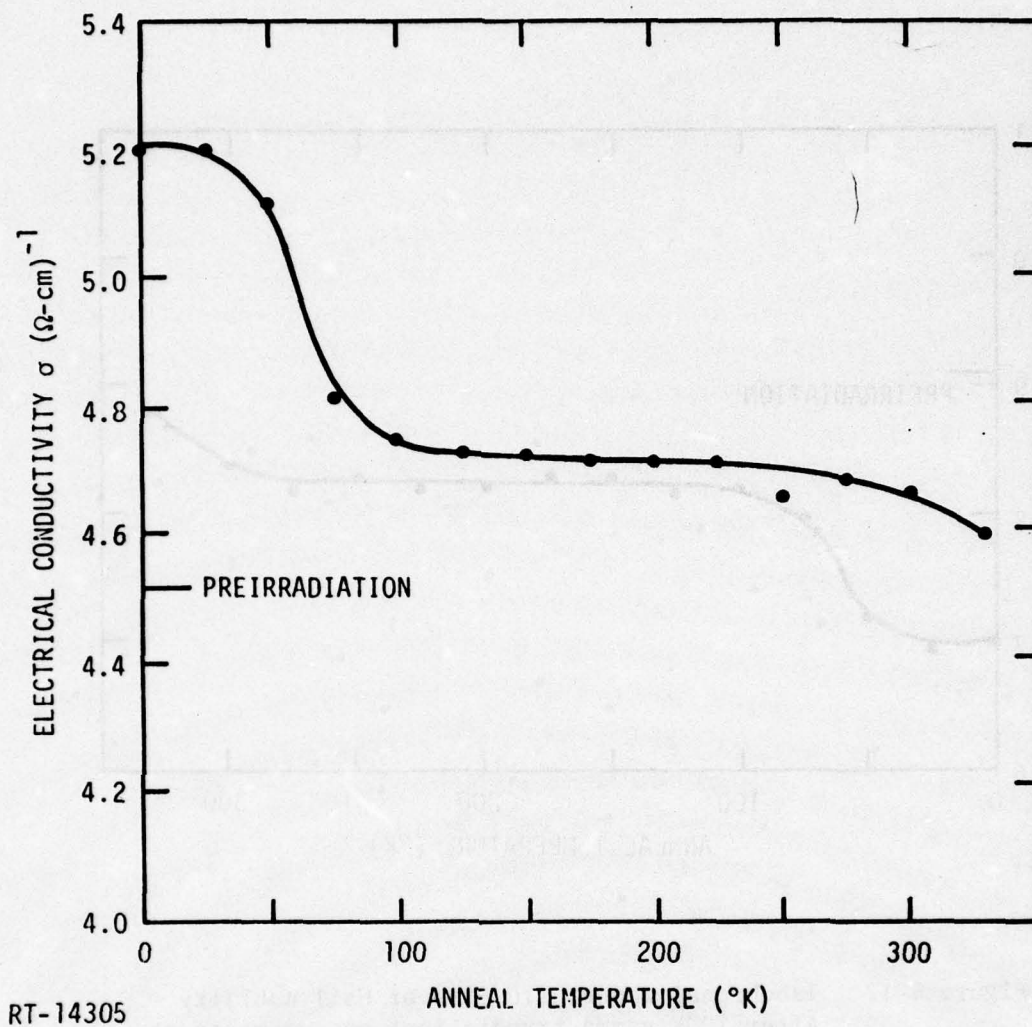10°K after each anneal, Sample I-1

72

Figure 5-12   Isochronal anneal (10 min) of Hall mobility
after 10°K gamma irradiation; measurements at
10°K after each anneal, Sample I-1

73

RT-14305

Figure 5-13   Isochronal anneal (10 min) of electrical
conductivity after 10°K gamma irradiation;
measurements at 10°K after each anneal,
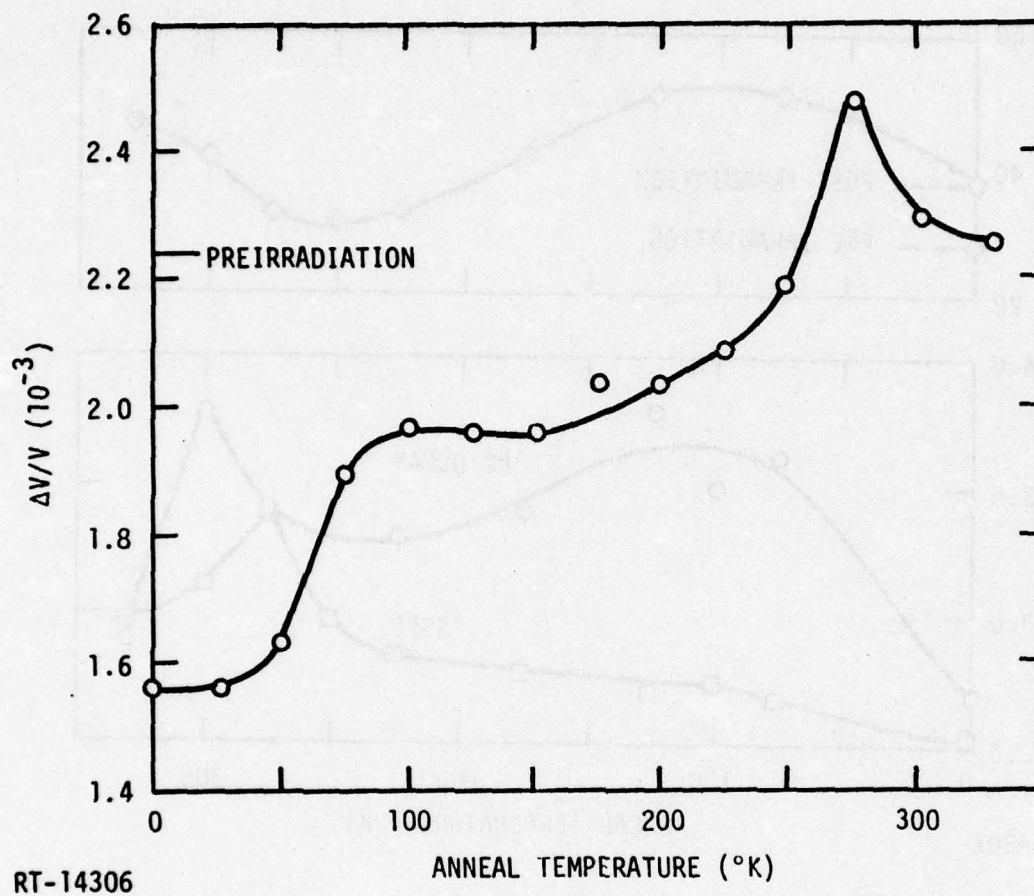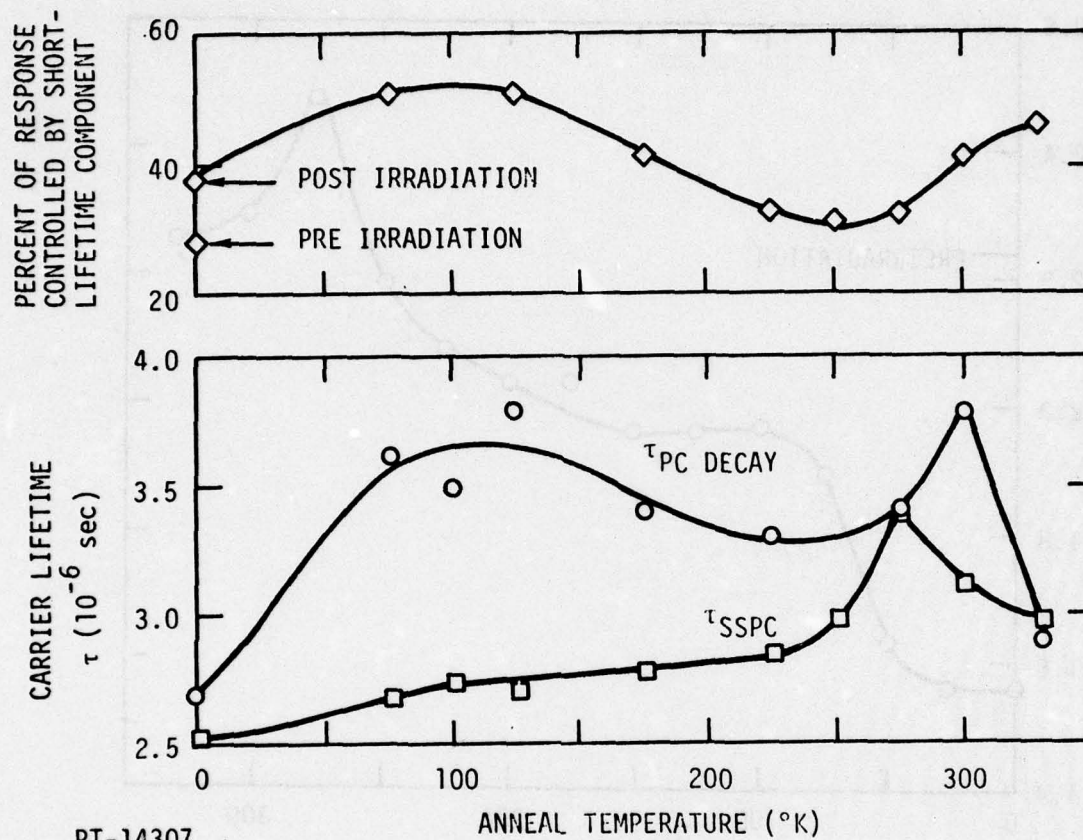Sample I-1

74

RT-14306

Figure 5-14   Isochronal anneal (10 min) of steady-state
photoconductivity after 10°K gamma irradiation;
measurements at 10°K after each anneal, Sample I-1

75

Figure 5-15   Lifetime (SSPC and PC decay) during isochronal
anneal, Sample I-1

76

125°K anneal (top curve of Figure 5-15). This is shown in Figure 5-16, which compares the photoconductive decay curves after the 125 and 275°K anneal. The amplitude of the long time constant is obtained by an extrapolation of the decay curve to zero time. The amplitude of the short time constant is then obtained by subtracting this value from the total observed response. As can be seen in Figure 5-16, the short time constant of 0.5 μsec was less effective in controlling the total response after the 275°K anneal than after the 125°K anneal.

Spectral Response

The spectral response was measured prior to irradiation and immediately following the irradiation, before any anneal. These results are shown in Figure 5-17. No shift in cutoff wavelength (bandgap) was observed; therefore, spectral response measurements were not made during the isochronal anneal.

Post Irradiation SSPC Temperature Dependence

The temperature dependence of the carrier density, Hall mobility, and electrical conductivity after anneal was nearly identical to the pre-irradiation value and is not shown. The SSPC, however, exhibited significant differences; therefore, the SSPC during cooldown after several anneals is compared with preirradiation data in Figure 5-6. It is interesting to note that the SSPC indicates a considerably larger damage after the 100°K anneal for 1000/T between 10 and 20 than at lower temperatures. Shockley-Read recombination is thought to dominate at the higher temperature and becomes less effective at lower temperatures. Figure 5-6 indicates that Shockley-Read centers were produced by the gamma irradiation; however, these centers were relatively ineffective at the irradiation temperature of 10°K. After the 300°K anneal, the SSPC recovered to a value slightly greater than the preirradiation curve throughout the entire temperature range.

Decay of Excess Conductivity Produced by Pulsed Gamma Injection

During the gamma irradiation, it was possible to measure the time dependence of the decay of excess carriers produced by the 0.44 rad(Si) gamma pulse delivered in 6 μsec. Figure 5-18 is a photograph taken
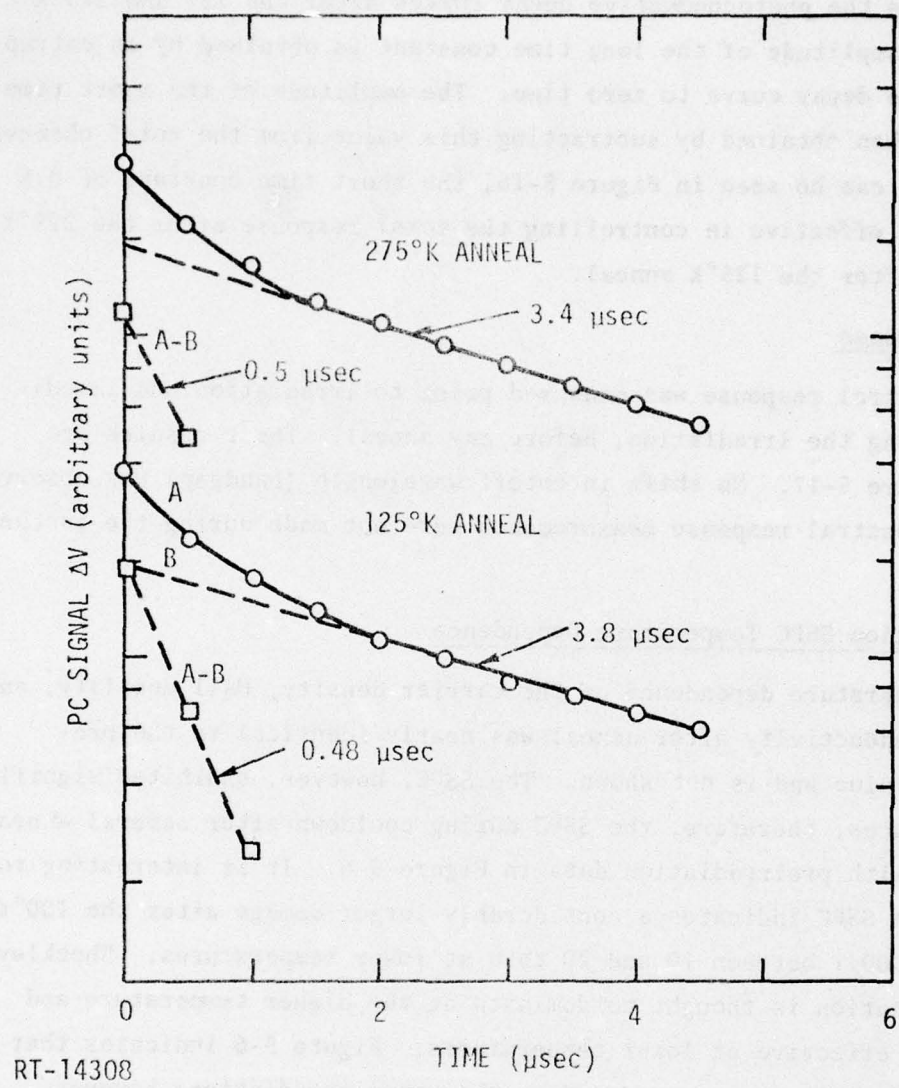
77

Figure 5-16.   Photoconductive decay curves after 125 and
275°K anneals, Sample I-1

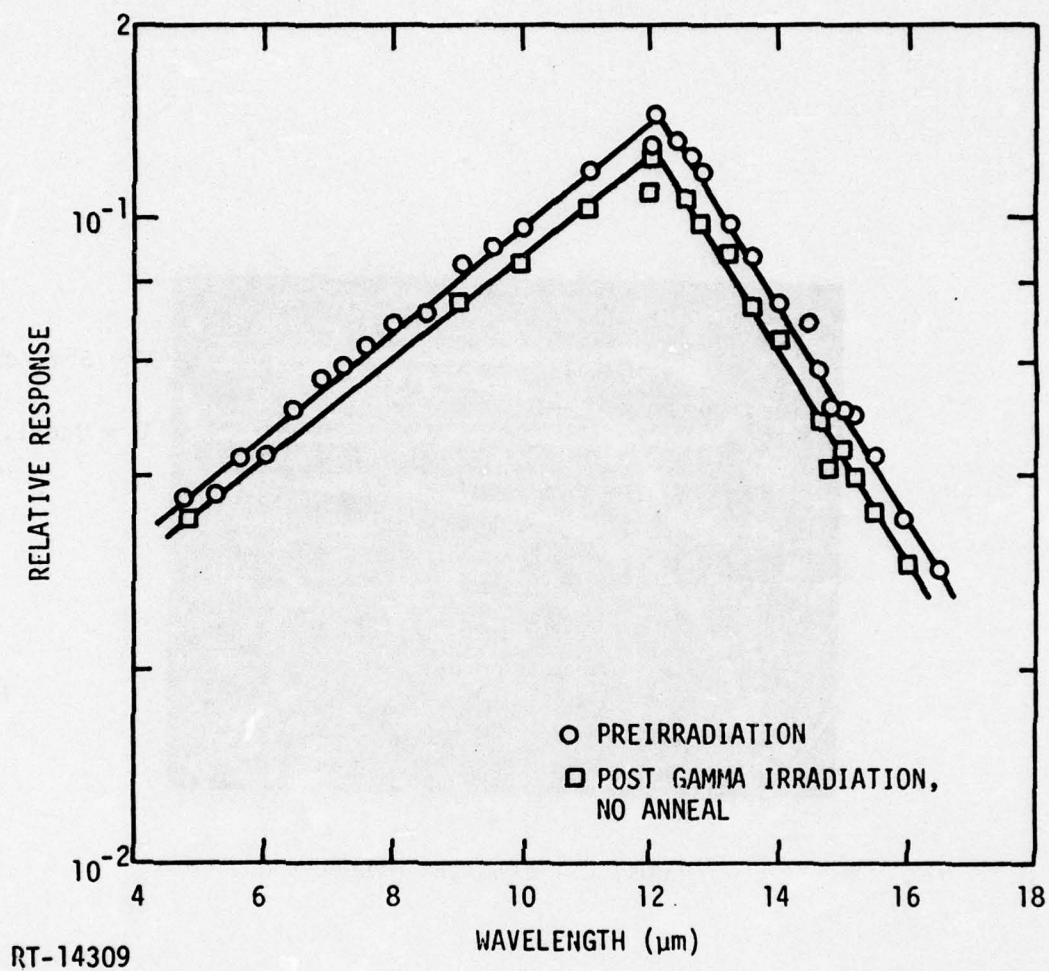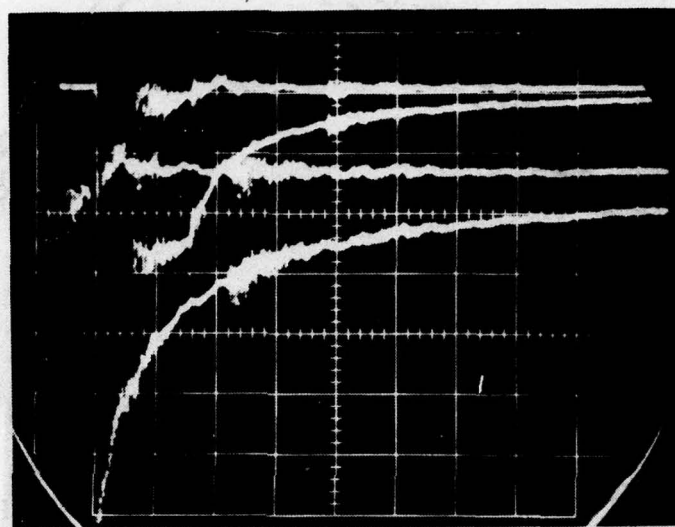RT-14308

RT-14309

Figure 5-17. Pre- and post-gamma irradiation 10°K spectral response, Sample I-1

79

V = 5 mV/cm

V = Uncal.

HORIZONTAL SCALE   5 μsec/cm

Figure 5-18.   Decay of excess conductivity produced by a
6 μsec wide, 0.44 rad(Si) gamma pulse.
Sample I-1, 10°K.

at the end of the gamma irradiation ($\sim$1 x 10^6 rad) at a sweep of 5 μsec/ division. The upper trace is 5 mV/cm, the lower trace is magnified and uncalibrated to show the decay curve. At the end of the 6 μsec gamma pulse the carrier density, determined from the upper trace, has increased to 2.9 x 10^{14} cm^{-3} or approximately 2.5 times the equilibrium carrier density of $\sim$1.2 x 10^{14} cm^{-3}. A relatively large injection ratio (Δn/n) of 10% still exists at the end of the trace. A decay time constant of $\sim$6 μsec was measured during the first 20 μsec of the decay. The time constant then increased to about 50 μsec for the remainder of the decay shown in Figure 5-18.

Both of these decay time constants are longer than the decay time constant ($\sim$3 μsec) following a pulse of illumination by the GaAs LED, which produced a much smaller average injection level (Δn/n) of only 10^{-4} to 10^{-3}. If the recombination process were only Auger, one would expect the decay times to be shorter for the large injection levels produced by the gamma pulse.

One possible reason for the shorter time constant with the GaAs LED is that the light from the LED is heavily absorbed near the surface of the sample whereas the gamma rays produce uniform bulk ionization. Since the estimated injection ratio of 10^{-4} to 10^{-3} for the LED is an average across the bulk of the sample, the injection ratio near the surface is actually much larger. The shorter recombination lifetime could result from surface recombination and/or Auger recombination in the high injection level region near the surface.

Another possible mechanism for the longer lifetimes at larger injection due to the gamma pulse is the injection level dependence of the lifetime, when the lifetime is controlled by Shockley-Read recombination. From the lifetime versus carrier density shown in Figure 6-2 (Curve A), it appears possible that a large carrier injection could cause either an increase or decrease in carrier lifetime, depending on the value of the carrier density. For large carrier density (n > 7 x 10^{14} cm^{-3}) an increase in carrier density resulting from a large injection would place the lifetime on the Auger curve where $\tau \propto \dfrac{1}{n^2}$. At lower carrier density; where the lifetime

81

is controlled by Shockley-Read recombination, the increased carrier density resulting from a large injection would not decrease the lifetime by Auger recombination; however, the lifetime could increase if the number of excess carriers exceeds the number of Shockley-Read recombination centers. While this number is not known, an estimate can be made from the results of silicon studies. The lifetime τ is given by

$$\tau = \frac{1}{n_R \sigma v}$$

where n_R is the number of recombination centers, σ is the capture cross section and v is the carrier thermal velocity. Using a value of 2×10^{-13} cm^2 for the capture cross section and a lifetime of 3 μsec results in a recombination center density of 4.5×10^{11}/cm^3. While this estimate is uncertain, the excess carrier density exceeded this number by about a factor of 400 after the gamma pulse and was still a factor of 20 larger at the end of the trace shown in Figure 5-18. However, for the above argument to be completely valid, the lifetime should be longer immediately following the pulse (at the largest injection ratio) and then decrease as $\Delta n/n$ approaches zero, rather than the observed shorter lifetime immediately following the pulse.

The above discussion may help to explain the long time constant observed in HgCdTe detectors due to gamma injection, which results in heavy localized injection.

5.2 10°K NEUTRON IRRADIATION OF SAMPLE I-1

After gamma irradiation and anneal to 340°K, sample I-1 was neutron-irradiated at 10°K to a neutron fluence of 1.2×10^{13} n/cm^2 > 10 keV. The neutron fluence was produced by γ-n reactions resulting from 55-MeV electrons from the IRT Linac impinging on a thick tungsten target. The target was 1 inch in diameter and 1-1/4 inch in length, which is several radiation lengths for the bremsstrahlung produced by stopping of the electron beam. The gamma dose at the sample was minimized by placing the sample at the side of the tungsten converter, 90° with respect to the electron beam, since the bremsstrahlung is strongly forward-directed at this electron

82

energy. The sample gamma dose was further reduced by placing a dif-
ferential neutron-gamma shield of 4 inches of depleted uranium between
the target and sample. This configuration resulted in a total gamma
dose of 5×10^4 rad(Si), which produced an n/γ ratio of ~ 0.3 assuming a
gamma energy of 1 MeV. The average gamma energy is likely to be between
1 and 10 MeV, which would increase the n/γ ratio accordingly.

An objective of the neutron irradiation was to measure damage in
HgCdTe in a pure neutron environment, i.e., to reduce the gamma dose to
a level such that the observed damage could be attributed only to the
neutron fluence. Based on the observed carrier introduction, it appears
that this objective was adequately fulfilled. The measured carrier
introduction during the neutron irradiation was $\sim 3 \times 10^{13}$ cm^{-3}, compared
to a calculated value of 1.3×10^{12} cm^{-3} using the measured gamma dose
of 5×10^4 rad(Si) and the measured gamma carrier introduction rate
[2.5×10^7 carriers/cm$^3 \cdot$rad(Si)] shown in the previous section. In other
words, approximately 95% of the carriers introduced during the neutron
irradiation can be attributed to the neutron fluence.

Carrier Introduction

The carrier density as a function of neutron fluence is shown in
Figure 5-19. This curve is slightly nonlinear during the early part
of the irradiation; however, the average introduction rate ($\Delta n/\Delta\phi$) is
2.5 electrons per n/cm^2. This value is in good agreement with the value
of 2.8 obtained during a 10°K neutron irradiation of a sample with an
initial carrier density of $\sim 1.4 \times 10^{15}$ cm^{-3} (Ref. 4), which required a
large correction for an accompanying gamma dose.

Mobility Damage

The Hall mobility neutron fluence dependence is shown in Figure 5-20.
The inverse mobility, also shown in Figure 5-20, was linear with fluence
and exhibits a damage constant ($\Delta\frac{1}{\mu}/\Delta\Phi$) of

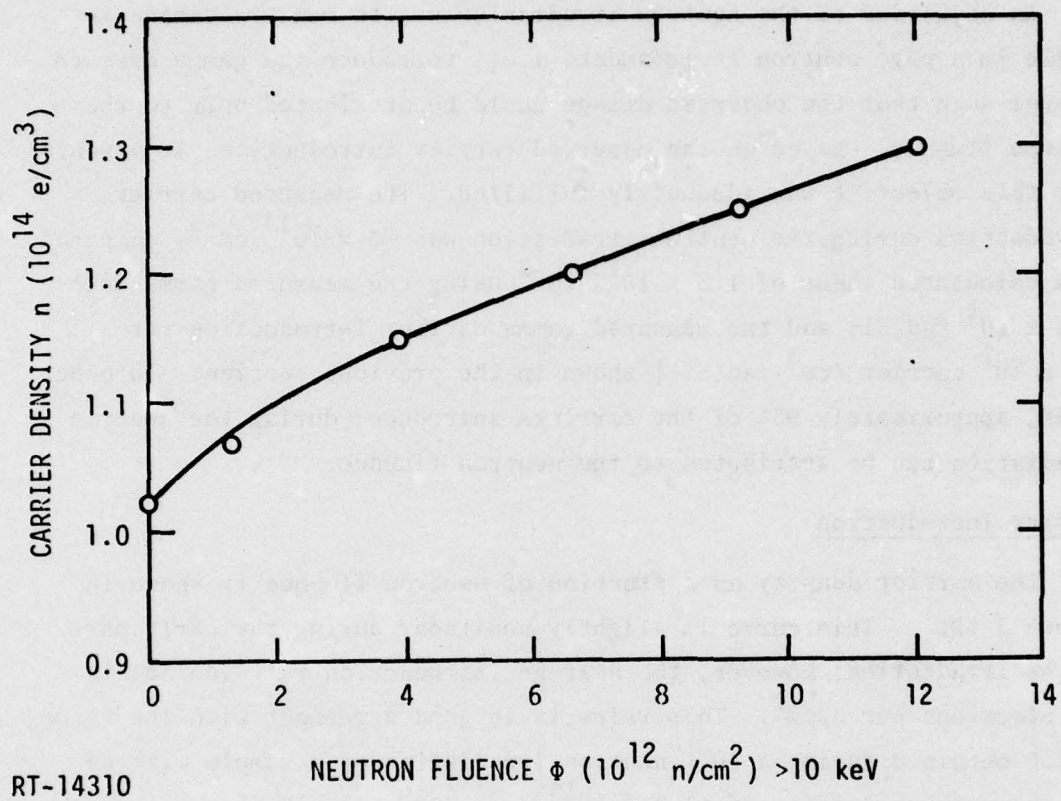$$6.9 \times 10^{-20} \left(\frac{V \cdot sec}{cm^2} \right) \left(\frac{cm^2}{n} \right) .$$

83

RT-14310

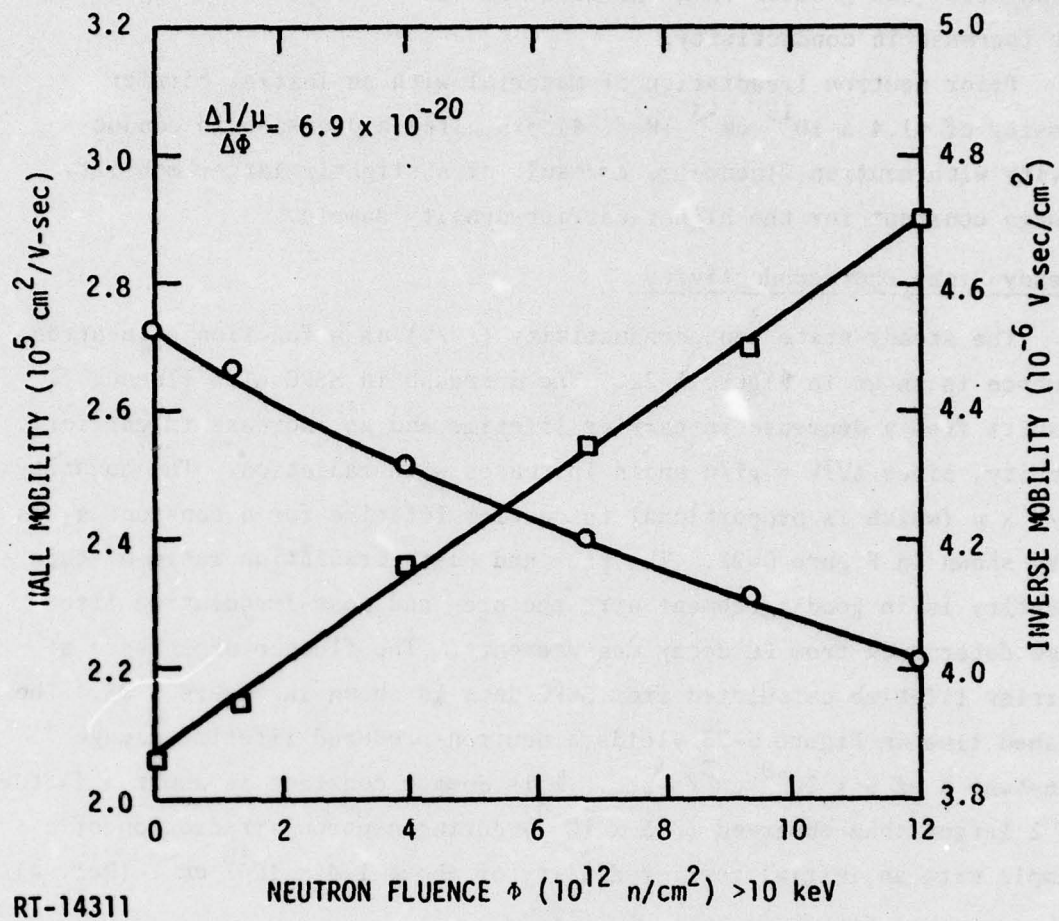Figure 5-19. Carrier density versus neutron fluence
at 10°K, Sample I-1

Figure 5-20. Hall mobility versus neutron fluence
at 10°K, Sample I-1

85

Electrical Conductivity

The electrical conductivity showed a slight increase with neutron fluence (Figure 5-21); i.e., the carrier introduction rate during the irradiation was greater than the decrease in mobility, resulting in a net increase in conductivity.

Prior neutron irradiation of material with an initial carrier density of $\sim 1.4 \times 10^{15}$ cm^{-3} (Ref. 4) exhibited a decrease in conductivity with neutron fluence as a result of a slightly larger mobility damage constant for the higher-carrier-density sample.

Steady-State Photoconductivity

The steady-state photoconductivity ($\Delta V/V$) as a function of neutron fluence is shown in Figure 5-22. The decrease in SSPC with fluence results from a decrease in carrier lifetime and an increase in carrier density, since $\Delta V/V = g\tau/n$ and n increases with radiation. The quantity $\Delta V/V \times n$ (which is proportional to carrier lifetime for a constant g) is also shown in Figure 5-22. The pre- and post-irradiation ratio of this quantity is in good agreement with the pre- and post-irradiation lifetime determined from PC decay measurements. The fluence dependence of carrier lifetime calculated from SSPC data is shown in Figure 5-23. The dashed line in Figure 5-23 yields a neutron-produced lifetime damage constant K of 9×10^{-9} cm^2/n-sec. This damage constant is about a factor of 2 larger than observed (3.5×10^{-9}) during neutron irradiation of a sample with an initial carrier density of about 1.4×10^{15} cm^{-3} (Ref. 4).

Isochronal Anneal of Neutron Damage

Isochronal anneal of the carrier density, Hall mobility, electrical conductivity, and SSPC is shown in Figure 5-24. Unlike electron and gamma damage, the anneal of neutron damage is more complex and recovery to the preirradiation conditions is less complete. The most significant changes in these parameters occurred between the 50 and 175°K anneals.

In this temperature range, the carrier density and mobility recover toward the preirradiation values. The SSPC shows a recovery between 50 and 100°K, then decreases between the 100 and 175°K anneals. The initial

86

RT-14313

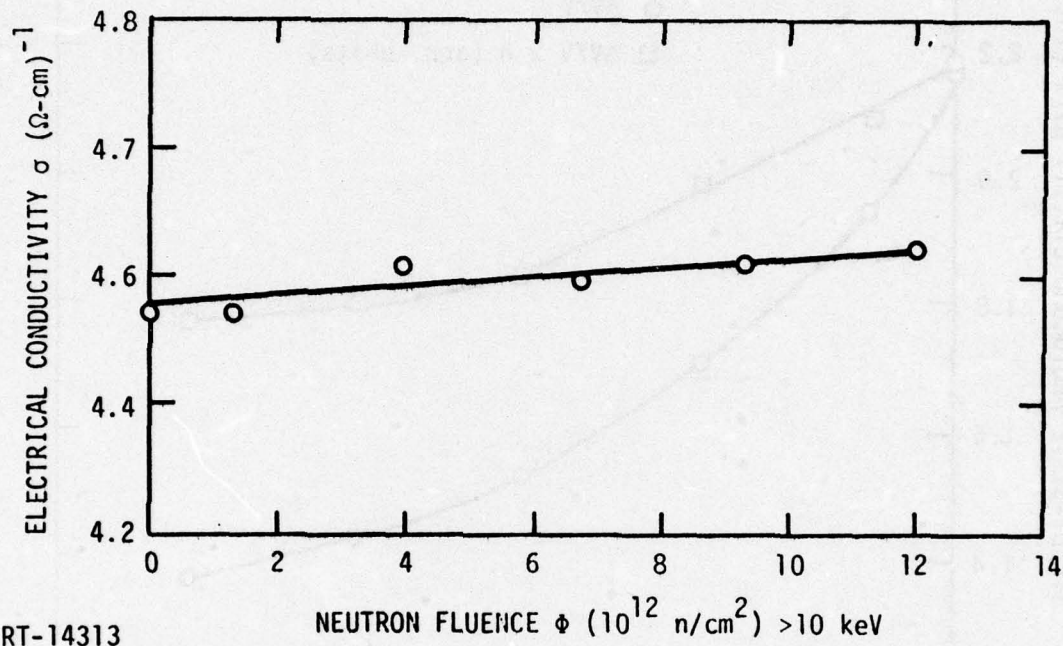Figure 5-21   Electrical conductivity versus neutron
fluence at 10°K, Sample I-1

87

STEADY-STATE PHOTOCONDUCTIVITY $\Delta V/V$ (10^{-3})

$\bigcirc$ $\Delta V/V$

$\square$ $\Delta V/V$ x η (arb. units)

NEUTRON FLUENCE Φ $(10^{12}\ n/cm^2)$ >10 keV
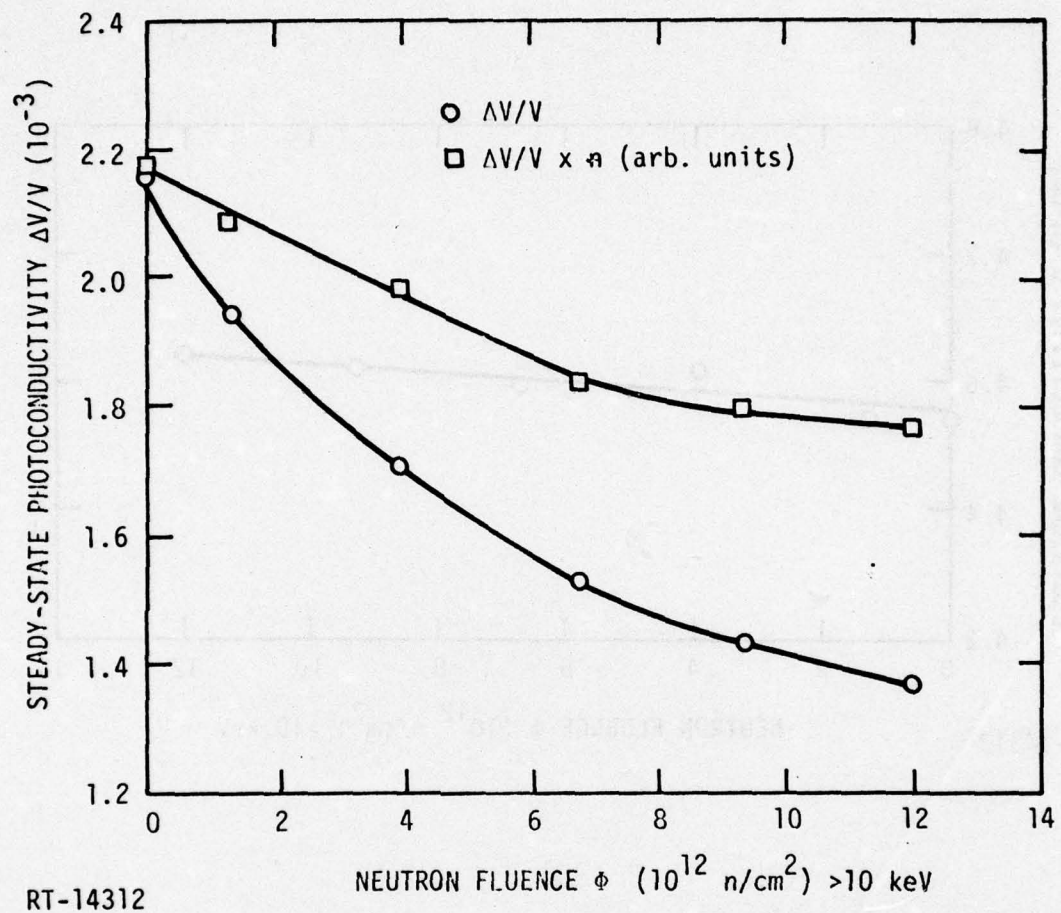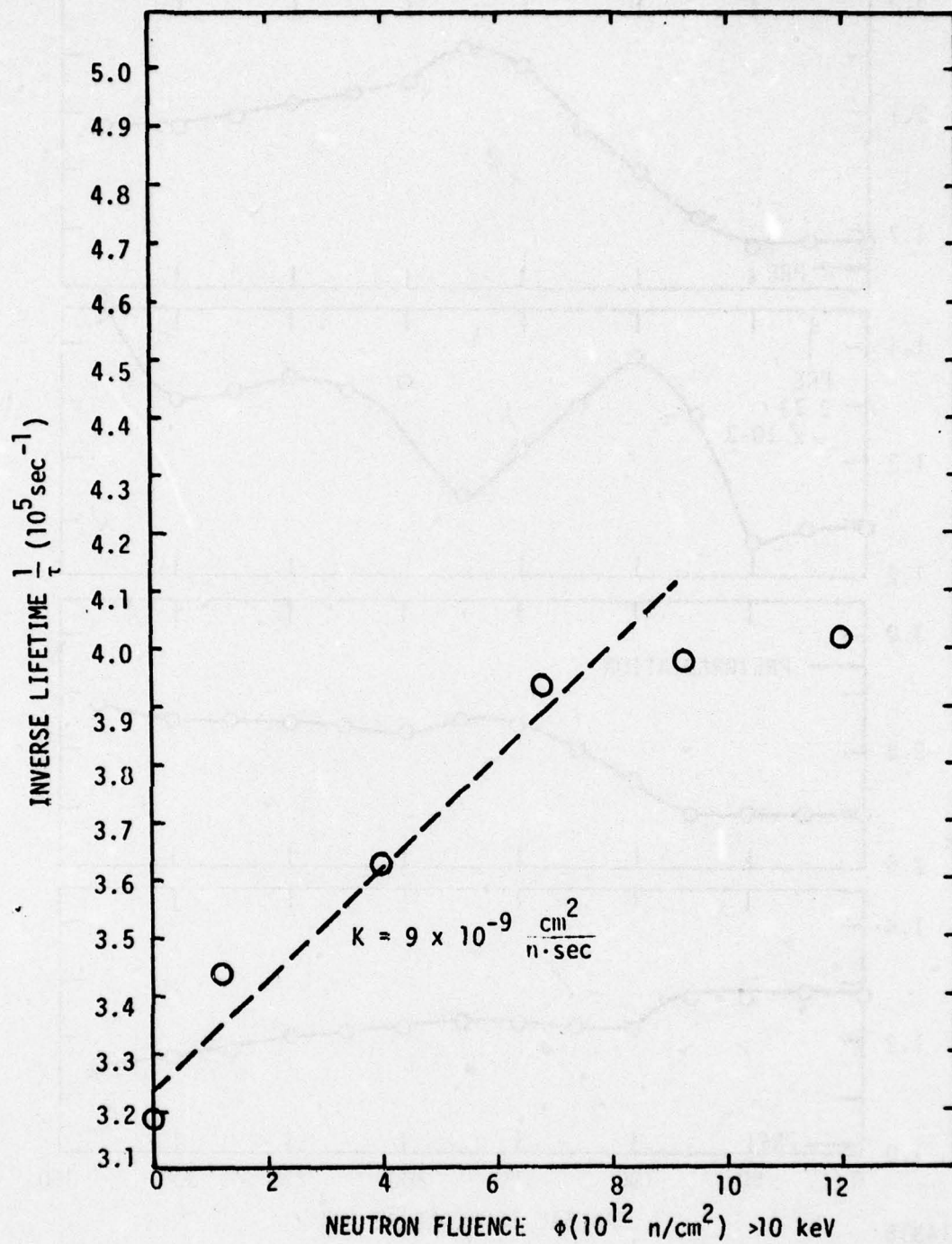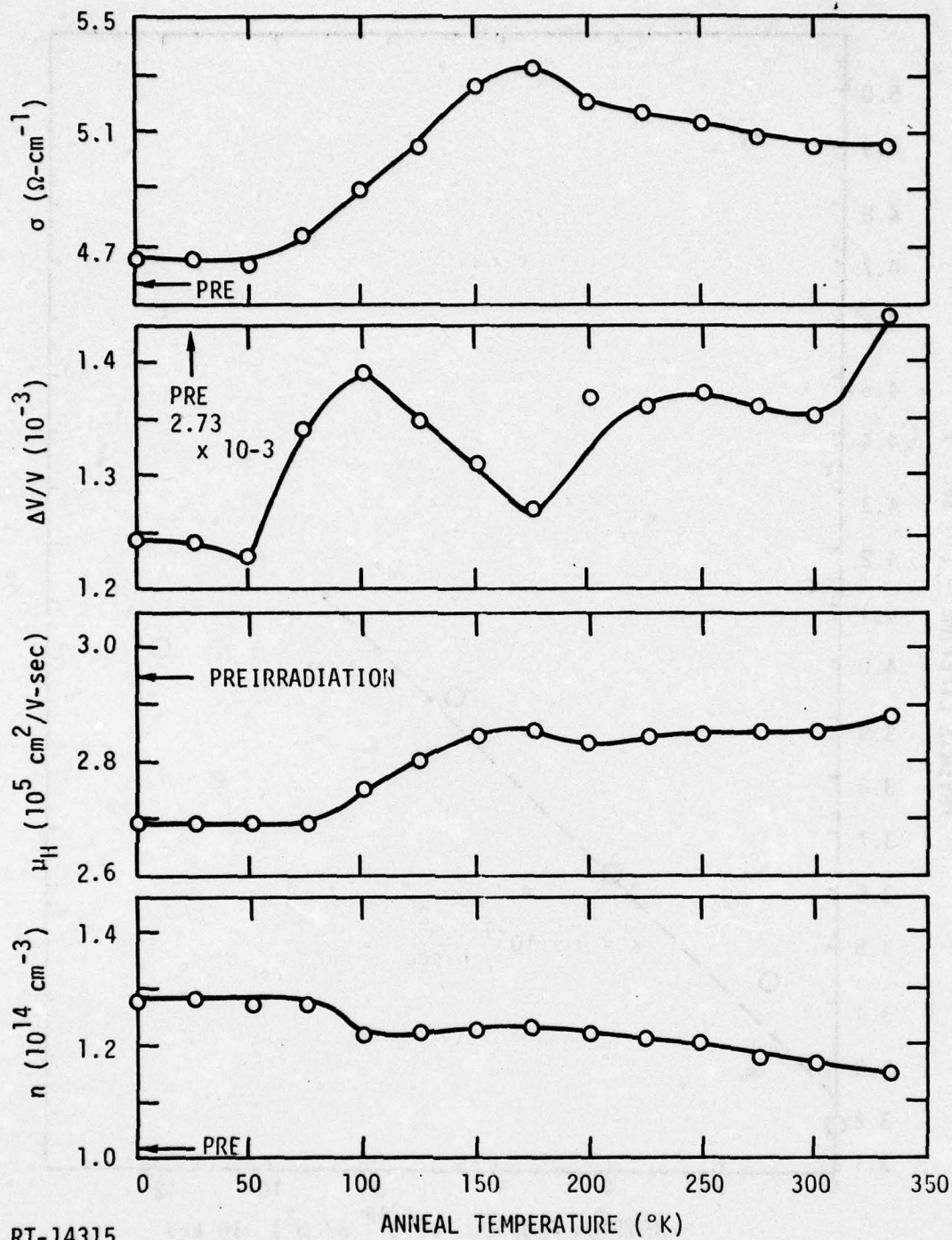
RT-14312

Figure 5-22   Steady-state photoconductivity versus
neutron fluence at 10°K, Sample I-1

88

RT-14340

**Figure 5-23   Inverse lifetime versus neutron fluence
10°K, Sample I-1**

89

RT-14315

Figure 5-24   Isochronal anneal (10 min) of n, μ, SSPC, and σ after 10°K neutron irradiations, measurements made at 10°K after each anneal

90

recovery appears to be correlated with a decrease in carrier density, however, the increase in SSPC is greater than can be accounted for by the decreased carrier density ($\Delta V/V \propto 1/n$). The decrease in SSPC between 100 and 175°K and the following increase between 175 and 250°K does not appear to be correlated with a carrier density or mobility anneal. The electrical conductivity increased during the irradiation and continued to increase until after the 175°K anneal. The increasing conductivity was dominated primarily by mobility recovery. After the 340°K anneal, the following changes with respect to preirradiation values were noted.

Electrical conductivity	+20%
Steady-state photoconductivity	-50%
Hall mobility	- 5%
Carrier density	+15%

Carrier Lifetime

A comparison of lifetime measurements by photoconductive decay indicates that the lifetime decreased from ~3.1 to ~2.5 µsec during the neutron irradiation. A semilog plot of the PC decay before and after neutron irradiation is shown in Figure 5-25. In both cases, two decay components are present. The fast component is relatively unchanged by the irradiation, while the longer component is decreased from ~3.1 to 2.5 µsec by the neutron irradiation. Extrapolation of the longer time constant to zero time indicates that the amplitude of the steady-state photoconductivity signal was controlled approximately equally by the two lifetime components. This can also be seen from the inset in Figure 5-25, which is a photograph of sample response to a 15-µsec GaAs LED pulse before neutron irradiation. At the end of the injection pulse, the signal decreases to approximately 50% of its steady-state value with a time constant of about 0.3 µsec, then decays to zero with a longer time constant of approximately 3 µsec.

The carrier lifetime measured from photoconductive decay and calculated from SSPC during isochronal anneal is shown in Figure 5-26 and indicates no significant change during the anneal.

91

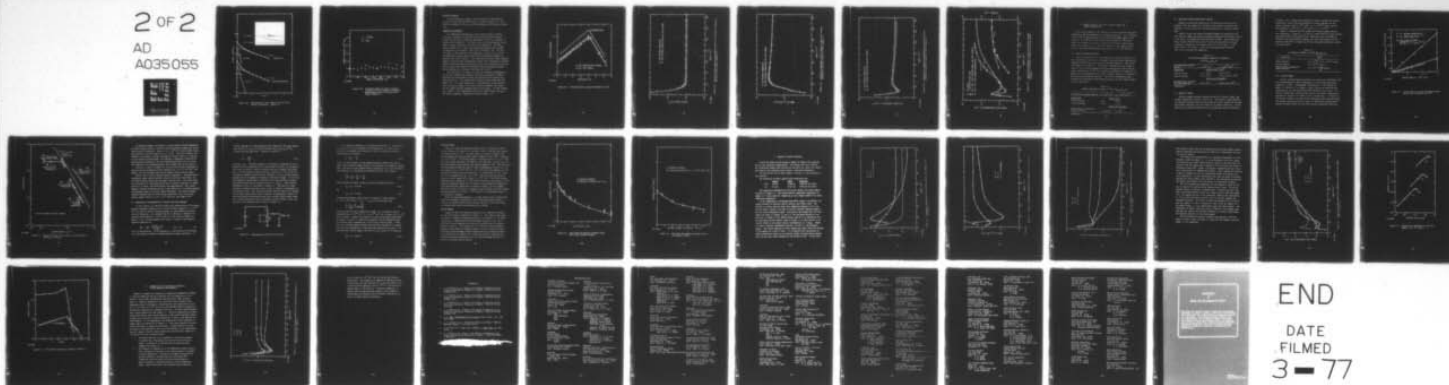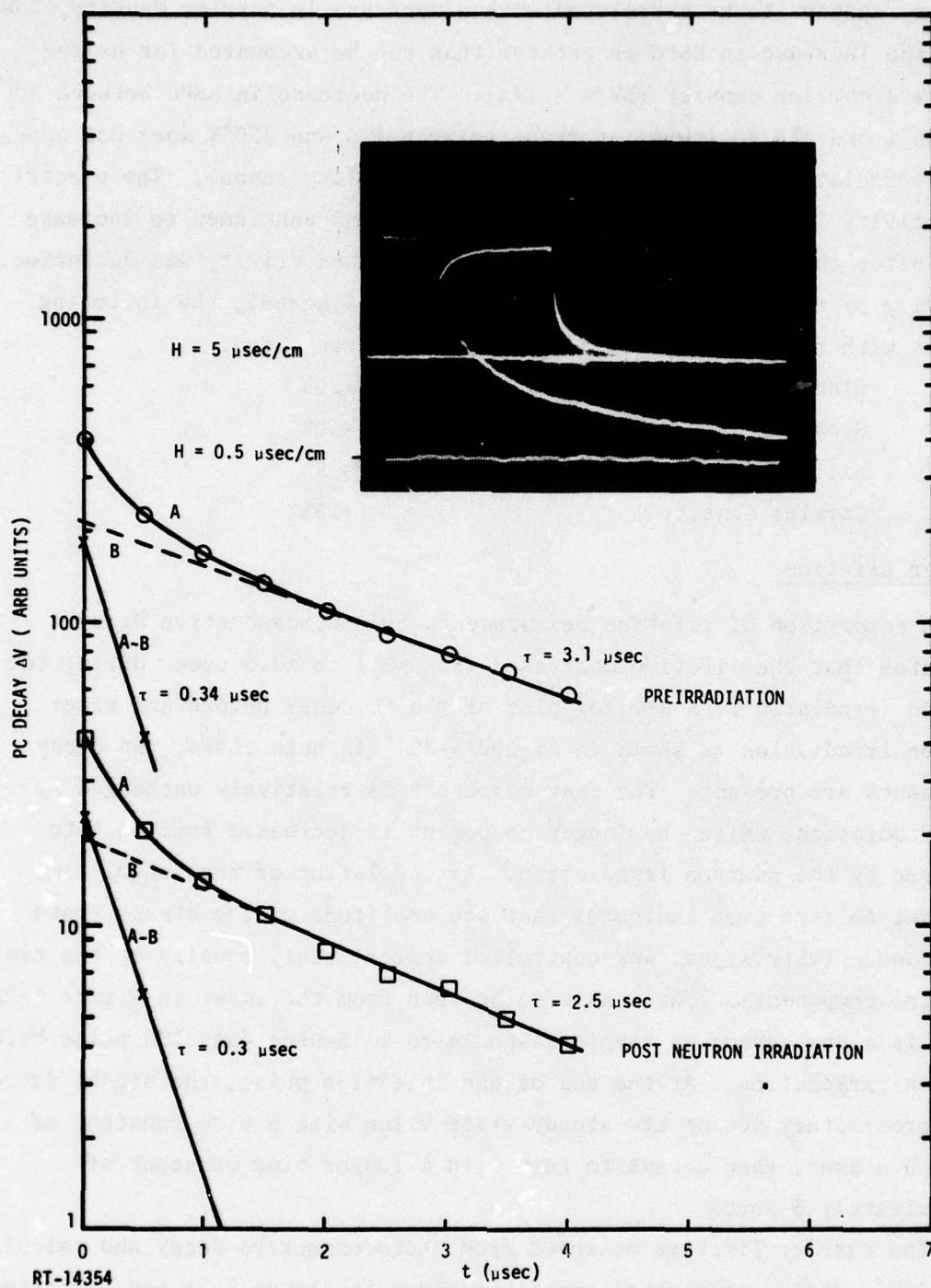Figure 5-25. Photoconductive decay before and after 10°K
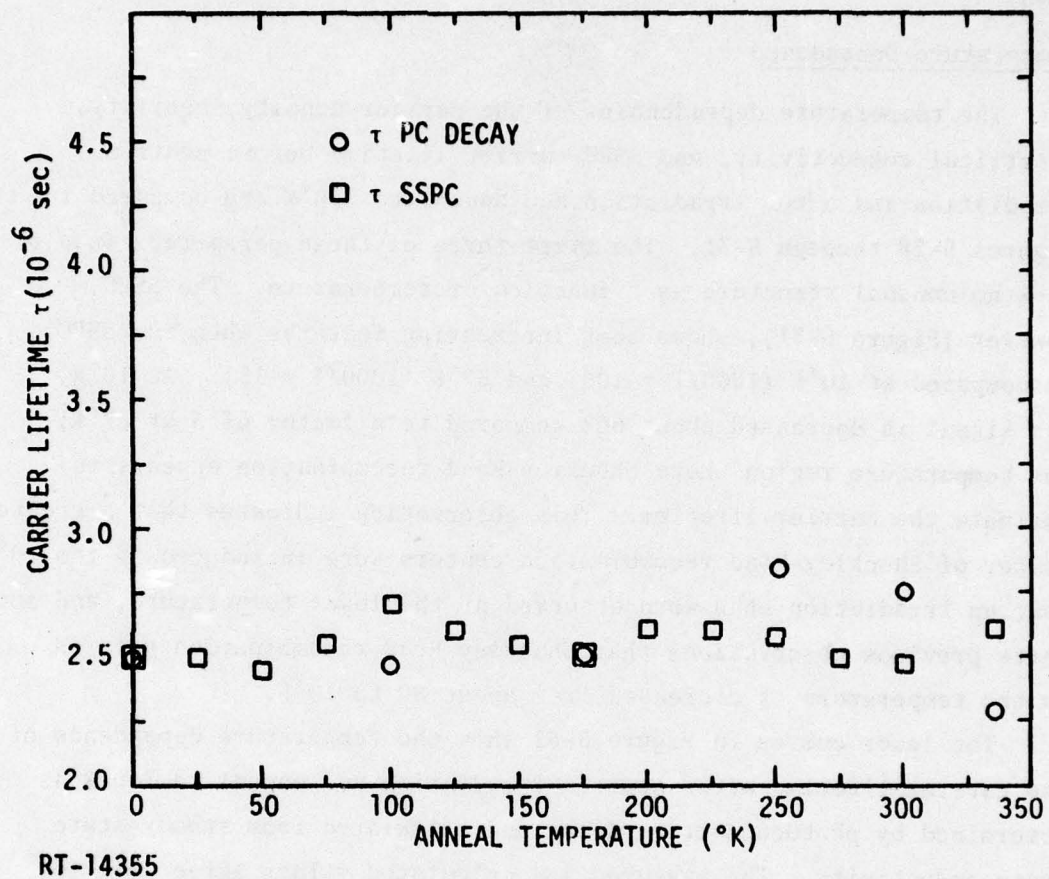neutron irradaition. Sample I-1.

92

RT-14355

Figure 5-26   Isochronal anneal (10 min) of carrier
lifetime after 10°K neutron irradiation,
measurements made at 10°K after each
anneal, Sample I-1

Spectral Response

The photoconductive spectral response before and after neutron irradiation and after the 300°K anneal is shown in Figure 5-27. The cutoff wavelength of $\sim$14 μm ($\lambda_{0.5}$) was unchanged by the neutron irradiation.

Temperature Dependence

The temperature dependencies of the carrier density, mobility, electrical conductivity, and SSPC-carrier lifetime before neutron irradiation and after irradiation and anneal to 340°K are compared in Figures 5-28 through 5-31. The first three of these parameters (n,μ,σ) show no unusual structure as a function of temperature. The SSPC, however (Figure 5-31), shows some interesting features when the SSPC is compared at 10°K (1000/T = 100) and 67°K (1000/T = 15). At 10°K, the signal is decreased about 60% compared to a factor of 3 at 67°K, the temperature region where Shockley-Read recombination appears to dominate the carrier lifetime. This observation indicates that a greater number of Shockley-Read recombination centers were introduced by the 10°K neutron irradiation than were observed at the lower temperature, and sup-ports *previous* observations that Shockley-Read recombination relaxes as the temperature is decreased from about 80 to 10°K.

The lower curves in Figure 5-31 show the temperature dependence of the carrier lifetime after neutron irradiation and anneal to 340°K as determined by photoconductive decay and calculated from steady-state photoconductivity. The measured and calculated values agree well for 1000/T > 90. At higher temperature, the disagreement arises partially from the relative weight of the short lifetime component (not shown) and the longer lifetime component shown in the figure. At lower tempera-ture (1000/T = 140), approximately 40% of the SSPC response was due to the shorter component, compared with $\sim$58% at 1000/T = 57.

94

RT-14317
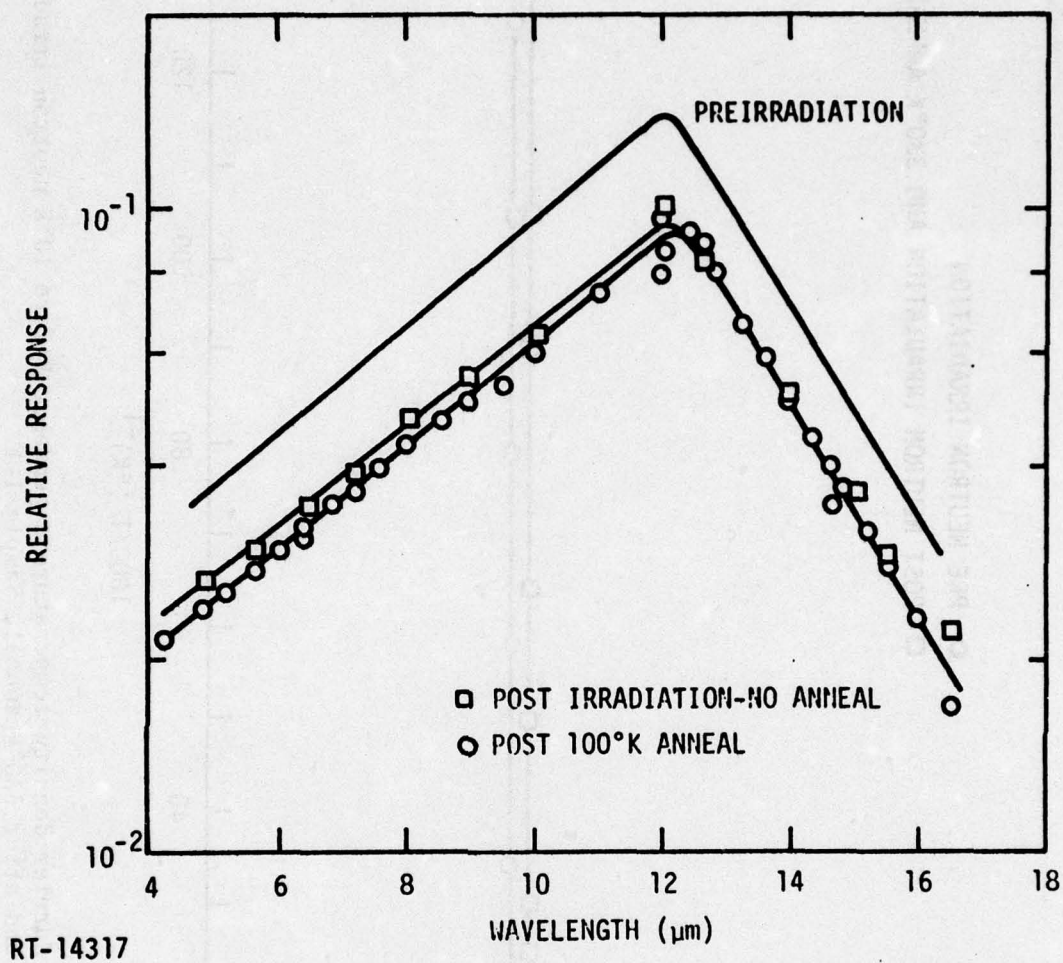
Figure 5-27   Photoconductivity spectral response at 10°K

PRE NEUTRON IRRADIATION

POST NEUTRON IRRADIATION AND 330°K ANNEAL

$1000/T \ (°K)^{-1}$

CARRIER DENSITY (cm^{-3})
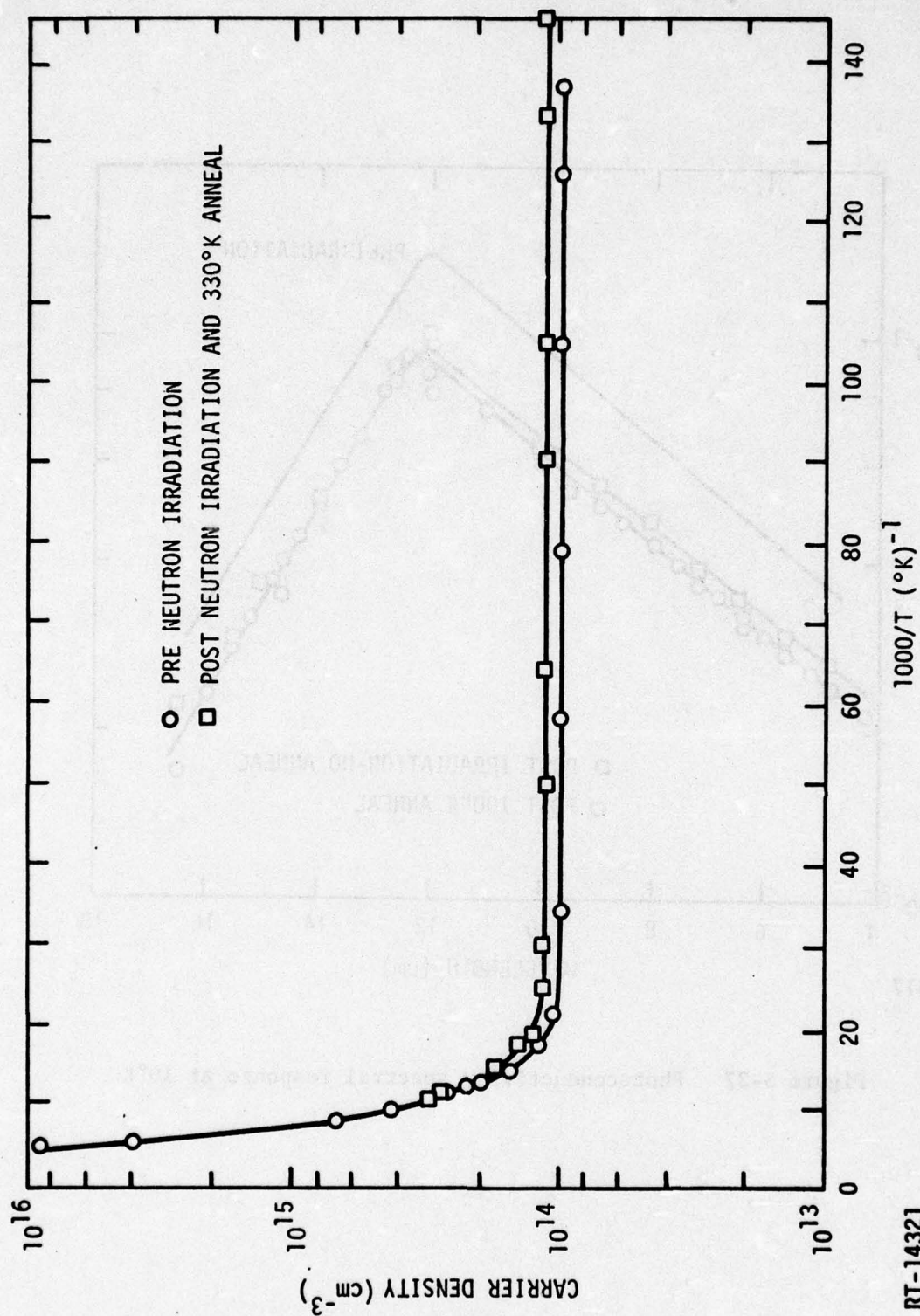
Figure 5-28 Carrier density temperature dependence before 10°K neutron irradiation and after 330°K anneal, Sample I-1

RT-14321

96
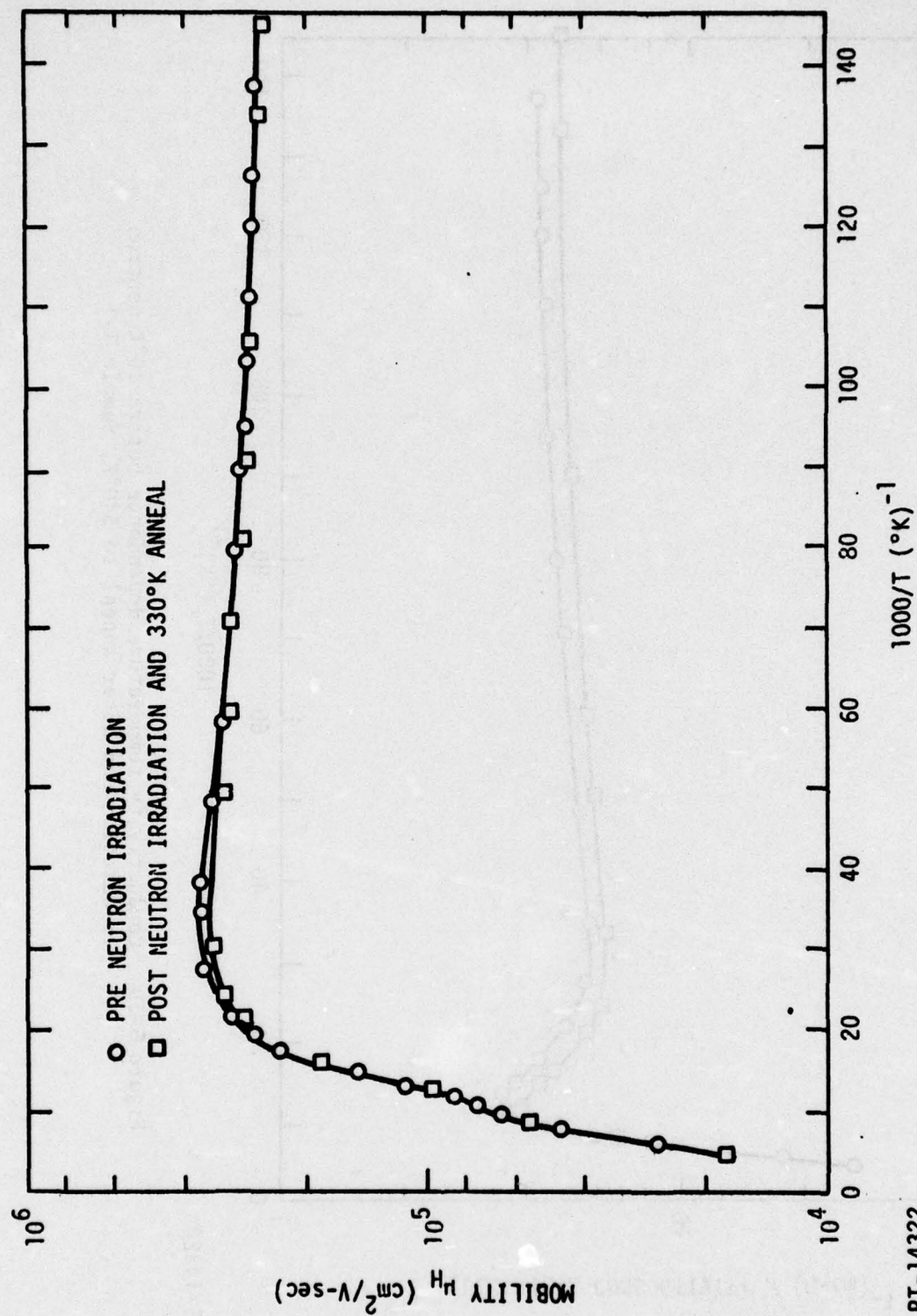
Figure 5-29 Temperature dependence of Hall mobility before 10°K neutron irradiation and after anneal to 340°K, Sample I-1

RT-14322

97

PRE NEUTRON IRRADIATION

POST NEUTRON IRRADIATION AND 330°K ANNEAL

ELECTRICAL CONDUCTIVITY σ $(\Omega\text{-cm})^{-1}$

100

10

1

0   20   40   60   80   100   120   140

$1000/T$ $(°K)^{-1}$

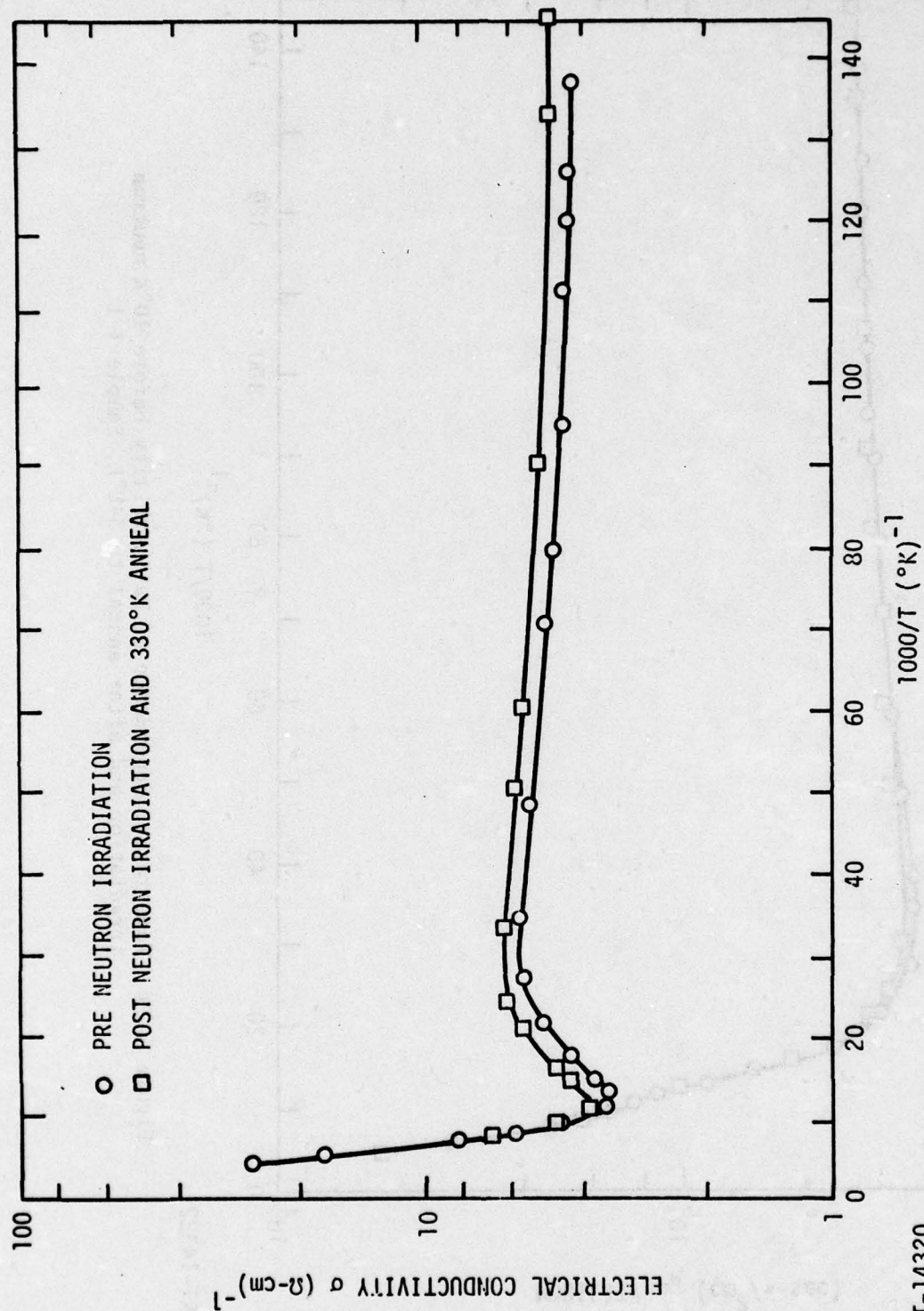Figure 5-30 Conductivity temperature dependence before 10°K neutron irradiation and after anneal to 340°K, Sample I-1

RT-14320

98

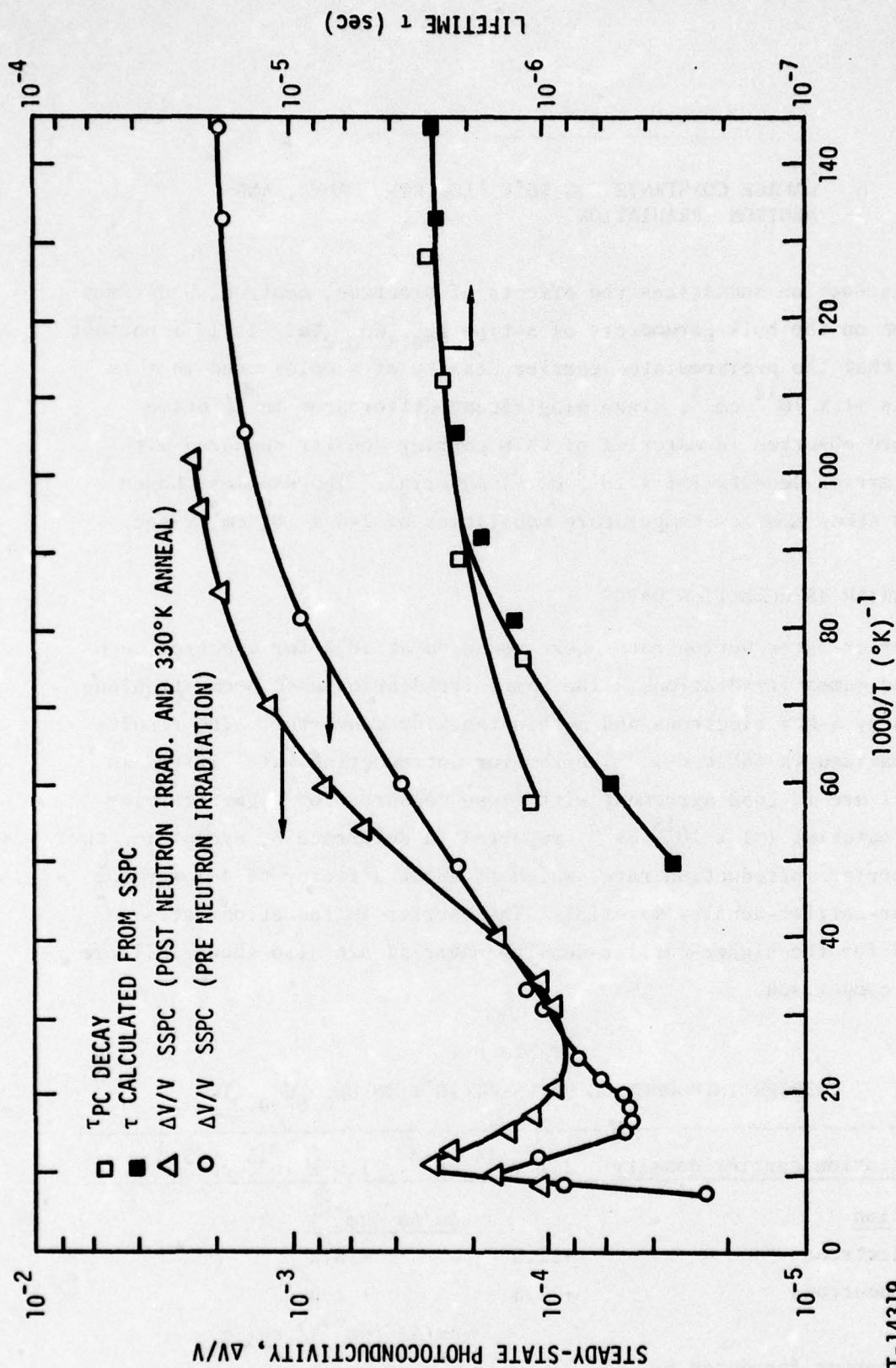Figure 5-31 Temperature dependence of SSPC and carrier lifetime before a 10°K neutron irradiation and after anneal to 340°K

RT-14319

99

6. DAMAGE CONSTANTS FOR 10°K ELECTRON, GAMMA, AND NEUTRON IRRADIATION

This section summarizes the effects of electron, neutron, and gamma radiation on the bulk parameters of n-type $Hg_{0.8}Cd_{0.2}Te$. It is important to note that the preirradiated carrier density of samples used in this study was $\sim 1 \times 10^{14}$ cm^{-3}, since singificant differences in lifetime damage are observed in material of this carrier density compared with higher-carrier-density ($\sim 1 \times 10^{15}$ cm^{-3}) material. The samples chosen for this study have low-temperature mobilities of $2-4 \times 10^5$ $cm^2/V \cdot sec$.

6.1 CARRIER INTRODUCTION RATES

Carrier introduction rates were measured at 10°K for electron, neutron, and gamma irradiations. The gamma irradiation used bremsstrahlung produced by 5-MeV electrons and a thin tantalum converter. The results are summarized in Table 6-1. The carrier introduction rates listed in Table 6-1 are in good agreement with those measured for higher-carrier-density material ($\sim 1 \times 10^{15}$ cm^{-3}) reported in Reference 8, except for the gamma carrier introduction rate, which is about a factor of 4 lower for the lower-carrier-density material. The carrier introduction rates obtained for the higher-carrier-density material are also shown in Table 6-1 for comparison.

Table 6.1

CARRIER INTRODUCTION RATES AT 10°K IN $Hg_{0.8}Cd_{0.2}Te$

Preirradiation carrier density	1×10^{14} cm^{-3}	1.5×10^{15} cm^{-3} [a]
Irradiation	$\Delta n/\Delta \phi$ (cm^{-1})	
5-MeV electrons	+12.5	+13.6
Fission neutrons	+ 2.5	+ 2.5
	$\Delta n/\Delta \phi$ $(cm^{-3})/rad(Si)$	
Bremsstrhalung (produced by 5-MeV electrons)	+ 2.5 x 10^7	1 x 10^8

[a]Reference 8

100

6.2 RADIATION-INDUCED CONDUCTIVITY CHANGES

Changes in electrical conductivity are important to detector performance since the conductivity determines the detector resistance and, therefore, the bias level for a detector operating in a constant current mode.

Table 6.2 gives the radiation-produced changes in conductivity for $10°K$ electron, gamma, and neutron irradiation discussed in Sections 4 and 5. In all cases, the conductivity increased with fluence. The increase was nearly linear; therefore the values of $\Delta\sigma/\Delta\Phi$ given in Table 6-2 can be considered constant for the fluences used (1.2×10^{13} n/cm^2, 7×10^{13} e/cm^2, and 1×10^6 rad(Si). Values for the higher-density-material (Ref. 8) are included for comparison.

Table 6-2

10°K RADIATION-PRODUCED CONDUCTIVITY CHANGES IN

n-TYPE $Hg_{0.8}Cd_{0.2}Te$

Pre-irradiation carrier density	1×10^{14} cm^{-3}	1.5×10^{15a} cm^{-3}
Irradiation	$\Delta\sigma/\Delta\Phi$ $(\Omega\text{-cm})^{-1}$ (cm^{-2})	
5-MeV electrons	$+1.7 \times 10^{-13}$	$+2.9 \times 10^{-13}$
Fission neutrons	$+4.6 \times 10^{-15}$	-2.3 to -0.97×10^{-15}
	$\Delta\sigma/\Delta\Phi$ $(\Omega\text{-cm}^{-1})$/rad(Si)	
Bremsstrahlung (produced by 5-MeV electrons)	$+7.5 \times 10^{-7}$	$+9.0$ to 2.4×10^{-6}

[a]Reference 8

6.3 MOBILITY DAMAGE

Mobility damage constants measured during $10°K$ electron, gamma, and neutron irradiation are given in Table 6-3. The mobility damage constants are obtained from the slope of inverse mobility versus fluence for electron and neutron irradiation and dose [rad(Si)] for gamma irradiation. Inverse mobility was linear with radiation for the gamma and neutron irradiation;

101

therefore, only a single damage constant is given. During the electron irradiation, inverse mobility exhibited two linear regions: one for fluences between 0 and 3×10^{13} e/cm^2, $K = 7 \times 10^{-20}$ V·sec/e, and the other between 3×10^{13} and 7×10^{13} e/cm^2, $K = 3.1 \times 10^{-20}$.

Figure 6.1 compares mobility damage for electron, gamma, and neutron irradiation. Figure 6.1 is a plot of inverse mobility versus increasing carrier density during the three irradiations and is included to illustrate the larger mobility damage, per carrier introduced, for the neutron irradiation as compared to electron and gamma irradiations, which are nearly equal.

Table 6-3

$10°K$ MOBILITY DAMAGE IN n-TYPE $Hg_{0.8}Cd_{0.2}Te$

Irradiation	$\Delta\frac{1}{\mu}/\Delta\Phi$
5-MeV electrons	3.1×10^{-20} to 7.4×10^{-20} V·sec/e
Fission neutrons	6.9×10^{-20} V·sec/n
Bremsstrahlung (produced by 5-MeV electrons)	$3.2 \times 10^{-13} \frac{V \cdot sec}{cm^2}/rad(Si)$

6.4 LIFETIME DAMAGE

Carrier lifetimes during irradiation and anneal were determined from direct photoconductive decay measurements or from steady-state photo-conductivity ($\Delta V/V$). During gamma irradiation of 1×10^6 rad(Si) of Sample I-1 (Section 5), no change in decay lifetime was observed when comparing pre- and post-irradiation photoconductive decay curves. The carrier lifetime data resulting from electron and neutron irradiation is presented in Figure 6-2 as Curves A and E, respectively. In Figure 6-2, the carrier lifetime is plotted versus increasing carrier density during the neutron irradiation (Curve E) and as a function of carrier density during isochronal anneal for the 5-MeV electron irradiation (Curve A).

INVERSE MOBILITY $1/\mu_{||}$ (10^{-6} V-sec/cm^2)

4.6

4.4

4.2

4.0

3.8

3.6

○ $1/\mu$, NEUTRON IRRADIATION $\}$ I-1

□ $1/\mu$, GAMMA IRRADIATION

△ $1/\mu$, 5-MeV ELECTRONS
(NORMALIZED TO 3.5 x $\}$ II-4
10^{-6} AT n = 1 x 10^{14})

0   1.1   1.2   1.3

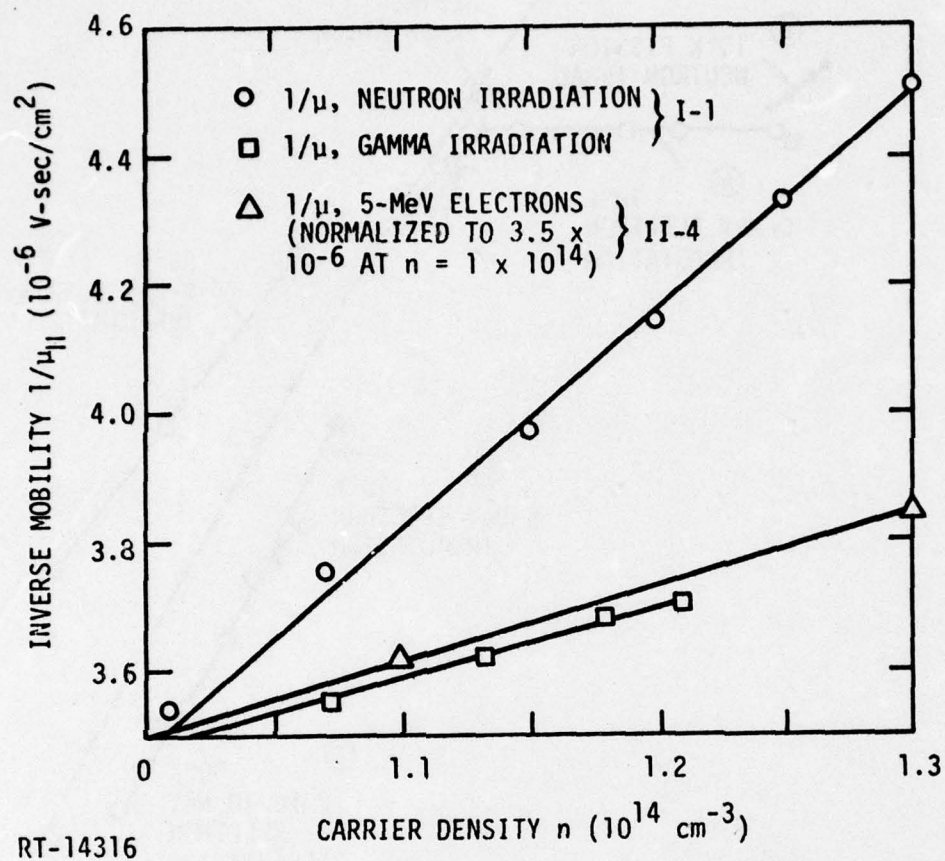CARRIER DENSITY n (10^{14} cm^{-3})

RT-14316

Figure 6-1   Inverse mobility versus increasing carrier
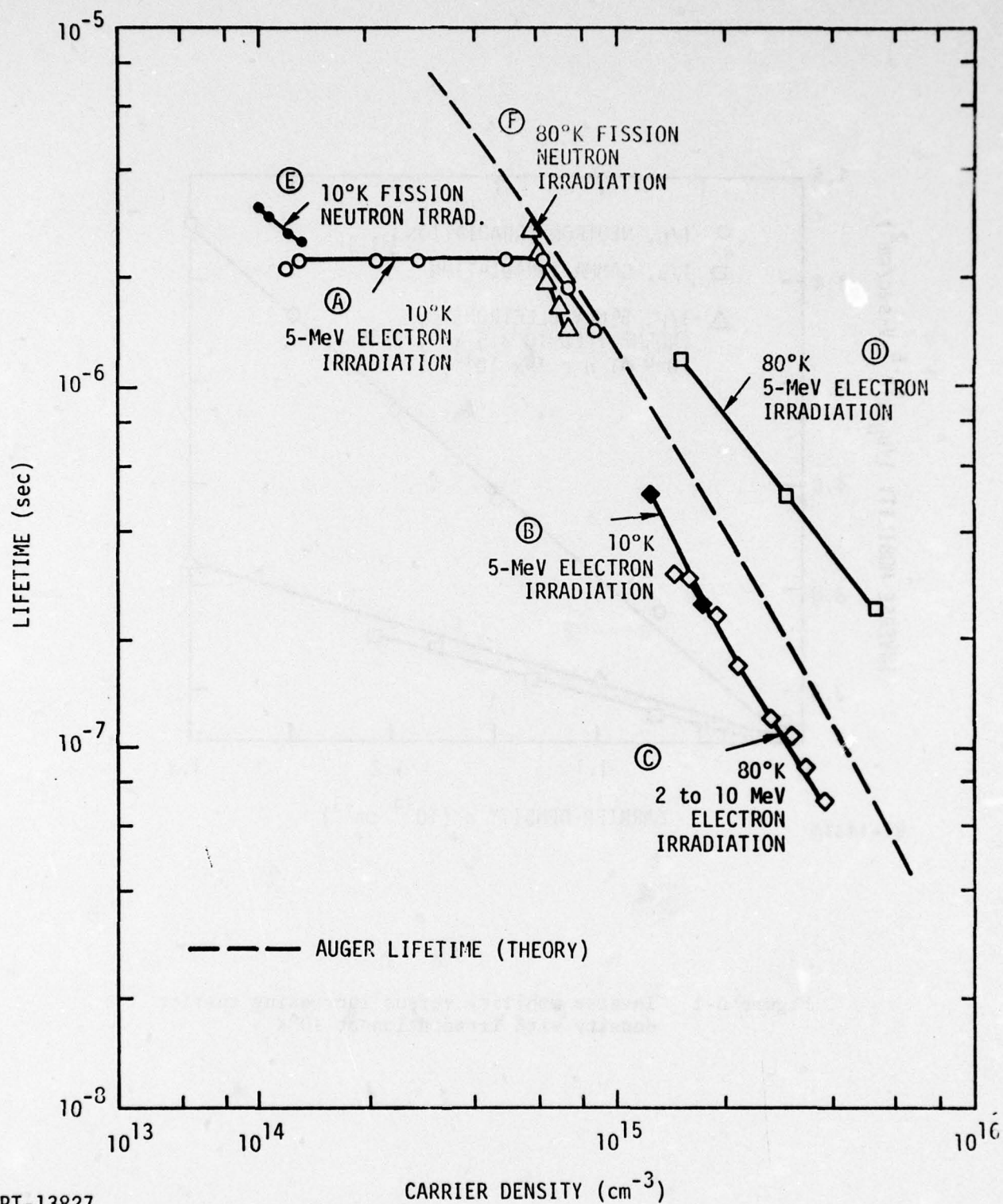density with irradiation at 10°K

103

Figure 6-2   Carrier lifetime versus change in carrier density
produced by radiation

RT-13827

104

An important feature of Figure 6-2 is the carrier lifetime dependence on carrier density (Curve A) for the low-carrier-density sample used in the 5-MeV electron irradiation. Above $n \simeq 6.5 \times 10^{14}$ cm^{-3}, the lifetime follows the theoretical extrinsic Auger curve ($\tau \propto 1/n^2$). Below this density, the lifetime is essentially constant although the carrier density is changing. In this contant-lifetime region, the lifetime is apparently controlled by Shockley-Read recombination, and the recombination defects are not noticeably affected by the annealing process which changes the carrier density.

Curves B, C, and D in Figure 6-2 are also for electron irradiation of samples with pre-irradiation carrier densities of 1 to 1.5×10^{15} cm^{-3} and appear to follow the Auger curve in this higher carrier density region.

Curves E and F are for fission neutron irradiations. Although neutron irradiation causes carrier addition similar to electron irradiation, the lifetimes decrease faster than the Auger lifetime curve. This trend could be an indication of clustering effects due to neutron irradiation in HgCdTe because it is known, both theoretically and experimentally, that cluster damage in neutron-irradiated silicon is more effective as a lifetime degradation mechanism than as a carrier removal mechanism. The lifetime damage constant obtained from the 10°K neutron irradiation of the low-carrier-density sample (Curve E) is $\sim 9.1 \times 10^{-9}$ $cm^2/n \cdot sec$ (see Figure 5-23).

6.5 PREDICTION OF PHOTOCONDUCTIVE DETECTOR RADIATION RESPONSE

In this section, the radiation effects data obtained from 10°K electron, neutron, and gamma irradiation of low-carrier-density HgCdTe ($n \sim 1 \times 10^{14}$ cm^{-3}) are used to predict radiation damage in a photoconductive detector. For this discussion, it is assumed that the PC detector is operated in a constant current mode in a circuit similar to that shown in Figure 6-3 where $R \gg R_d$. The photoconductivity signal is related to the detector material properties by

$$\frac{\Delta V}{V} = \frac{\Delta \sigma}{\sigma} = \frac{g \tau e (\mu_n + \mu_p)}{n_0 \, e \mu_n} \qquad (\Delta V \ll V) \qquad (6)$$

for an n-type detector. In this equation, V is the detector bias voltage, ΔV is the change in detector voltage produced by signal injection, τ is

105

carrier lifetime, g is the generation rate produced by the signal photon flux ($cm^{-3}sec^{-1}$), n_0 is the carrier density and μ_n and μ_p are the electron and hole mobilities. Equation 6 reduces to

$$\Delta V = \frac{g\tau V}{n_0} , \tag{6.1}$$

since $\mu_n \gg \mu_p$. The above equation is equivalent to responsivity R of a detector if ΔV is normalized to the signal power in watts, and the generation rate g is given in terms of quantum efficiency, bandgap, and photon flux. For the purpose of this discussion, however, Eq. 6.1 will be used for detector damage calculations and, therefore, will not include possible degradation due to bandgap or absorption coefficient changes. At low bias, the response is proportional to detector bias V and saturates at higher bias when minority-carrier sweepout occurs ($V \simeq L^2/\mu_p\tau$). This response dependence on bias is illustrated in Figure 7-5. The region of linear increase in response with bias occurs if the $\mu\tau$ product is independent of the electric field. This discussion assumes that the detector is operated in the linear region below carrier sweepout, as experimental results for both bulk material and detectors show that a plateau region beyond sweepout is never achieved and that the response actually reaches a peak, then decreases with increasing bias as shown in Figure 7-5.
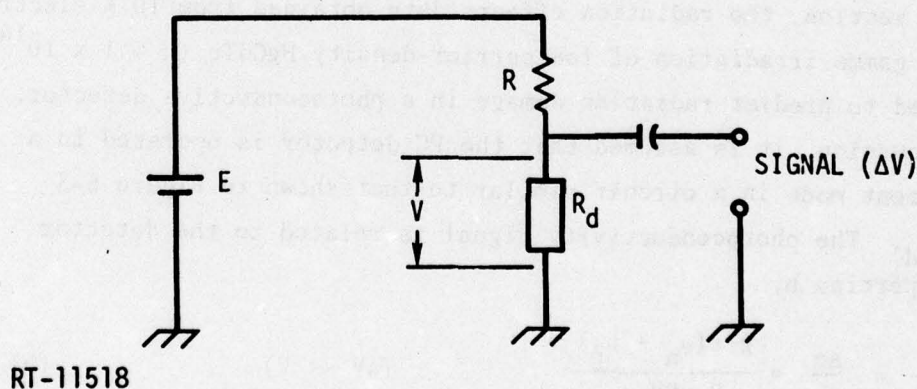
RT-11518

Figure 6-3. Photoconductive detector bias circuit

106

For a detector operating in a constant current mode, V, the detector bias in Eq. 6.1 can be replaced by the conductivity ($\sigma = CI/V$) which results in an equation for response (ΔV) which includes the parameters that change with radiation,

$$\Delta V = \frac{g\tau}{n} \times \frac{CI}{\sigma} . \tag{6.2}$$

In Eq. 6.2 the constant C is the detector geometry factor (ℓ/A) and is equal to the detector length divided by the detector area normal to current flow. The ratio of the response during irradiation, ΔV_R to the preirradiation response, ΔV, eliminates the constants from Eq. 6.2, leaving

$$\frac{\Delta V_R}{\Delta V} = \frac{\tau_R}{\tau_0} \times \frac{n_0}{n_R} \times \frac{\sigma_0}{\sigma_R} . \tag{6.3}$$

From the previous tables, n_R and σ_R can be calculated as follows.

$$n_R = n_0 + \Phi \, \Delta n/\Delta \Phi \tag{6.4}$$

and

$$\sigma_R = \sigma_0 + \Phi \, \Delta\sigma/\Delta\Phi \tag{6.5}$$

In the carrier density region where the lifetime is Auger-limited ($n > 6.5 \times 10^{14}$) where $\tau \propto \frac{1}{n^2}$, τ_R/τ_0 can be calculated from

$$\frac{\tau_R}{\tau_0} = \left(\frac{n_0}{n_0 + \Phi \, \Delta n/\Delta\Phi} \right)^2 . \tag{6.6}$$

During the 10°K neutron irradiation of sample I-1, the carrier density increased from $\sim 1 \times 10^{14}$ cm^{-3} to 1.3×10^{14} cm^{-3} for a fluence of 1.2×10^{13} n/cm^2 (>10 keV). Based on the results of electron and gamma irradiations of samples II-4 and I-1, there was no apparent lifetime degradation due to increased Auger recombination in this carrier density range. Therefore, the lifetime damage observed during neutron irradiation is assumed to result from introduction of Shockley-Read recombination centers. For Shockley-Read lifetime damage, the ratio of τ_R/τ_0 in Eq. 6.3 is given by

$$\frac{\tau_R}{\tau_0} = (1 + K\Phi\tau_0)^{-1} . \tag{6.7}$$

107

Electron Damage

Figure 6-4 shows the measured response (ΔV) as a function of 5-MeV electron fluence for sample II-4 (Sections 4 and 5), and also the response calculated using Eq. 6.3.   The open squares in Figure 6-4 neglect any lifetime damage and underestimate response damage by about 70% at a fluence of 7×10^{13} e/cm^2.   If lifetime damage is considered for $\Phi > 6 \times 10^{13}$ e/cm^2, the solid square data points of Figure 6-4 are obtained.   In this case, the calculated damage underestimates the measured damage by $\sim 25\%$.   The calculated lifetime damage assumes the onset of Auger recombination to occur at a carrier density of 6.5×10^{14} cm^{-3} ($\Phi = 5.4 \times 10^{13}$ e/cm^2 for sample II-4), and beyond this fluence and carrier density, τ is proportional to $1/n^2$.   Equation 6.6 was applied with $n_0 = 6.5 \times 10^{14}$, and the fluence was actually taken as a delta fluence of Φ minus 5.4×10^{13} e/cm^2.   The total response degradation at a fluence of 7×10^{13} e/cm^2 consisted of three parts: (1) the response decreased a factor of 6.7 because of the increase in conductivity which decreases the sample bias for constant current; (2) the response decreased a factor of 10 due to increased carrier density; (3) the lifetime decrease between $\Phi = 6.1$ and 7×10^{13} resulted in an additional factor of 1.5 decrease in response.

While not shown experimentally, it seems possible that a scheme which senses the increase in conductivity with irradiation could be used to increase the detector bias current and thus partially avoid the decrease in response that occurs with decreasing bias voltage.

Neutron Damage

Figure 6-5 shows the measured response ΔV as a function of fluence for the 10°K neutron irradiation of sample I-1.   Also shown in the figure are values of response calculated using Eqs. 6.3 through 6.7.   For these calculations, a Shockley-Read lifetime damage constant K of 9×10^{-9} cm^2/n·sec was used together with the values of $\Delta n / \Delta \Phi$ and $\Delta \sigma / \Delta \Phi$ given in Tables 6.1 and 6.2.   At a fluence of 1.2×10^{13} n/cm^2, the calculated response overestimates the damage slightly ($\sim 7\%$) as a result of using a worst-case-lifetime damage constant measured during the neutron irradiation (dashed line in Figure 5-23).   During the neutron irradiation the response decreased approximately 25% from lifetime damage and 13% as a result of increased carrier density.
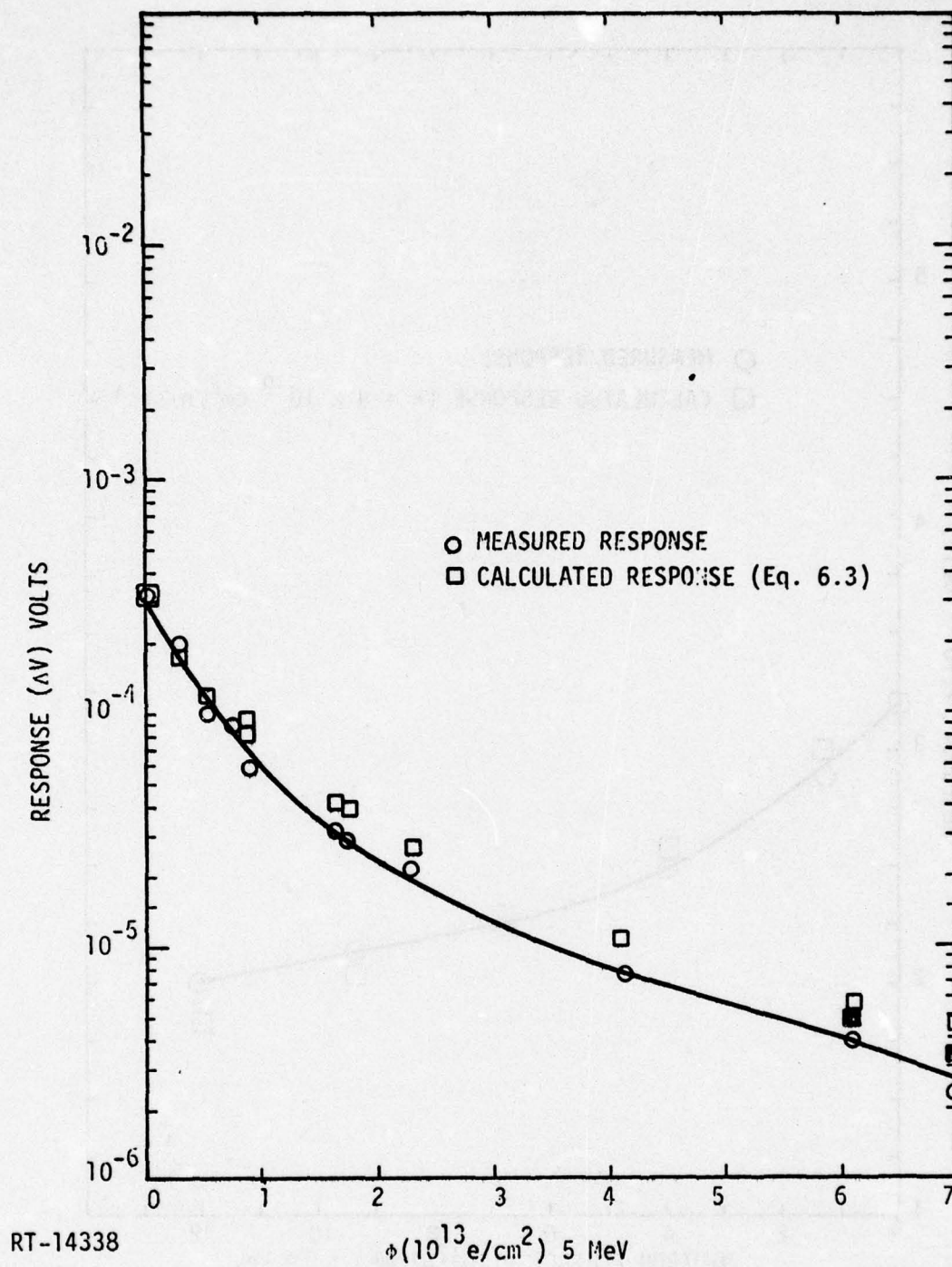
108

RT-14338

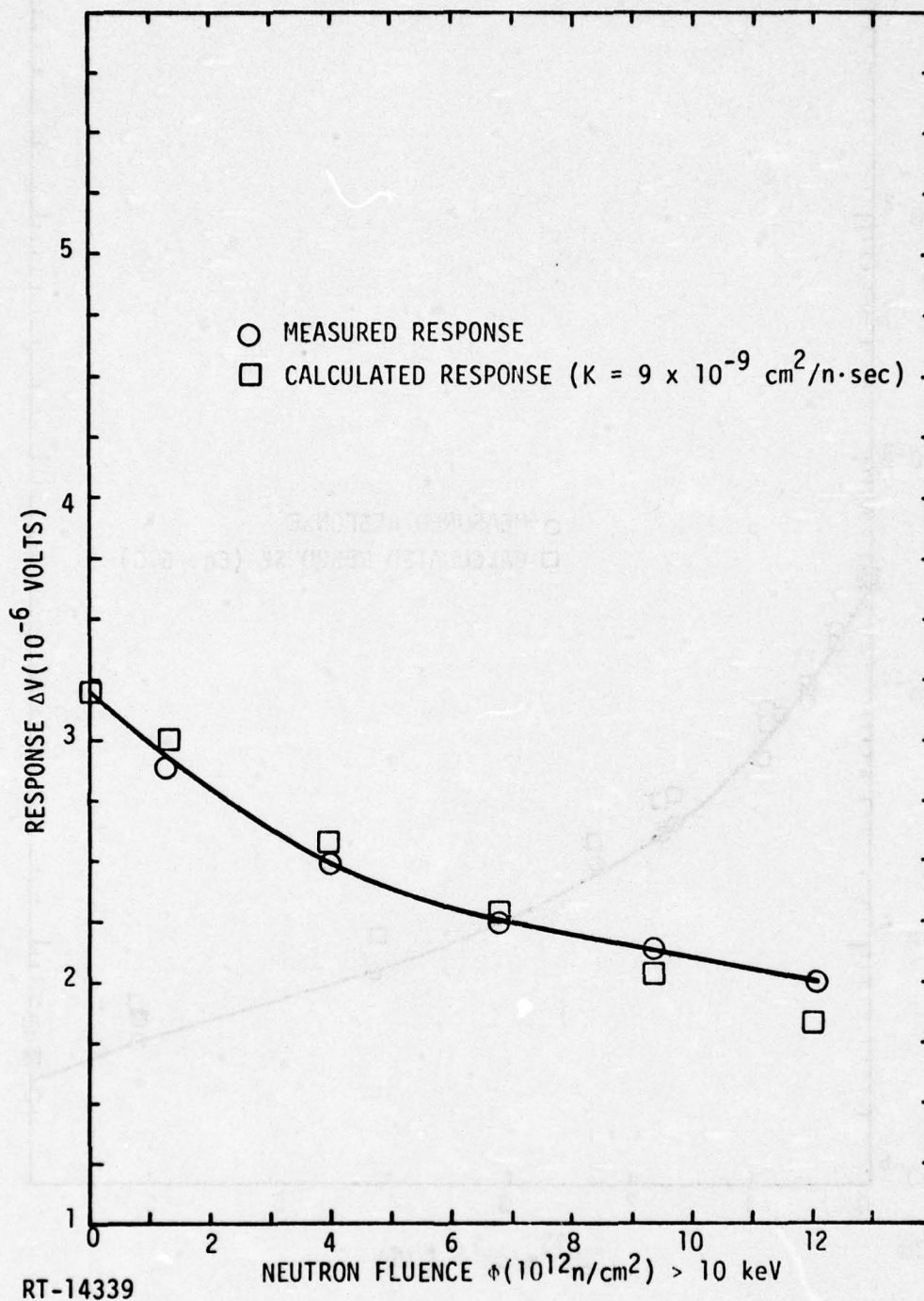Figure 6-4   Calculated and measured response versus
10°K, 5 MeV electron fluence

109

Figure 6-5   Calculated and measured response versus
10°K neutron fluence

RT-14339

110

7. RESULTS OF SAMPLE SCREENING

During the course of the program a number of samples were prepared
and at least partially characterized. The samples that were rejected
for irradiation studies were rejected on the basis of a small low tempera-
ture mobility and abnormal carrier density temperature dependence.

The results for two of these samples, I-1b and I-4, are presented in
this section.

The dimensions of these samples after preparation was

	Length	Width	Thickness
I-1b	0.6 cm	0.056 cm	0.023 cm (9.2 mils)
I-4	0.5 cm	0.121 cm	0.013 cm (5.2 mils)

The temperature dependence of the carrier density for these samples
is given in Figure 7-1. The carrier density temperature dependence for
sample I-1 is also shown for comparison, as this sample exhibits the normal
temperature dependence.

As the temperature is decreased from $300°K$, sample I-1b exhibits the
normal decrease in intrinsic carrier density until about $120°K$. The
reversal in carrier density below this temperature appears to be a two
carrier effect; however, the sign of the Hall constant remained negative
for the entire temperature range. The mobility and conductivity for this
sample are shown in Figures 7-2 and 7-3. The continued decrease in con-
ductivity in Figure 7-3 for 1000/T greater than 20 is an indication that
the decreasing carrier density shown in Figure 7-1 is real and not a two
carrier effect in the carrier density determination ($n = 1/R_H e$). Sample
I-4 shows a behavior intermediate between I-1b and I-1, the reference
sample. The unusual behavior of these samples may result from the thinness
of the samples (5.2 and 9.2 mils). It is possible that the process of
sample preparation results in an inverted surface (p-type) which competes
with the bulk until hole freezeout at the surface occurs. In this case,
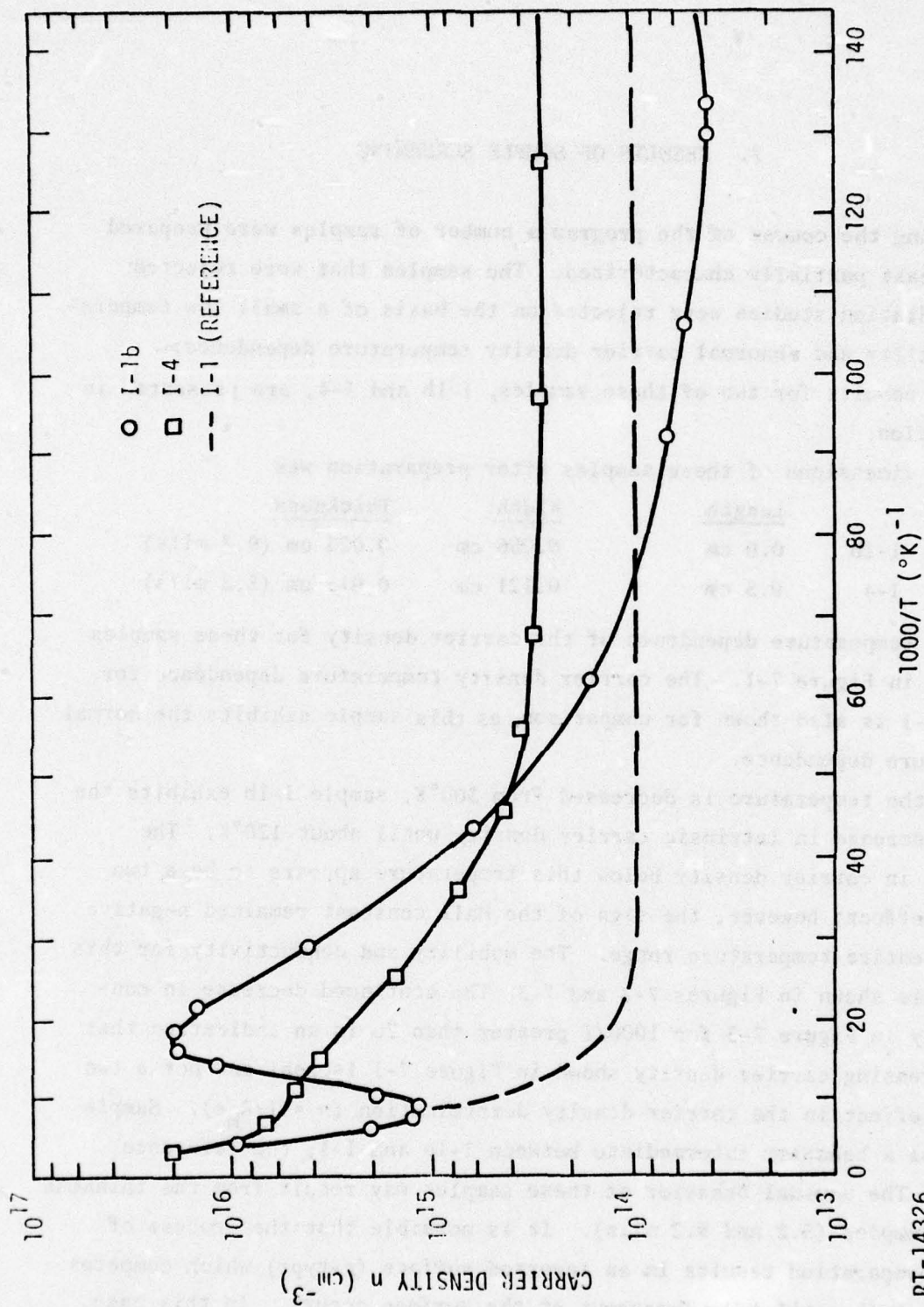
111

Figure 7-1 Temperature dependence of the carrier density for samples I-1b, I-4, and I-1

CARRIER DENSITY n (cm⁻³)

1000/T (°K)⁻¹
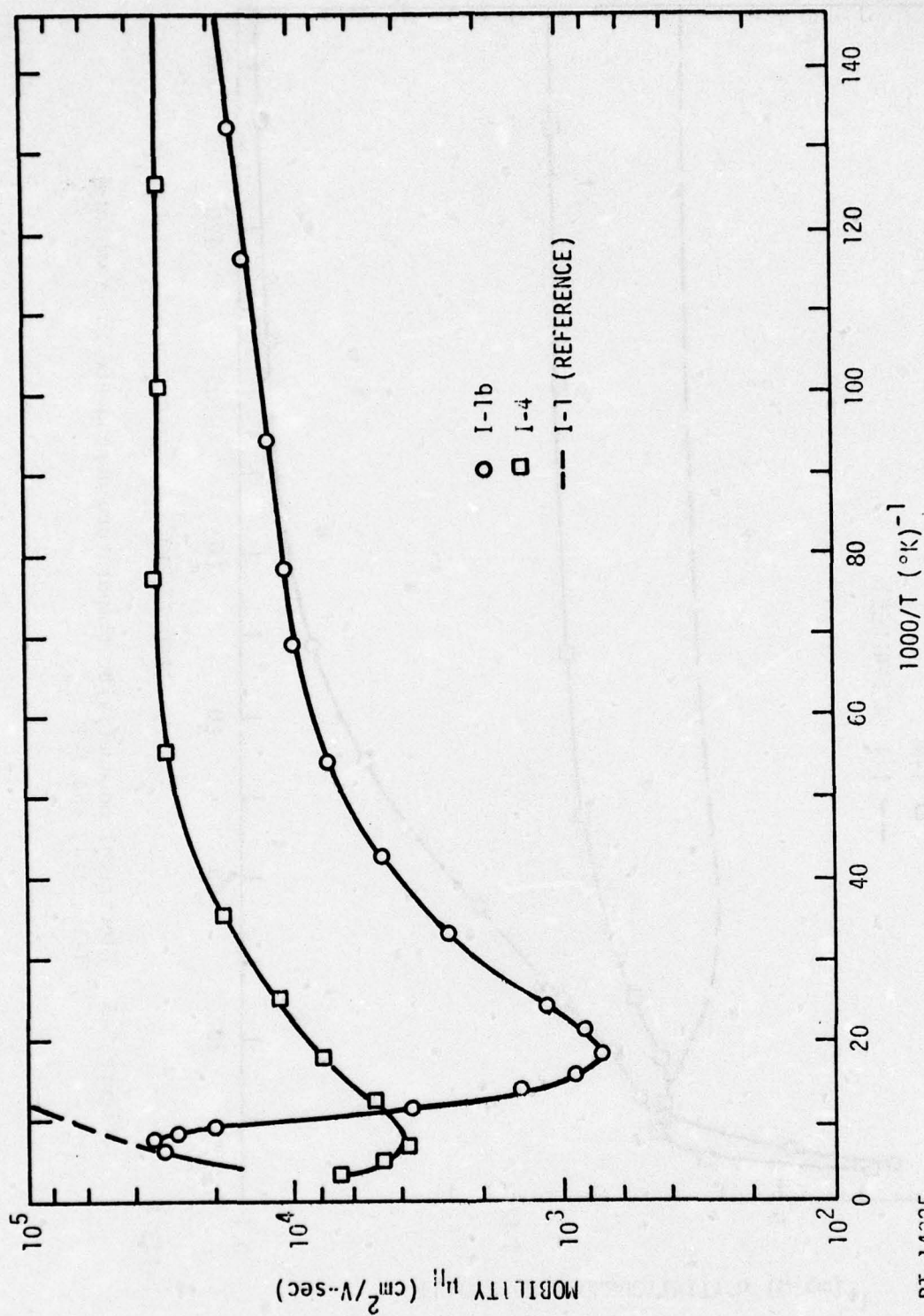
○ I-1
□ I-4
I-1 (REFERENCE)

Figure 7-2   Mobility temperature dependence for samples I-1b, I-4, and I-1
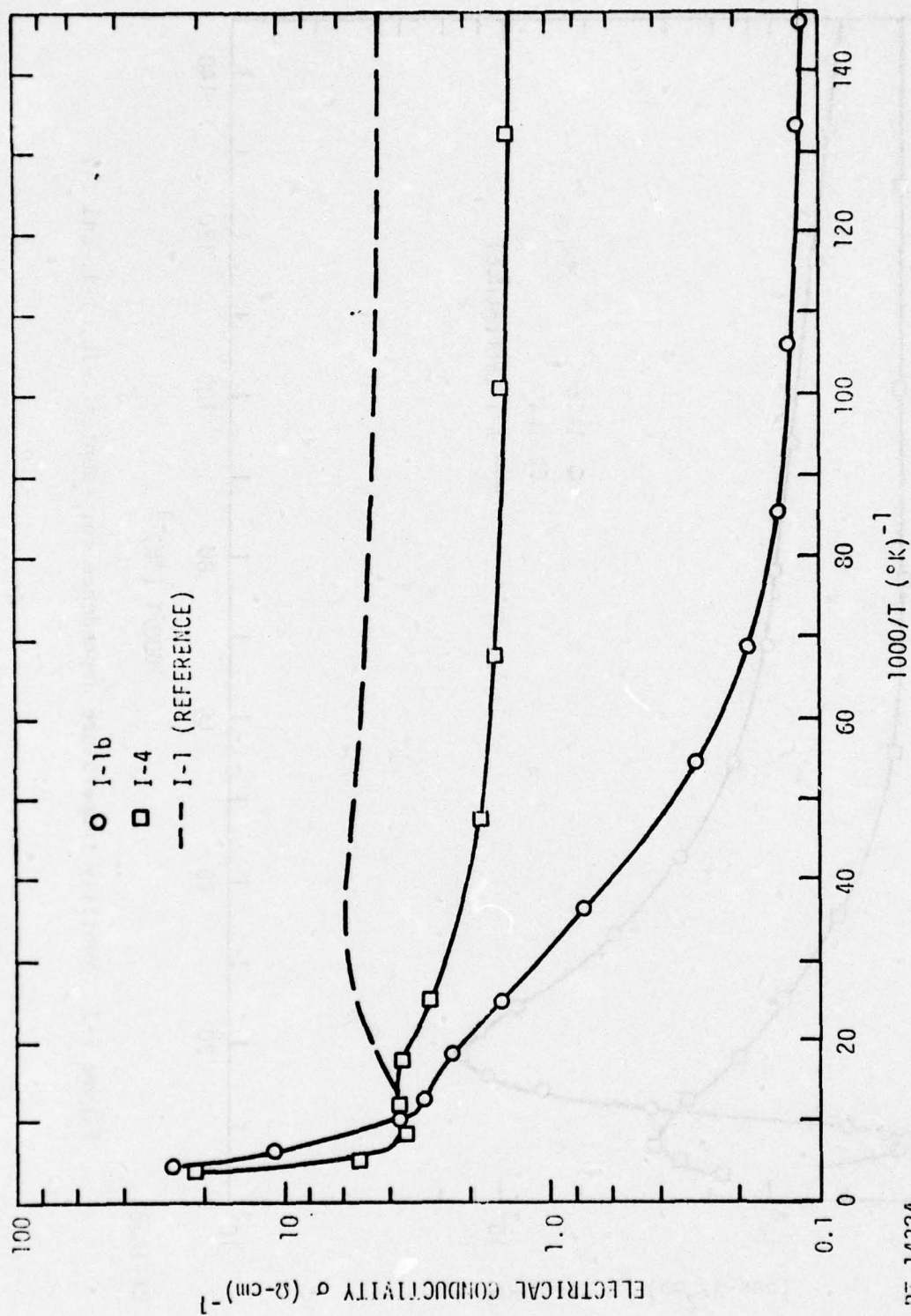
RT-14325

113

Figure 7-3   Electrical conductivity temperature dependence for samples
I-1b, I-4, and I-1

RT-14324

114

the surface to bulk ratio of the sample and the bulk and surface carrier density (electrons and holes) would be effective in determining the measured carrier density.

The steady-state photoconductivity temperature dependence for these samples is shown in Figure 7-4. It is interesting to note that sample I-1b which has the lowest carrier density, mobility, and electrical conductivity has the largest photo response at 10°K, and that this order is reversed at about 80°K. Sample I-1b appears compensated and thus likely has a large density of Shockley-Read centers. These centers are effective at 80°K as evidenced by the low response, and become less effective at lower temperature. An 80°K screening of this material based on response and mobility would probably have resulted in its elimination for detector fabrication even though it has the larger low temperature response.

The 10°K response bias dependence for the samples is given in Figure 7-5 where ΔV is plotted versus sample electric field. All of the samples exhibit a decrease in response above a certain bias level; however, the maximum response occurs at a larger electric field for sample I-1b. The reason for this is not understood, based on the relationship $V > L^2/\mu_p\tau$ which determines the bias level for carrier sweepout and response saturation. The carrier lifetime was measured to be $\sim$3 and 15 μsec for samples I-1 and I-4 respectively and $\sim$7 μsec for sample I-1b. The sample lengths, L, were approximately equal for these samples. The combination of sample length and carrier lifetime in the sweepout equation does not explain the observed differences in electric field where the response saturates for the three samples.

The photoconductive spectral responses was measured at 10°K for sample I-4 and is shown in Figure 7-6 along with the response curve for sample I-1 for comparison.
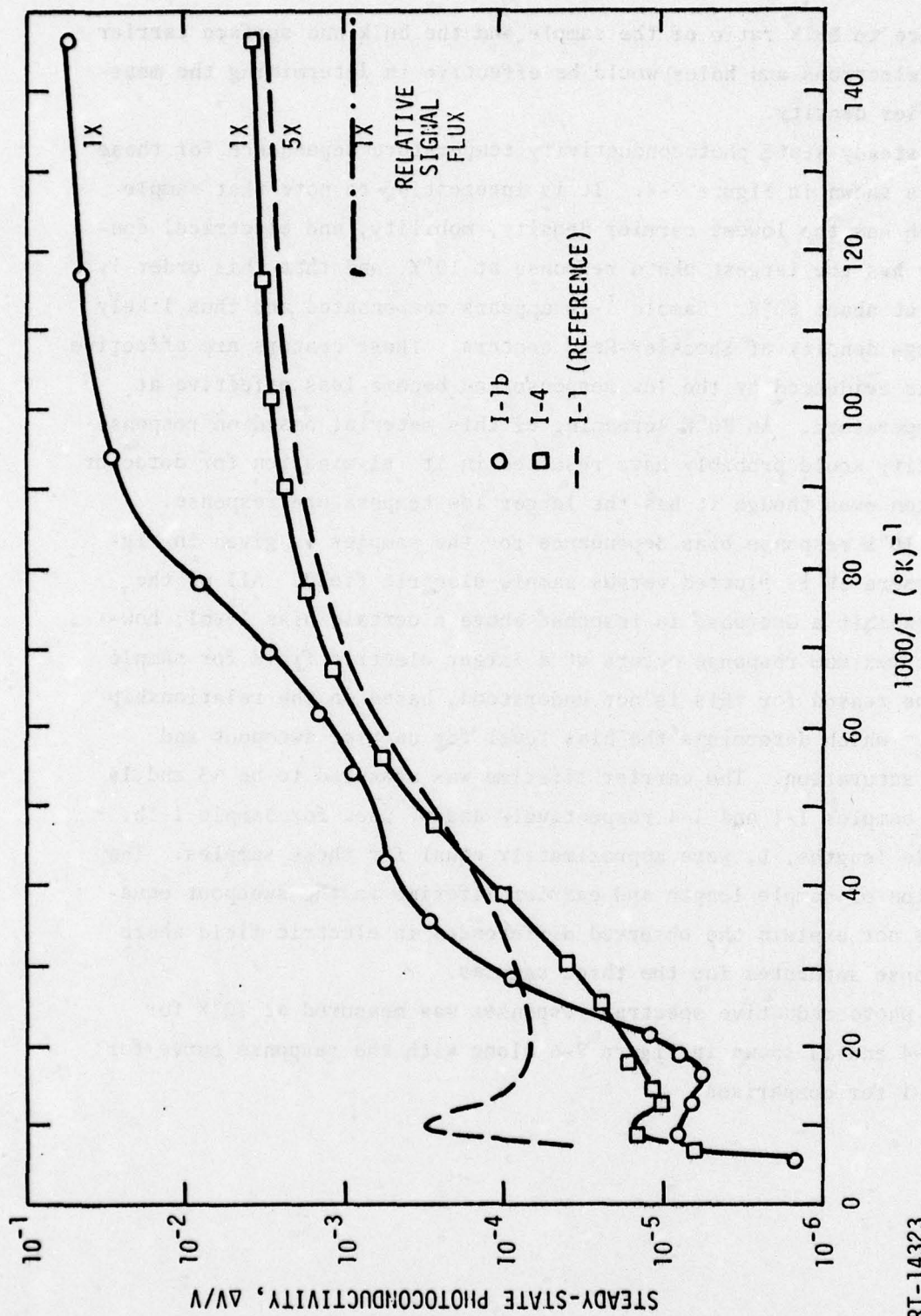
115

Figure 7-4 Steady-state photoconductivity temperature dependence for samples I-1b, I-4, and I-1

RT-14323

STEADY-STATE PHOTOCONDUCTIVITY, ΔV/V

$1000/T \ (°K)^{-1}$

RELATIVE SIGNAL FLUX

1X
1X
5X
1X

I-1b
I-4
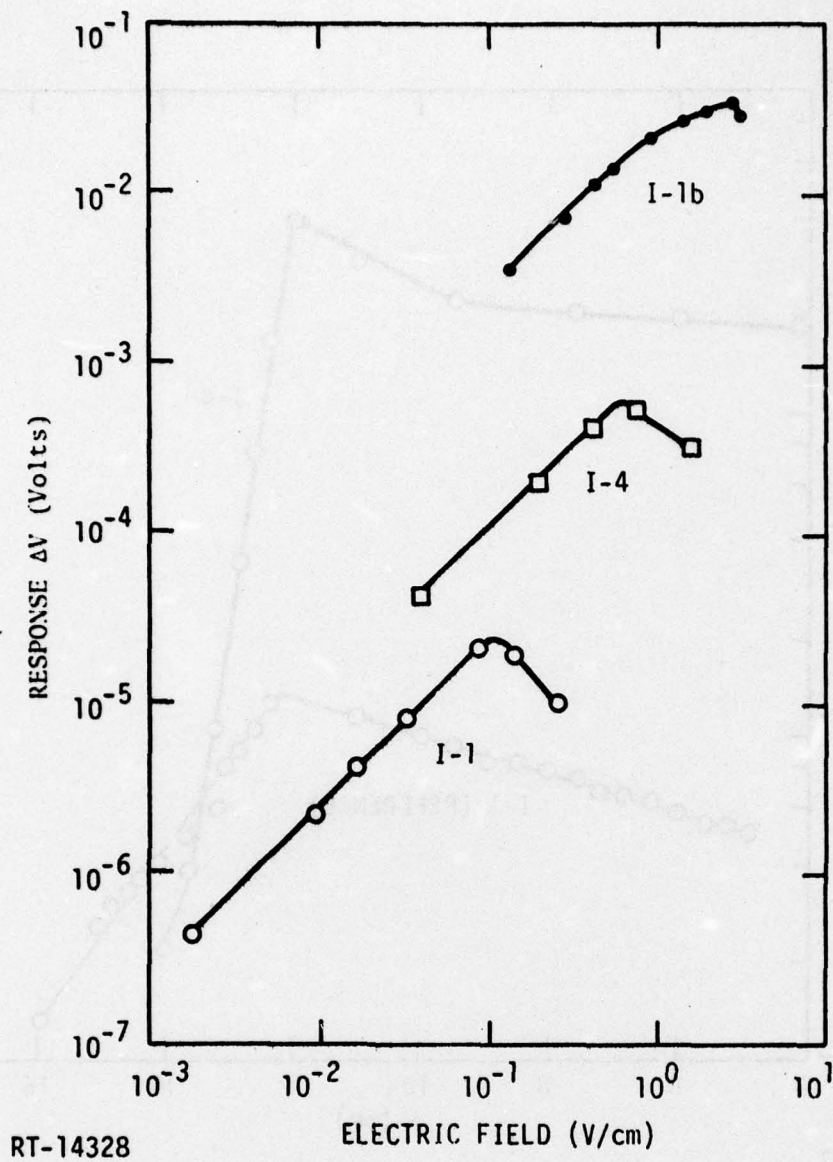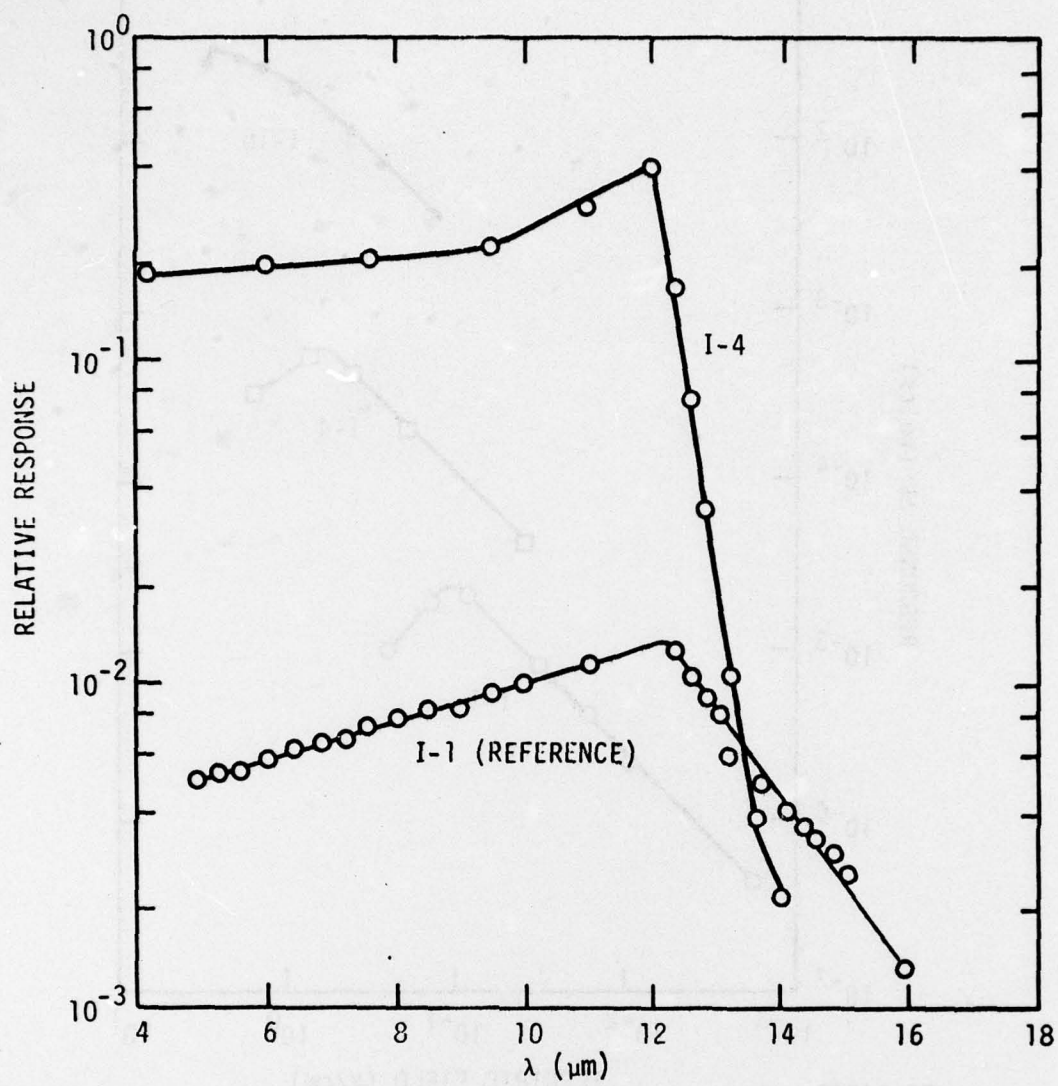I-1 (REFERENCE)

RT-14328

Figure 7-5   Response bias dependence at 10°K for
samples I-1b, I-4, and I-1

117

RT-14327

Figure 7-6   10°K spectral response for samples I-4 and I-1

118

8. COMPARISON OF THE ELECTRICAL PROPERTIES
OF BULK MATERIAL AND DETECTORS

Figure 8-1 compares the conductivity temperature dependence of sample I-1 that was gamma and neutron irradiated with the conductivity of an Arthur D. Little (ADL) and Honeywell Radiation Center (HRC) detector (Ref. 9). Detector conductivity was calculated from resistance versus temperature data of Reference 9. Both detectors were square with an area of 4.5×10^{-5} and 9.2×10^{-5} cm^2 for the ADL and HRC detector respectively. The detector thickness was estimated to be 30 μm. At 300°K, both detectors have a lower conductivity than sample I-1. The lower conductivity at 300°K could result from a lower lattice mobility as the carrier densities should be equal in the intrinsic region providing the x value is the same for the three samples. At low temperature, the conductivity of both detectors is larger than the conductivity of sample I-1. The larger conductivity could result from either a larger carrier density, a larger mobility, or both. The shape of the conductivity curves for the detectors at low temperatures, however, suggests that the larger conductivity results from a larger carrier density for the following reasons.

1.   For larger extrinsic carrier densities, the initial decrease in conductivity, when going from the intrinsic-to-extrinsic region, is smaller as is observed for both detectors when compared with sample I-1.

2.   The decrease in conductivity at low temperature usually results from a decrease in mobility, as the carrier density is constant at these temperatures. Generally, the higher carrier density material exhibits a constant mobility below about 20°K (1000/T=50) while the mobility of lower carrier density material exhibits a decreasing mobility in this temperature range. Based on the above, the estimated carrier densities
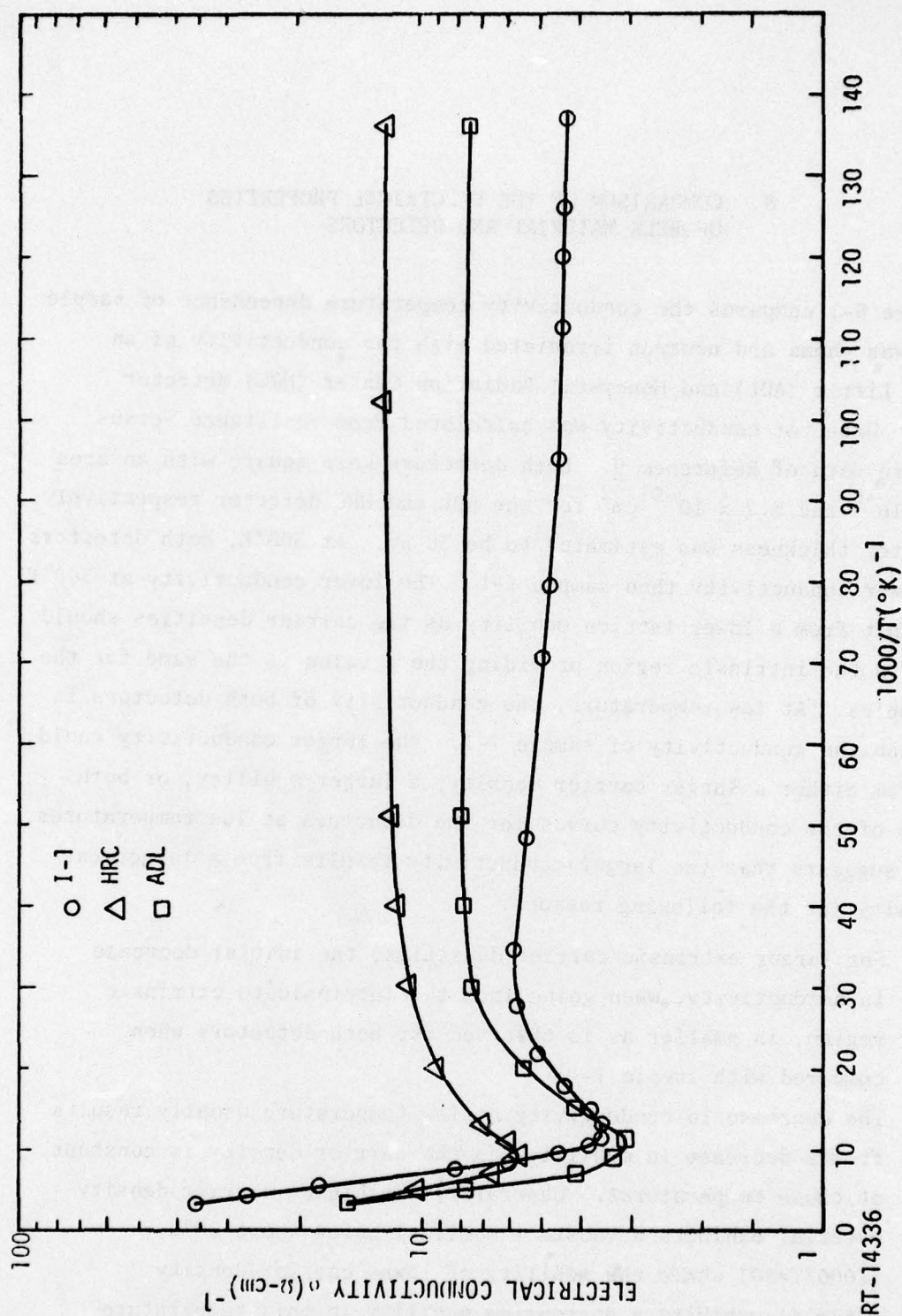
119

Figure 8-1 Comparison of the electrical conductivity temperature dependence of detectors and bulk, Sample I-1

RT-14336

120

are ~1.8 and 3.0 x 10^{14} cm^{-3} for the ADL and HRC detector respectively. The conductivity temperature dependence shows conclusively that both detectors are n-type and probably have carrier densities between 1 and 5 x 10^{14} cm^{-3} and mobilities greater than 1 x 10^5 cm^2/V·sec. From this comparison, it appears that the bulk material studied in this program is representative of material used in detector fabrication, at least in carrier density and mobility.

are -1.6 and 1.6 x 10^14 cm^-3 for the SHM and HG^-18 (?) respectively. The conductivity temperature dependence also demonstrates that both materials are n-type and readily have carrier densities between 1 and 1.6 x 10^14 cm^-3 and mobility...

REFERENCES

1. J. F. Colwell et al., "Study of the Effects of Radiation on the Electrical and Optical Properties of HgCdTe," AFCRL-TR-73-0134, November 1972.

2. J. F. Colwell et al., "Study of the Effects of Radiation on the Electrical and Optical Properties of HgCdTe," AFCRL-TR-73-0761, December 1973.

3. C. E. Mallon et al., "Study of the Effects of Radiation on the Electrical and Optical Properties of HgCdTe," AFCRL-TR-74-0313, June 1974.

4. C. E. Mallon et al., "Study of the Effects of Radiation on the Electrical and Optical Properties of HgCdTe," AFCRL-TR-75-0018, December 1974.

5. R. H. Bube, Photoconductivity of Solids, Wiley & Sons., Inc., New York (1960).

6. J. F. Colwell et al., "Irradiation Effects on PbSnTe," INTEL-RT 8040-001, August 17, 1973, pp. 40-46.

7. M. A. Kinch, M. J. Brau, and A. Simmons, J. Appl. Phys. 44, 1649 (1973).

8. C. E. Mallon et al, "Study of the Effects of Radiation on the Electrical and Optical Properties of HgCdTe," AFCRL-TR-75-0310, 31 May 1975.

9. "R   C/TR-1901   3 June 1976

DISTRIBUTION LIST

Commander in Chief
Continental Air Force Command, JCS
Ent AFB, CO 80912
Attn: DCS/C&E (CESA)

Defense Documentation Center
Cameron Station
Alexandria, VA   22314
Attn: TC (2 copies)

Commander
Defense Electronic Supply Center
1507 Wilmington Pike
Dayton, OH   45401
Attn: ECS

Director Defense Nuclear Agency
Washington, DC   29305
Attn: DDST
      STSI (Archives)
      STTL
      RAEV

Director
Defense Research & Engineering
Washington, DC   20301
Attn: AD/OS

Commander
Field Command
Defense Nuclear Agency
Kirtland AFB, NM   87115
Attn: FCTA-E
      FCSM-A

Interservice Nuclear Weapons School
Kirtland AFB, NM   87115
Attn: Document Control

Director
Joint Strategic Target Planning
   Staff, JCS
Offutt AFB, NE   68113
Attn: JLTW-2

Director
Ballistic Missile Defense Adv.
   Tech. Ctr.
Huntsville Office, P.O. Box 1500
Huntsville, AL   35807
Attn: RDMH-O, F. M. Hoke

Chief of Research & Development
Department of the Army
Washington, DC   20301
Attn: DARD-DDM-N/LTC J. P. Gonce

Commander Frankford Arsenal
Bridge and Tacony Sts.
Philadelphia, PA   19137
Attn: L100, 64-4, G. C. White

Commander
Harry Diamond Laboratories
Washington, DC   20438
Attn: AMXDO-RBF, J. Thompkins
      AMXDO-RB, E. E. Conrad
      AMXDO-NP, Stuart Marcut
      AMXDO-RFB, R. E. McCoskey
               Br-280
      AMXDO-RC, R. Oswald Lab 300
      AMXDO-TI, Technical Library

Commander
Picatinny Arsenal
Attn: SMUPA-QA-N, P. G. Olivieri
      SMUPA-FR-E, L. Avrami
      SMUPA-TS-I-E, A. Grinoch
      SMUPA-ND-N-E

Commander
Redstone Scientific Information Ctr.
U.S. Army Missile Command
Redstone Arsenal, AL   35809
Attn: Chief Documents

Director
U.S. Army Ballistic Res. Laboratories
Aberdeen Proving Ground, MD   21005
Attn: AMXBR-RL, Mr. Harrison

124

AF Weapons Laboratory, AFSC
Kirtland AFB, NM   87117
Attn: SAB
       SUL/Technical Library
       ELP, TREE Section
       SAS
       SAT

AF Avionics Laboratory, AFSC
Wright-Patterson AFB, OH   45433
Attn: AFAL (TEA), H. J. Hennecke

Hq Electronic Systems Division, AFSC
Hanscom AFB, MA   01731
Attn: DCD/SATIN IV
       MCAE, LTC D. Sparks

Commander
Foreign Technology Division, AFSC
Wright-Patterson AFB, OH   45433
Attn: PDTN/Mr. Ballard

Commander
Rome Air Development Center, AFSC
Griffiss AFB, NY   13440
Attn: RCRM, Capt. R. Bellem

Hq Space & Missile Systems Org.
P.O. Box 92960
Worldway Postal Center
Los Angeles, CA   90009
Attn: DYS, Capt. W. Schober
       IND, I. J. Judy
       XRS
       DYS/Maj. Larry A. Darda
       RSSE/LTC Kenneth L. Gilbert

Space & Missile Systesm Organization
Norton AFB, CA   92409
Attn: MNNH/Capt. William M. Carra

Commander in Chief
Strategic Air Command
Offutt AFB, NB   68113
Attn: NRI-STINFO Library

Sandia Laboratories
P.O. Box 5800
Albuquerque, NM   87115
Attn: Org. 2110/J. A. Hood

Central Intelligence Agency
Washington, DC   20505
Attn: RD/SI, Rm. 5G48
       Hq. BLdg./Alice Padgett

Department of Commerce
National Bureau of Standards
Washington, DC   20234
Attn: Applied Rad. Div., Dr. Placious
       Electron Tech. Div., Dr. J.
         C. French

National Aeronautics & Space Admin.

Lewis Research Center
21000 Brookpark Road
Cleveland, OH   44135
Attn: Library

Aerojet Electrosystesm Co.
P.O. Box 296
Azusa, CA   91702
Attn: T. D. Hanscome B170/D6711

Aerospace Corporation
P.O. Box 92957
Los Angeles, CA   90009
Attn: Devl. & Surv. Dir., V. Josephson
       L. W. Aukerman, Bldg. 120
              Rm. 2841
       Library
       D.A. McPherson

AVCO
Government Products Group
201 Lowell St.
Wilmington, MA   01887
Attn: Research Library, A680
       Rm. 2201

Battelle Memorial Institute
505 King Avenue
Columbus, OH   43201
Attn: STOIAC

Bell Aerospace Company
P.O. Box 1
Buffalo, NY   14240
Attn: M. A. Henry, M/S F-11
       C. B. Schoch, M/S I-85

Bendix Corporation
Research Laboratories Division
Bendix Center
Southfield, MI   48075
Attn: D. J. Niehaus, Prog. Devel.

Boeing Company
P.O. Box 3707
Seattle, WA   98124
Attn: A. R. Lowrey, M/S 2R-99
       Aerospace Library
       R. S. Caldwell/2R-00
       D. L. Dye/MS 87-75

Calspan Corporation
P.O. Box 25891
Albuquerque, NM   87125
Attn: R. H. Dickhaut, Bldg. 10,
       Rm. 341

Charles Stark Draper Laboratory, Inc.
68 Albany St.
Cambridge, MA   02139
Attn: Paul Kelly

Cincinnati Electronics Corp.
2630 Glendale-Milford Road
Cincinnati, OH   45241
Attn: C. R. Stump

Collins Radio Company
5225 C Ave, NE
Cedar Rapids, IA   52406
Attn: M. Lahr, Librarian
       Bldg. 106-216
       Ar. R. Langenfeld,
       Bldg. 107-150

E-Systems, Inc.
Greenville Division
P.O. Box 1056
Greenville, TX   75401
Attn: Library 50100

Energy Conversion Devices, Inc.
1675 West Maple Road
Troy, MI   48084
Attn: Lionel Robbins

Fairchild Camera & Instrument Corp.
464 Ellis Street
Mountain View, CA   94040
Attn: Security Dept., 2-233,
       D. K. Myers

Franklin Institute
20th St. and Parkway
Philadelphia, PA   19103
Attn: R. H. Thompson

General Electric Company
Aerospace Electronics Systems
French Road
Utica, NY   13503
Attn: W. J. Patterson, Drop 233

General Electric Company
Space Division
P.O. Box 8555
Philadelphia, PA   19101
Attn: J. L. Andrews, Rad. Eff. Lab.
       J. P. Spratt, Room M 9549

General Research Corporation
P.O. Box 3587
Santa Barbara, CA   93105
Attn: John Ise, Jr.

Grumman Aerospace Corporation
South Oyster Bay Road
Bethpage, nY   11714
Attn: Dept. 533, Pt. 35, J. Rogers

GTE Sylvania, Inc.
189 B St.
Needham Heights, MA   02194
Attn: H&V Group, M. A. Nurefora

GTE Sylvania, Inc.
Electronics Systems Group, Eastern Div.
77 A Street
Needham, MA   02194
Attn: Elec. Sys. Div., L. L. Blaisdell
       S/V Eng. Dept., J. A. Waldron
       Librarian, C. Thronhill

Harris Corp.
P.O. Box 883 Semiconductor Div.
Melbourne, FL   32901
Attn: T. L. Clark, M/S 4040

126

Honeywell, Inc.
Gov. and Aeron. Prod. Div.
1625 Zarthan Ave.
Minneapolis, MN   55416
Attn: R. R. johnson, A1391

Honeywell, Inc.
Radiation Center
2 Forbes Road
Lexington, MA   02173
Attn: Technical Library

Honeywell, Inc.
Aerospace Division
13350 U.S. Highway 19
St. Petersburg, FL   33733
Attn: Stacey H. Graff, M/S 725-J

Hughes Aircraft Company
Centinella Ave. & Teale St.
Culver City, CA   90230
Attn: Dr. Dan Binder, M/S 6-D147

Hughes Aircraft Company
Space Systems Division
P.O. Box 92919
Los Angeles, CA   90009
Attn: E. C. Smith, M/S C624
       W. W. Scott, M/S A1080

ITT Research INstitute
10 West 35th St.
CHicago, IL   60616
Attn: J.E. Bridges
       I. Mindel

Institute for Defense Analyses
400 Army-Navy Drive
Arlington, VA   22202

Intelcom Rad Tech
P.O. Box 81087
San Diego, CA   92123
Attn: R. E. Leadon
       J. A. Naber
       C. E. Mallon

Int. Business Machines Corp.
Route 17C
Owego, NY   13827
Attn: F. C. Tietze, Dept. L99
       Frank Frankovsky

Intl. Telephone & Teleg. Corp.
500 Washington Ave.
Nutley, NJ   07110
Attn: A. Richardson, Avionic Div.

Ion Physics Corp.
South Bedford St.
Burlington, MA   01803
Attn: H. Milde
       R. Evans

Johns Hopkins University
Applied Physics Laboratory
8621 Georgia Ave.
Silver Spring, MD   20910
Attn: P. E. Partridge

Kaman Sciences, Corp.
P.O. Box 7463
Colorado Springs, CO   80933
Attn: W. Ware
       W. F. Rich
       A. P. Bridges

Lockheed Missile & Space Co.
3251 Hanover St.
Palo Alto, CA   94304
Attn: C. F. Kooi, 52-11

Lockheed Missile & Space Co.
P.O. Box 504
Sunnyvale, CA   94088
Attn: B. T. Kimura/Dept. 81-14
       H. Schneemann/Dept. 81-62
       D. M. Tellep/Dept. 81-01
       E. A. Smith/Dept. 85-85
       Dept. 81-23, Bldg. 154, M-365

LTV Aerospace Corp.
Vought Systems Division
P.O. Box 6267
Dallas, TX   75222
Attn: Technical Data Center

MIT Lincoln Laboratory
P.O. Box 73
Lexington, MA   02173
Attn: Leona Loughlin, Librarian

127

Martin-Marietta Aerospace
Orlando Division
P.O. Box 5837
Orlando, FL   32805
Attn: W. W. Mras, MP-413
       M. C. Griffith, MP-30
       J. M. Ashford, MP-537

Maxwell Laboratories, Inc.
9244 Balboa Avenue
San Diego, CA   92123
Attn: V. Fargo

McDonnell Douglas Corp.
5301 Bolsa Ave.
Huntington Beach, CA   92647
Attn: Stanley Schneider

MITRE Corporation
P.O. Box 208
Bedford, MA   01730
Attn: M. E. Fitzgerald

National Academy of Sciences
2101 Constitution Ave., NW
Washington, DC   20418
Attn: Dr. R. S. Shane, National
       Materials Advisory Board

University of New Mexico
Dept. of Campus Security & Police
1821 Roma, NE
Albuquerque, NM   87106
Attn: W. W. Grannemann

Northrop Corporation
Research & Technology Center
3401 West Broadway
Hawthorne, CA   90250
Attn: O. L. Curtis, Jr.
       Library
       D. N. Pocock

Perkin-Elmer Corp.
Main Avenue
Norwalk, CT   06852
Attn: D. P. Mathur

Philco-Ford Corporation
Aerospace & Comm. Operations
Aeronutronic Division
Ford & Jamboree Roads
Newport Beach, CA   92663
Attn: K. C. Attinger
       L. H. Linder

Philco-Ford Corporation
Western Devel. Laboratories Div.
3939 Fabian Way
Palo Alto, CA   94303
Attn: D. R. McMorrow, M/S G-30
       Library

R&D Associates
P.O. Box 3580
Santa Monica, CA   90403
Attn: S. Clay ROgers
       R. A. Poll
       R. R. Schaefer

Rand Corporation
1700 Main St.
Santa Monica, CA   90406
Attn: Cullen Crain

Raytheon Company
528 Boston Post Road
Sudbury, MA 01776
Attn: J. R. Weckback

RCA Corporation
Sarnoff Research Center
P.O. Box 432
Princeton, NJ   08540
Attn: W. J. Dennehy
       K. H. Zaininger

RCA Corporation
Govt. & Comm. Systems
Astro Electronics Div.
P.O. Box 800
Princeton, NJ   08540
Attn: George Brucker

Rensselaer Polytechnic Institute
P.O. Box 965
Troy, NY   12181
Attn: R. Ryan, Electron Accel. Fac.

128

MISSION
of
Rome Air Development Center

RADC plans and conducts research, exploratory and advanced development programs in command, control, and communications (C^3) activities, and in the C^3 areas of information sciences and intelligence. The principal technical mission areas are communications, electromagnetic guidance and control, surveillance of ground and aerospace objects, intelligence data collection and handling, information system technology, ionospheric propagation, solid state sciences, microwave physics and electronic reliability, maintainability and compatibility.